Title
Mechanisms in Notch-mediated Development of Arteriovenous Malformation

Author
Kim, Tyson Nam

Publication Date
2012

Mechanisms in Notch-mediated Development of Arteriovenous Malformation

by

Tyson Nam Kim

DISSERTATION

Submitted in partial satisfaction of the requirements for the degree of

DOCTOR OF PHILOSOPHY

in

Bioengineering

in the

GRADUATE DIVISION

of the

UNIVERSITY OF CALIFORNIA, SAN FRANCISCO

AND

UNIVERSITY OF CALIFORNIA, BERKELEY

[redacted]

DEDICATION

To my parents, Chul and Hyun, and my brother David.

You have shaped me as I am today. This work is for to you.

ACKNOWLEDGEMENTS

This work would not have been possible without the wisdom and guidance of my advisor, **Professor Rong Wang**. It is from her example and direction that I am a biologist. I am privileged to have been a member of her laboratory that delves to the heart of vascular development using the most advanced tools in animal genetics and *in vivo* optical imaging. Rong's enthusiasm in science, collaborative spirit, and dedicated work ethic are truly inspiring. Her scientific passion and support have shaped my aspirations in biomedical research and allowed me to learn the important skills of being an independent researcher. I hope to have picked up a bit of her ability and discipline in leading a research program. The life lessons and skills that she has shared will be invaluable in my future endeavors.

I have been privileged with an excellent and supportive committee. **Professor Chris Schaffer** has shaped me as an optical and biological engineer starting from early college. His tireless patience, instruction, and friendship have played a critical role in my desire to pursue graduate studies. I have benefited immensely from his support and collaboration. He has guided the design and *in vivo* applications of our two-photon microscope for cerebrovascular studies. He has honed my skills as a logical thinker and his commitment

to teaching has helped set my intellectual compass. I have watched and learned by his example. He has my deepest admiration and appreciation. **Professor Dorian Liepmann** is the chair of my committee and has enabled me to pursue my studies in Bioengineering at UCSF/UCB. I have benefited from his career advice, support, and collaboration. His expertise in fluid mechanics and computational analysis has shaped important aspects of my dissertation and training as an engineer. He has instilled in me an appreciation and confidence to follow my intellectual curiosity, even if it should lead to entirely new fields. **Professor Deepak Srivastava** has played a key role in forming my goals as a physician-scientist. He has shown me how a clinician can also be a great scientist and mentor. His advice, support, and insights have helped guide the course of my research. I will undoubtedly benefit from his guidance as I endeavor to make my clinical practice and research enhance each other. I have been honored to have **Professor Song Li** serve on my committee. His prior work, enthusiasm, and advice have helped shape my approach to studying endothelial cell biology, *in vivo*, with an engineering lens. His collaborative spirit is one that I will strive to emulate.

Professor Steven Conolly has been an incredible Bioengineering program advisor, course instructor, collaborator, and friend. His joy in sharing practical wisdom and genuine interest in my well-being have enhanced my years in graduate school. I have benefited from our numerous office hours and open discussions, covering topics ranging from image analysis to life happiness. **Dr. Patrick Goodwill** has been a dear colleague and friend. His intelligence and collaboration have influenced my dissertation work while his advice has helped me navigate the challenges of graduate school. His passion in his research is contagious and has helped me stay interested in work outside of my own. **Professor Kevin Shannon** has been an amazing MSTP director. His advocacy has enhanced my training and his advice has helped me keep perspective on my career path. His dedication to physician-scientist training is an example that I will strive to emulate. **Jana Toutolmin** and **Catherine Norton** have made me feel at home in the MSTP and have helped make my time at UCSF happy and rewarding.

I am indebted to the members of the Wang lab for their company and scientific insight. **Dr. Patrick Murphy** has my deepest respect as a scientist, and my appreciation for teaching me so much during my transition into biological research. He has been highly involved in much of the work throughout this dissertation, and in particular, leading the study on AVM regression. He is one of the most intelligent and diligent individuals that I have known, and I am confident that he will make a fantastic professor one day. I hope to emulate his ability to cultivate a beautiful family while being so dedicated in his research. I thank **Dr. Henrik Lindskog** for his dear friendship, intellectual camaraderie, and for helping me strive for an excellent work-life balance. **Yeni Chen** has been both a terrific mentee and diligent researcher. She is a wonderful human being and has helped me keep life perspective on multiple occasions. **Gloria Lu** has brightened my life with her happy personality and beautiful spirit. I am lucky to have met such an incredible person and I will always be amazed with her appreciation of life. **Dr. Corinne Nielson** has been the ideal colleague with whom to share countless discussions about science, life, and the future. Her support and advice have lifted my spirits. **Dr. Professor Douglas Miniati** has been a fantastic clinical mentor. He is a role model for balancing research, surgery, and a beautiful family life. **Dr. Eric Jelin** showed me how diligence and intelligence could be complemented with a healthy dose of humor. Collaborating with him was very rewarding. I admire **Dr. Henar Cuervo** for her great energy and her refreshing honesty. I appreciate **Dr. Karyn Catalano's** kindred spirit and how she values people in her life. **Dr. Weiya Jiang** has brought me happiness with her gentle, and oddly lovable, approach to everything. I have enjoyed **Dr. Marc Bolliger's** calm personality and humor. **Dr. Christen Munkittrick** has helped me navigate many important hurdles of graduate school. I was inspired to join the lab, in large part, by the work of **Dr. Shant Vartanian** and **Dr. Yuankai Lin**. I enjoyed my collaborations with **Drs. Yupeng Kong, Ruchika Srinivasan, Sara Runge, Tadayoshi Watanabe,** and **Salvador Guevara-Gallardo.** They have helped me appreciate the importance of always learning from others around you. **Morgan Anderson, Claudia Tomas-Miranda, Leslie Neely,** and **Yusef Karaouni** brought joy and fun into the lab for several years.

My time at UCSD has shaped my path in science and life. I greatly appreciate the support of **Professor David Kleinfeld,** in whose lab I first developed my passion in research. **Dr. Philbert Tsai** was a great mentor with the perfect mix of creativity and methodical approach, while also cultivating a beautiful family. **Dr. Nozomi Nishimura** and **Dr. Quoc Nguyen** were always very friendly and supportive, and their work has greatly impacted the research in this dissertation. **Julia Brown's** dedication to education at UCSD enabled me to focus on my academic passions at an early and impressionable time in life. I will always be thankful for her generosity and will endeavor to follow her example.

Lastly, I would like to thank my close family and friends who have been an incredible source of love, support, and encouragement. To my parents, **Chul Kim** and **Hyun Lee**, and my brother **David**: you have formed me in your image and shaped my passions. This work is for you. To **Lorena Haynes** and **Mark Blubaugh**: your love has been a source of my strength and happiness. You have shared your lives with me and many of your joys are now my own. To my aunt and uncle, **Soo-Young Kim** and **James Spindelman**: your love and example have shaped my values in life, brought me happiness, and taught me the importance of contentment. To **Evelyn Wells** and **John Wells**: you have made me part of your incredible family and I will cherish this forever. To my dear friends **Alex Schafgans** and **Anthony Cheung**: you are the peers from whom I draw personal strength and inspiration. Your personalities and approach to life have profoundly shaped who I am. Your companionship has brought me great happiness over the years and I love you as brothers.

To many others who have come and gone from my life: you have left a profound impact. You will be remembered and forever appreciated.

Chapter 3, in full, has been submitted for publication and is entitled "Line-Scanning Particle Image Velocimetry: an Optical Approach for Quantifying a Wide Range of Blood Flow Speeds in Live Animals". Authors include Tyson N. Kim, Patrick W. Goodwill, Yeni Chen, Steven M. Conolly, Chris B. Schaffer, Dorian Liepmann, and

Rong A. Wang. The dissertation author was the primary researcher and author of this work.

Chapter 4, in full, is a reprint of material as it appears in Patrick A. Murphy, Tyson N. Kim, Gloria Lu, Andrew W. Bollen, Chris B. Schaffer, and Rong A. Wang, "*Notch4* Normalization Reduces Blood Vessel Size in Arteriovenous Malformations", Science Translational Medicine 4, 117 (2012). The dissertation writer was a second author with equal contribution to the first in this work.

Chapter 5, in part, is in preparation for submission to be published. The dissertation author is the primary researcher and author of this work. Yeni Chen performed experiments and provided much dedicated work. Chris B. Schaffer and Rong A. Wang directed and supervised the research that comprises this chapter.

ABSTRACT

Mechanisms in Notch-mediated Development of Arteriovenous Malformation

by

Tyson Nam Kim
Doctor of Philosophy in Bioengineering
University of California, San Francisco 2012
University of California, Berkeley 2012
Professor Rong A. Wang, Dissertation Advisor

The vasculature arborizes as an elegant system of branching arteries, veins, and capillaries. For over a century, forces exerted by blood flow have been recognized to determine the arterial and venous (AV) identities of blood vessels. Recent studies have uncovered genes that are uniquely expressed in arteries but not veins, and vice versa. It is thought that these AV markers are expressed prior to circulation and necessary for the morphogenesis of embryonic arteries and veins, suggesting an interplay of biochemical and hemodynamic cues in development and maintenance of the AV network.

The programs regulating the AV network are disrupted in arteriovenous malformation (AVM), a dangerous condition characterized by enlarged, tangled shunts between arteries and veins that bypass capillaries. These high-flow lesions are believed to persist and enlarge under the influence of blood flow, and the abnormal hemodynamic stress exerted on the vasculature can lead to life-threatening ruptures in organs such as brain. To date, the origin of AVMs is poorly understood. These lesions are speculated to persist as congenital abnormalities from embryonic development, or arise *de novo* later in life. We have previously reported a mouse model of AVMs, wherein endothelial expression of constitutively active Notch4, a potent regulator of arterial identity, caused high-flow shunts to directly join arteries and veins. We hypothesized that reprogramming of the endothelium caused postnatal AVMs through the enlargement of pre-existing capillaries.

We constructed a two-photon laser scanning microscope for *in vivo* observation of vascular development over time. We developed a method to quantify blood velocities in high-flow AVMs, enabling correlation of hemodynamics and formation of these lesions. Utilizing these tools, we discovered that brain AVMs developed from the established AV network by the enlargement of pre-existing microvessels. Additionally, we found that normalization of Notch signaling in our mouse model resulted in the regression of AVMs to capillary-like vessels. Taken together, these results suggest that AVM may arise from capillaries, and importantly, may be a reversible process. This work presents tools that will be highly useful in the study of developmental vascular biology, and sheds light on the pathogenesis of arteriovenous malformations in general.

TABLE OF CONTENTS

LIST OF FIGURES

INTRODUCTION

The vertebrate vasculature forms an extensive and efficient network of blood vessels that allows transport of nutrients, gases, hormones, and circulating cells between tissues and organs of the body. In early vascular development, **endothelial cells** (ECs) assemble and remodel into the first blood vessels through the processes of vasculogenesis and angiogenesis[1,2]. Upon maturation, the vasculature becomes arborized as an elegant hierarchical system of arteries, capillaries, and veins. In the seventeenth century, William Harvey established the functional definition of arteries and veins as vessels that carry blood from and back to the heart, respectively[3]. Hemodynamic forces have been recognized to play a role in shaping blood vessels and were once thought to be the primary determinants of **arteriovenous** (AV) identity[4-7]. Surgical manipulation of blood flow can cause abnormalities in heart and vessel development[8,9] and primary defects in heart contractility have detrimental effects on vessel and cardiac remodeling[10-12]. More recently, biochemical programs have been identified that are involved in specifying arteries and veins prior to circulation[13] raising important questions on the interplay of genetic and hemodynamic cues in development of the AV hierarchy. In a seminal study, Wang *et al.* described the expression pattern of ephrin-B2, a member of a family of membrane-bound ligands, in arterial but not venous endothelial cells of mouse embryo. *EphB4*, a gene encoding the putative receptor for ephrin-B2, was expressed at much higher levels in the veins than the arteries[13,14]. Subsequently, artery- and vein-associated genes have been identified in vertebrate animals and humans[15-17]. Extensive *in vitro* work has been conducted to directly test the role of AV markers on vascular development.

However, the vascular hierarchy cannot be recapitulated *in vitro* or removed from the body without loss of function and has been challenging to study.

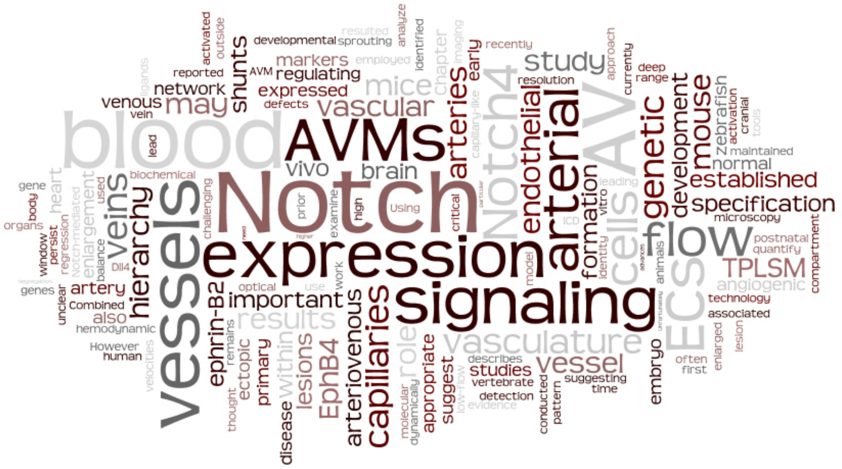

Figure 1.1: Graphical representation of the text in Chapter 1. The relative size of the word correlates with the frequency at which it appears in the chapter.

The relationship between blood flow, AV specification, and vessel hierarchy will be better understood by investigating vascular diseases such as **arteriovenous malformation** (AVM), a dangerous condition characterized by enlarged, tangled shunts that bypass normal capillary beds. These high-flow lesions are believed to persist and enlarge under the influence of blood flow[18,19], and abnormal hemodynamic stress exerted on the vasculature can lead to life-threatening ruptures in organs such as brain[18,19]. Treatments for these fragile lesions include surgical resection, radiological ablation, and endovascular embolization - interventions that can be associated with significant risk in themselves[20]. Unfortunately, the etiology of AVMs remains unclear and has hindered design of molecular therapies for the disease. Observations in human skin AVMs suggest that these defects are initiated by the enlargement of post-capillary venules and grow over time[21]. In contrast, brain AVMs are often discovered in younger people and have morphologic similarities to early vasculature, leading to the hypothesis that these lesions persist as congenital abnormalities[22,23]. Recently, we have reported that expression of **activated Notch4** (Notch4*) in endothelial cells results in AVMs in young and adult mice[24,25]. Additionally, we and others have linked increased Notch signaling in ECs with human brain AVMs[26,27], suggesting an important role for this signaling pathway in the pathogenesis of the disease. The ability to dynamically study the formation and possible regression of AVMs through a Notch-mediated mechanism would shed light on this enigmatic disease and be a powerful tool in understanding how the AV network is established and maintained.

Notch signaling is an exquisitely sensitive regulator of lineage decisions in many aspects of embryonic development[28,29] and is a critical mediator in the arterial specification of endothelial cells. In brief, Notch receptors are a class of transmembrane proteins that are activated through direct cell-cell contact by ligands on adjacent cells, resulting in sequential cleavage events that release the Notch **intracellular domain** (ICD)[30]. The ICD translocates to the nucleus where it must associate with the DNA-binding protein, RBP-J, to elicit transcription of target genes. In mice, Notch1 and Notch4 are expressed in arterial ECs[31,32]. Embryos that lack Notch activity expressed venous marker EphB4 ectopically in the aorta[33,34]. Mutants lacking the Notch ligand Dll4 had decreased expression of arterial markers ephrin-B2, connexin40, and neuropilin-1, while exhibiting ectopic expression of EphB4 in arteries[30,35]. Consistent with these findings, we found that expression of **activated-Notch4** (Notch4*) in ECs resulted in upregulation of ephrin-B2 and concomitant reduction of EphB4 in veins[25,36].

Notch's role in regulating markers of AV identity in ECs is compelling evidence for the physical segregation of arteries and veins. In embryo, the first artery and vein develop in close proximity to each other from what was once thought to be a homogenous population of angioblasts in the lateral plate mesoderm. In zebrafish, the Notch downstream gene gridlock (homologue of Hey2 in mammals) labels arterial precursors and is also necessary for formation of the dorsal aorta[37]. Additional studies have implicated Notch signaling in the sorting of endothelial cells between the early artery and vein in zebrafish and mouse embryo[38,39]. Interestingly, Notch has recently been established in regulating angiogenic sprouting. Several studies have provided different lines of evidence that Notch-Dll4 signaling at the angiogenic front suppresses tip cell formation and inhibits sprouting angiogenesis[40-44]. Combined with the highly mosaic pattern of Dll4 expression and Notch activation in the retina[42-44], these results suggest that the activation of Notch signaling imparts a quiescent, non-sprouting phenotype on some ECs that may help to maintain the integrity of angiogenic blood vessels**.** However, these studies were conducted in specialized model systems such as developing mouse retina or intersgmental vessels in the zebrafish embryo, where it was simpler to examine the extension of non-lumanized ECs into avascular regions. It currently remains unclear how perfused capillaries are maintained within the established AV network. Using our Notch-mediated mouse model of AVMs, we investigated how the appropriate balance of Notch signaling in vessels is not only important for AV identity, but also for regulating the critical interface between arteries and veins through small, low-flow capillaries.

Figure 1.2: Graphical representation of the text in Chapter 2. The relative size of the word correlates with the frequency at which it appears in the chapter.

Recent advances in technology have enabled *in vivo* observation of blood flow and vessel morphology over time with microscopic resolution. Combined with advanced genetic tools, we may now investigate the role of hemodynamics and molecular specification on AV hierarchy with incredible scrutiny. **Chapter two** of this dissertation describes the combination of optical and genetic tools as an approach to study vascular development in the living mouse. In particular, we use **two-photon fluorescence laser-scanning microscopy** (TPLSM) to image fluorescently labeled vessels and structure deep within mice over multiple time-points. We describe how this technology may be used to quantify blood flow in individual microvessels when employed with the appropriate algorithms. We also demonstrate several genetic approaches that enable detection and alteration of the biochemical composition of cells within vessels, which may be dynamically studied over time with *in vivo* imaging.

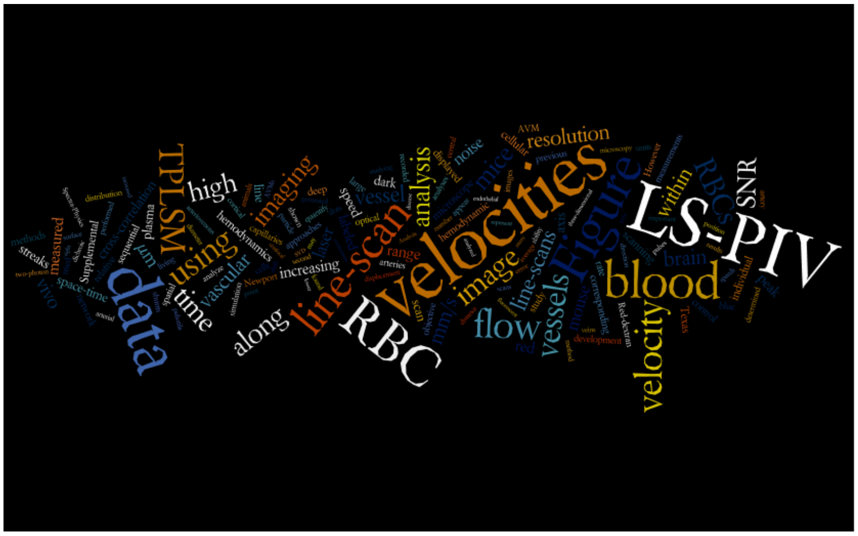

Figure 1.3: Graphical representation of the text in Chapter 3. The relative size of the word correlates with the frequency at which it appears in the chapter.

Quantifying blood flow with optical resolution in intact animals is technically challenging. Traditional single-photon microscopes have difficulty imaging into thick specimens. Alternatively, confocal microscopy and TPLSM can be used to quantify blood flow hundreds of micrometers deep, but have traditionally been limited to the lower range of velocities present in mice. **Chapter three** describes an analytical approach that, when employed with well-established TPLSM protocols[45], can analyze a wider range of blood velocities. This work was motivated by our need to analyze the high flow speeds harbored by large arteriovenous malformations.

Figure 1.4 Graphical representation of the text in Chapter 4. The relative size of the word correlates with the frequency at which it appears in the chapter.

We previously reported that expression of Notch4* in endothelium of neonatal mice results in brain arteriovenous malformation[25]. **Chapter four** investigates the regression of these high flow lesions. We use *in vivo* TPLSM through a cranial window and observe that repression of Notch4* resulted in conversion of large-caliber AV shunts into capillary-like vessels. These structural changes are associated with recovery of tissue hypoxia, restoration of EphB4 expression in venous ECs and a normalization of blood flow. Importantly, our study suggests that AVMs may be treated therapeutically by targeting the causal genetic lesion.

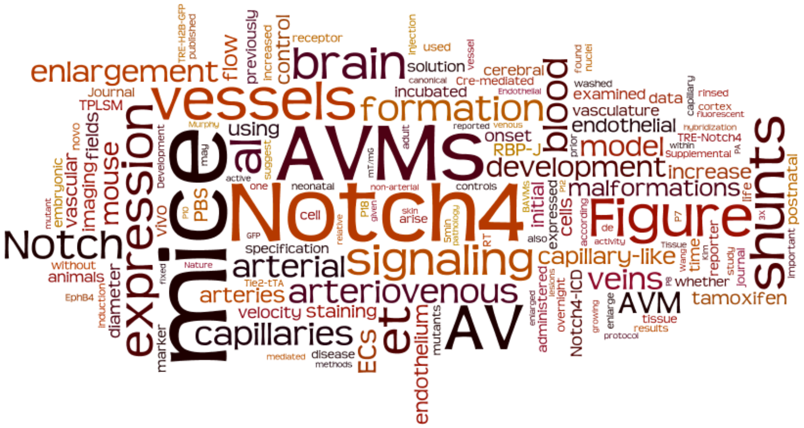

Figure 1.5 Graphical representation of the text in Chapter 5. The relative size of the word correlates with the frequency at which it appears in the chapter.

The developmental origin of AVMs is currently unknown. In **chapter five**, we examine how brain AVMs arise from the cerebral vasculature upon postnatal expression of Notch4*. Using *in vivo* TPLSM through a cranial window, we observed that AV shunts enlarged from capillary-like vessels. The initial enlargement of these low-flow vessels often preceded their increase in blood velocity, indicating that expansion of the vessel lumen was the primary developmental defect. AV specification of the vasculature in mutant mice appeared normal at P10 prior to detection of Notch4* expression, suggesting that AV shunts arose from normal capillaries within the AV hierarchy. Next, we examined whether the ectopic Notch signaling outside the arterial compartment was responsible for AVMs. Conditional expression of Notch4* in arterial ECs did not lead to AVM formation. Similarly, blocking canonical Notch signaling in all ECs, but not arterial ECs, prevented the AVMs. Taken together, these results indicate that ectopic Notch signaling outside of the arterial compartment was the specific genetic lesion leading to the enlargement of capillaries. These results compellingly suggest that the appropriate balance of Notch signaling is important for the maintenance of capillaries in postnatal life.

REFERENCES

1 Pardanaud, L., Yassine, F. & Dieterlen-Lievre, F. Relationship between vasculogenesis, angiogenesis and haemopoiesis during avian ontogeny. *Development* **105**, 473-485 (1989).

2 Poole, T. J. & Coffin, J. D. Vasculogenesis and angiogenesis: two distinct morphogenetic mechanisms establish embryonic vascular pattern. *J Exp Zool* **251**, 224-231, doi:10.1002/jez.1402510210 (1989).

3 Auffray, C. & Noble, D. Origins of systems biology in William Harvey's masterpiece on the movement of the heart and the blood in animals. *Int J Mol Sci* **10**, 1658-1669, doi:10.3390/ijms10041658 (2009).

4 Murray, C. D. The Physiological Principle of Minimum Work Applied to the Angle of Branching of Arteries. *J Gen Physiol* **9**, 835-841 (1926).

5 Murray, C. D. The Physiological Principle of Minimum Work: I. The Vascular System and the Cost of Blood Volume. *Proceedings of the National Academy of Sciences of the United States of America* **12**, 207-214 (1926).

6 Girard, H. Arterial pressure in the chick embryo. *Am J Physiol* **224**, 454-460 (1973).

7 Gonzalez-Crussi, F. Vasculogenesis in the chick embryo. An ultrastructural study. *Am J Anat* **130**, 441-460, doi:10.1002/aja.1001300406 (1971).

8 Kurz, H. Physiology of angiogenesis. *J Neurooncol* **50**, 17-35 (2000).

9 le Noble, F. *et al.* Flow regulates arterial-venous differentiation in the chick embryo yolk sac. *Development* **131**, 361-375, doi:10.1242/dev.00929 (2004).

10 Conway, S. J., Kruzynska-Frejtag, A., Kneer, P. L., Machnicki, M. & Koushik, S. V. What cardiovascular defect does my prenatal mouse mutant have, and why? *Genesis* **35**, 1-21, doi:10.1002/gene.10152 (2003).

11 Huang, C. *et al.* Embryonic atrial function is essential for mouse embryogenesis, cardiac morphogenesis and angiogenesis. *Development* **130**, 6111-6119, doi:10.1242/dev.00831 (2003).

12 Lucitti, J. L. *et al.* Vascular remodeling of the mouse yolk sac requires hemodynamic force. *Development* **134**, 3317-3326, doi:10.1242/dev.02883 (2007).

13 Wang, H. U., Chen, Z. F. & Anderson, D. J. Molecular distinction and angiogenic interaction between embryonic arteries and veins revealed by ephrin-B2 and its receptor Eph-B4. *Cell* **93**, 741-753 (1998).

14 Gerety, S. S., Wang, H. U., Chen, Z. F. & Anderson, D. J. Symmetrical mutant phenotypes of the receptor EphB4 and its specific transmembrane ligand ephrin-B2 in cardiovascular development. *Mol Cell* **4**, 403-414 (1999).

15 Gale, N. W. *et al.* Ephrin-B2 selectively marks arterial vessels and neovascularization sites in the adult, with expression in both endothelial and smooth-muscle cells. *Dev Biol* **230**, 151-160, doi:10.1006/dbio.2000.0112 (2001).

16 Shin, D. *et al.* Expression of ephrinB2 identifies a stable genetic difference between arterial and venous vascular smooth muscle as well as endothelial cells, and marks subsets of microvessels at sites of adult neovascularization. *Dev Biol* **230**, 139-150, doi:10.1006/dbio.2000.9957 (2001).

17 Ekman, N. *et al.* Bmx tyrosine kinase is specifically expressed in the endocardium and the endothelium of large arteries. *Circulation* **96**, 1729-1732 (1997).

18 Morgan, M. & Winder, M. Haemodynamics of arteriovenous malformations of the brain and consequences of resection: a review. *J Clin Neurosci* **8**, 216-224, doi:10.1054/jocn.2000.0795 (2001).

19 Corti, P. *et al.* Interaction between alk1 and blood flow in the development of arteriovenous malformations. *Development* **138**, 1573-1582, doi:10.1242/dev.060467 (2011).

20 Stapf, C., Mohr, J. P., Choi, J. H., Hartmann, A. & Mast, H. Invasive treatment of unruptured brain arteriovenous malformations is experimental therapy. *Curr Opin Neurol* **19**, 63-68 (2006).

21 Braverman, I. M., Keh, A. & Jacobson, B. S. Ultrastructure and three-dimensional organization of the telangiectases of hereditary hemorrhagic telangiectasia. *J Invest Dermatol* **95**, 422-427 (1990).

22 Friedlander, R. M. Clinical practice. Arteriovenous malformations of the brain. *N Engl J Med* **356**, 2704-2712, doi:10.1056/NEJMcp067192 (2007).

23 Mullan, S., Mojtahedi, S., Johnson, D. L. & Macdonald, R. L. Embryological basis of some aspects of cerebral vascular fistulas and malformations. *J Neurosurg* **85**, 1-8, doi:10.3171/jns.1996.85.1.0001 (1996).

24 Carlson, T. R. *et al.* Endothelial expression of constitutively active Notch4 elicits reversible arteriovenous malformations in adult mice. *Proc Natl Acad Sci U S A* **102**, 9884-9889 (2005).

25 Murphy, P. A. *et al.* Endothelial Notch4 signaling induces hallmarks of brain arteriovenous malformations in mice. *Proceedings of the National Academy of Sciences of the United States of America* **105**, 10901-10906, doi:10.1073/pnas.0802743105 (2008).

26 ZhuGe, Q. *et al.* Notch-1 signalling is activated in brain arteriovenous malformations in humans. *Brain* **132**, 3231-3241, doi:10.1093/brain/awp246 (2009).

27 Murphy, P. A., Lu, G., Shiah, S., Bollen, A. W. & Wang, R. A. Endothelial Notch signaling is upregulated in human brain arteriovenous malformations and a mouse model of the disease. *Lab Invest* **89**, 971-982, doi:10.1038/labinvest.2009.62 (2009).

28 Nichols, S. A., Dirks, W., Pearse, J. S. & King, N. Early evolution of animal cell signaling and adhesion genes. *Proceedings of the National Academy of Sciences of the United States of America* **103**, 12451-12456, doi:10.1073/pnas.0604065103 (2006).

29 King, N. *et al.* The genome of the choanoflagellate Monosiga brevicollis and the origin of metazoans. *Nature* **451**, 783-788, doi:10.1038/nature06617 (2008).

30 Lai, E. C. Notch signaling: control of cell communication and cell fate. *Development* **131**, 965-973, doi:10.1242/dev.01074 (2004).

31 Del Amo, F. F. *et al.* Expression pattern of Motch, a mouse homolog of Drosophila Notch, suggests an important role in early postimplantation mouse development. *Development* **115**, 737-744 (1992).

32 Uyttendaele, H. *et al.* Notch4/int-3, a mammary proto-oncogene, is an endothelial cell-specific mammalian Notch gene. *Development* **122**, 2251-2259 (1996).

33 Lawson, N. D. *et al.* Notch signaling is required for arterial-venous differentiation during embryonic vascular development. *Development* **128**, 3675-3683 (2001).

34 Krebs, L. T. *et al.* Haploinsufficient lethality and formation of arteriovenous malformations in Notch pathway mutants. *Genes & development* **18**, 2469-2473, doi:10.1101/gad.1239204 (2004).

35 Villa, N. *et al.* Vascular expression of Notch pathway receptors and ligands is restricted to arterial vessels. *Mech Dev* **108**, 161-164 (2001).

36 Murphy, P. A. *et al.* Notch4 normalization reduces blood vessel size in arteriovenous malformations. *Sci Transl Med* **4**, 117ra118, doi:10.1126/scitranslmed.3002670 (2012).

37 Lawson, N. D. & Weinstein, B. M. Arteries and veins: making a difference with zebrafish. *Nature reviews. Genetics* **3**, 674-682, doi:10.1038/nrg888 (2002).

38 Herbert, S. P. *et al.* Arterial-venous segregation by selective cell sprouting: an alternative mode of blood vessel formation. *Science* **326**, 294-298, doi:10.1126/science.1178577 (2009).

39 Kim, Y. H. *et al.* Artery and vein size is balanced by Notch and ephrin B2/EphB4 during angiogenesis. *Development* **135**, 3755-3764, doi:10.1242/dev.022475 (2008).

40 Lobov, I. B. *et al.* Delta-like ligand 4 (Dll4) is induced by VEGF as a negative regulator of angiogenic sprouting. *Proceedings of the National Academy of Sciences of the United States of America* **104**, 3219-3224, doi:10.1073/pnas.0611206104 (2007).

41 Suchting, S. *et al.* The Notch ligand Delta-like 4 negatively regulates endothelial tip cell formation and vessel branching. *Proceedings of the National Academy of Sciences of the United States of America* **104**, 3225-3230, doi:10.1073/pnas.0611177104 (2007).

42 Claxton, S. & Fruttiger, M. Periodic Delta-like 4 expression in developing retinal arteries. *Gene Expr Patterns* **5**, 123-127, doi:10.1016/j.modgep.2004.05.004 (2004).

43 Hellstrom, M. *et al.* Dll4 signalling through Notch1 regulates formation of tip cells during angiogenesis. *Nature* **445**, 776-780, doi:10.1038/nature05571 (2007).

44 Hofmann, J. J. & Luisa Iruela-Arispe, M. Notch expression patterns in the retina: An eye on receptor-ligand distribution during angiogenesis. *Gene Expr Patterns* **7**, 461-470, doi:10.1016/j.modgep.2006.11.002 (2007).

45 Shih, A. Y. *et al.* Two-photon microscopy as a tool to study blood flow and neurovascular coupling in the rodent brain. *J Cereb Blood Flow Metab*, doi:10.1038/jcbfm.2011.196 (2012).

II

Optical tools for *in vivo* imaging of vascular development and blood flow

Optical approaches are well suited for the detailed study of biology. In particular, fluorescence microscopy is a powerful technique that allows for high-resolution imaging of structures that can be selectively labeled. Signal is generated from these structures using an external source of excitation light that is focused onto the sample. With conventional fluorescence microscopy, signal is produced throughout the path of excitation light. It becomes impossible to distinguish in- or out-of-focus fluorescence once it has reached the detector, thus fluorescence generated outside the focal plane can contribute to severe reduction in image quality. Histology addresses this problem by cutting the sample into thin slices, thereby eliminating 'out-of-focus' material. However, this approach is highly invasive in living specimens. Alternatively, confocal and multiphoton microscopy are powerful tools for imaging in thick specimens by recording fluorescent signal originating from a known focal point in three-dimensional space. Both methods focus excitation light into the specimen and generate fluorescent signal by scanning the focal point throughout a volume. The fluorescence at this point is recorded and extrapolated into a three-dimensional map of fluorescence intensity[1,2].

Confocal microscopy utilizes linear excitation of fluorescence. The signal that is produced above and below the focal point is removed by re-imaging the collected light onto a mask (pinhole). The photons generated at the focal point pass through the mask while photons generated elsewhere are blocked. Thus, confocal microscopy is able to selectively distinguish fluorescence from one position using sophisticated filtering techniques. Alternatively, multiphoton microscopy generates fluorescence only at one focal spot in three-dimensional space. There is no ‘out-of-focus’ fluorescence that needs to be filtered and all collected signal can contribute to image reconstruction. The ability to generate fluorescence in one spot, deep within a specimen, is made possible by harnessing nonlinear optical effects that occur with extremely high intensities of light (generally on the order of 10^{10} W/cm^2 and above). In the lab, these high intensities can be achieved momentarily during **femtosecond** (fs) pulses from an ultrafast laser. Light exhibits very different properties in this intensity regime. One particularly useful property for biological study has been two-photon absorption for fluorescence generation. In two-photon excited fluorescence, the energy of a single photon of laser light is insufficient to energize a fluorescent molecule into a fluorescent state. However, the energy of two photons may be absorbed simultaneously if the intensity of light (density of photons) is sufficiently high. The probability of this event depends on the intensity of light squared. Therefore, with tight focusing and controlled laser intensity, two-photon absorption can be induced in only a small focal volume within three-dimensional space.

TPLSM has two major advantages over confocal microscopy for *in vivo* imaging. **First**, TPLSM induces less phototoxicity in the specimen. As with fluorescence, phototoxicity occurs only at the focal point because the laser intensity elsewhere is insufficient to excite molecules that would convert to harmful reactive species. The average power and energy deposition into the tissue remains low despite the high intensities achieved with ultrafast lasers. For example, our laser (MaiTai HP; SpectraPhysics) will generate 100 fs laser pulses at approximately 60 MHz. Cumulatively, these brief laser pulses are proportional in time to about half a second of light distributed across a full day. Although multiphoton-mediated effects can potentially harm tissue, empirical studies demonstrate that cells in culture survive better with TPLSM than with confocal microscopy. **Second**, TPLSM can image significantly deeper into specimens due to its relative insensitivity to scattering. In confocal microscopy, any fluorescence photons that are scattered by tissue can deviate from their ballistic path to the detector. These photons will miss the pinhole and result in a loss of useful signal. Conversely, fluorescence that is scattered in TPLSM can still contribute to the image because the origin of the signal is already known and no mask is required. In combination, these attributes have made TPLSM a robust tool for *in vivo* imaging deep within living specimens.

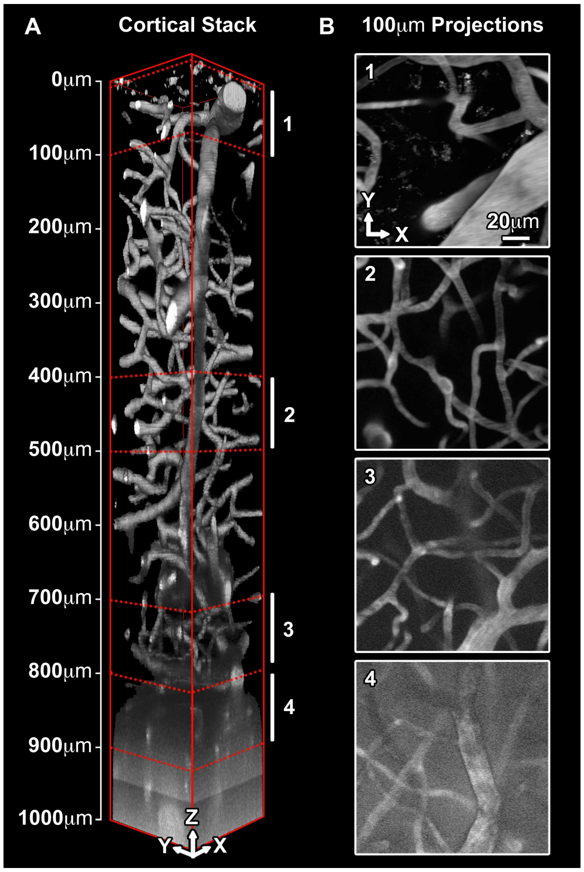

Figure 2.1: Deep cortical imaging with *in vivo* TPLSM. A, Three-dimensional rendering of cortical vessels imaged with TPLSM demonstrating depth-dependent decrease in signal-to-noise ratio. The blood plasma was labeled with Texas Red-dextran and a 1000 mm stack was acquired with images at 1 mm spacing along the z-axis starting from the brain surface. **B,** 100 mm-thick projections of regions 1-4 in panel (A).

In vivo imaging of blood vessels with arteriovenous specificity

Advancements in genetic technologies allow for selective fluorescent labeling of normal or biochemically altered tissues, enabling incredible scrutiny of *in vivo* biology when combined with TPLSM. Importantly, this blend of genetics and optics is unbound from static, post-mortem analysis and allows for detailed study of dynamic processes over time. The experimental possibilities are vast. This section describes several applications that can useful in the study of vascular biology.

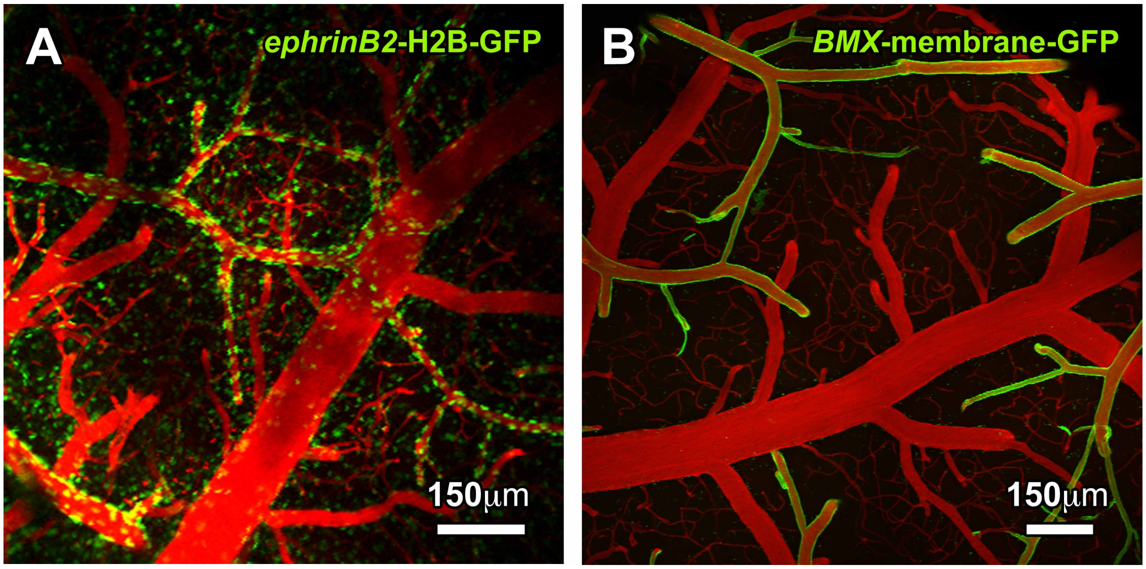

Figure 2.2: *In vivo* imaging of blood vessels with arterial specification. A, TPLSM projection of cortical vasculature in *ephrin-B2*$^{+/H2B\text{-}eGFP}$ mouse with the blood plasma labeled by intravenous injection of Texas Red-dextran. *Ephrin-B2*$^{+/H2B\text{-}eGFP}$ mice express nuclear GFP in arterial endothelial cells, which allows these vessels to be distinguished with cellular resolution. **B,** TPLSM projection of cortical vasculature in *BMX-CreER; mT/mG* mouse where the plasma is labeled by intravenous injection of TexasRed-dextran. Mice were administered Tamoxifen at P1 and P2 to induce Cre-mediated recombination under regulation of the BMX promoter, resulting in irreversible GFP expression in arterial ECs from early post-natal life. Importantly, these cells remain GFP+ despite any subsequent changes in their arteriovenous specification.

Ephrin-B2$^{+/H2B\text{-}eGFP}$ mice express histone-associated GFP under control of the endogenous *ephrin-B2* promoter[3], allowing visualization of arterial endothelium with cellular resolution. *In vivo* TPLSM may be employed to track these cells over time or to examine the acquisition of arterial specification under genetic or hemodynamic perturbations. The *BMX-CreERT*$_2$ mice were kindly provided by the Ralph Adams lab and may be treated with tamoxifen to induce Cre-mediated recombination in arterial endothelium. These arterial ECs can be fluorescently tagged when crossed with the *mT/mG* reporter line[4], where expression of membrane-targeted tdTomato (*mT*) irreversibly converts to membrane-targeted eGFP (*mG*) in the presence of Cre-recombinase. The expression of GFP distinctly resolves the arteriole-capillary boundary and is carried throughout the life and progeny of converted cells. The position of this boundary or mixing of cells between the arteriole and capillary vessels can be examined using the relative contrast between GFP positive and negative cells.

Genetic approaches for studying vascular development with *in vivo* imaging

We utilize three general approaches to induce or remove gene expression with tissue and temporal control. **First**, we employ the well-validated tetracycline regulatory system[5], where the unusually specific transcriptional response to tetracycline in a bacterium was cloned to regulate transgene expression in the presence or absence of the drug. The *Tie2-tTA* construct generated in our lab[6,7] allows expression of the tetracycline transactivator in endothelium under control of the *Tie2* promoter. Combined with a *TRE-transgene* (where *TRE* designates tetracycline response element), the *Tie2-tTA/TRE-transgene* construct allows expression of that transgene with high specificity in ECs. Expression is suppressed when the animals are fed tetracycline or doxycycline. Importantly, use of this system enables both perturbation and re-normalization of key signaling pathways, such as those involved in specification of arteries and veins (further described in Chapters 4 and 5).

Second, the Cre/loxP system relies on the bacteriophage P1 Cre-recombinase that recognizes loxP sites (locus of recombination) and removes the intervening DNA sequence, thereby generating a nonfunctional allele[5,8,9]. Temporal control can be added with tamoxifen-inducible versions of Cre (CreERT), which are fusion proteins consisting of mutated ligand-binding domains of the estrogen receptor and Cre-recombinase[8,9]. Administration of tamoxifen activates the Cre fusion protein and enables recombination to be timed with a particular process of interest, thereby circumventing other developmental abnormalities or embryonic lethality. Additionally, the recombination of DNA is permanently accomplished in somatic cells and their entire progeny, allowing for lineage tracing of these cells and their expansion. Robust endothelial-specific expression patterns of Cre have been achieved[10,11]. We temporally regulate expression of Cre-recombinase in endothelium using *Cdh5-CreERT*$_2$[12] or in arterial endothelium using *BMX-CreERT2* mice, both kindly provided by the Ralph Adams lab. Importantly, these regulatable Cre mice may be used to disrupt endogenous gene function or activate other genetic constructs in endothelium. For example, the loxP-flanked STOP sequence can be excised to allow expression of GFP in *mT/mG* mice [4] or the tetracycline transactivator in fs-tTA mice[13].

Third, the ability to study behavior and expansion of discrete endothelial cells within the vasculature is a powerful approach in understanding *in vivo* vascular biology at the cellular level. This is made possible by administering *Cdh5-CreERT*$_2$[12] mice with a sufficiently low dose of tamoxifen to allow Cre-mediated recombination in only a few endothelial cells per image field. Combined with the above-mentioned Cre-responsive constructs, these discrete cells may be programmed for gene deletion, activation, and/or GFP expression in an effectively normal animal. We examine these cells over time with TPLSM to better understand their function and maintenance within the artery and vein systems.

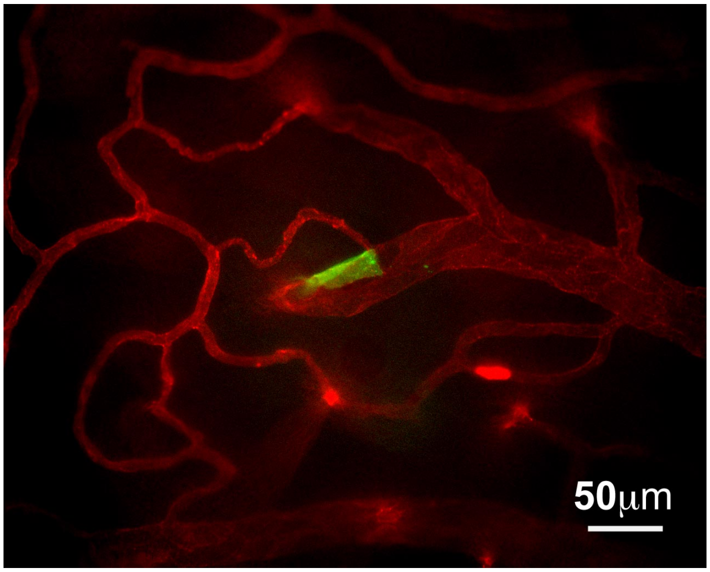

Figure 2.3: Labeling and study of discrete EC behavior in mouse brain. Imaging of cortical vasculature of *Cdh5-CreERT*$_2$*;mT/mG* mouse perfused with Cy5-conjugated Lycopersicon esculentum lectin. The animal was administered low-dose Tamoxifen at P1 to induce Cre-mediated recombination in a few discrete endothelial cells, resulting in their expression of GFP from early post-natal life. Importantly, these cells continue to express GFP+ and their migration and proliferation can be tracked over time by *in vivo* TPLSM.

Optical approaches for quantifying blood flow

Video-rate microscopy has been widely used for studying flow within microfluidic devices by imaging moving particles[14,15] and employing computational approaches to quantify their displacement between serial images. In particular, digital particle image velocimetry (DPIV) is a robust method for calculating velocities from these data. Traditionally, DPIV utilizes fast Fourier transforms to determine the cross-correlation of two serial images of a flow field. The location of the cross-correlation peak represents the most probable particle displacement within a sub-region. The velocity at that location is determined from dividing by the time interval between exposures. DPIV has many desirable features including high resolution and the ability to quantify complex flow fields. However, it has had minimal application *in vivo* because of difficulty in acquiring data with sufficient spatiotemporal resolution deep in tissues with traditional microscopy. Nevertheless, cross-correlation based approaches hold great promise for analyzing blood flow when employed with advanced imaging techniques. One example will be discussed further in Chapter 3.

Several optical approaches have been used to quantify blood flow in living animals. **First**, laser Doppler flowmetry (LDF) utilizes a single wavelength of laser light to illuminate moving RBCs. The wavelength of light is broadened slightly after scattering from these cells, and the degree of broadening is a measure of their speed. While easy to use, LDF has course spatial resolution due to the large scattering properties of most tissues. It is best applied for comparative study of blood perfusion in a delocalized area. **Second,** speckle imaging is a method that quantifies blood speed utilizing the interference of coherent light as photons scatter off tissue and interfere with each other from nearby points[16]. Scattering of the laser light on the specimen results in a 'speckled' appearance as photons constructively or destructively interfere. The blood flow can be quantified by measuring the change in contrast of the speckles as RBCs move through the vessel. Lateral resolution of speckle imaging is about one scattering length (~200 mm), and though an improvement upon LDF, also has difficulty distinguishing sub-surface blood flow. **Third,** Doppler optical coherence tomography (DOCT)[17] can quantify blood flow along the axial path of light in well-defined microscopic volumes by measuring the Doppler shift of light scattered off moving RBCs. Though a powerful approach for measuring flow in an unbiased fashion, DOCT is currently applicable to speeds under 10 mm/s and in larger vessels rather than capillaries[18]. Additional methods are required to analyze a wider range of RBC velocity with microscopic resolution deep within living specimens.

Fourth, TPLSM and confocal line-scan geometries have been used to track red blood cell (RBC) motion in a vessel-specific[19-23] or multi-vessel[24] fashion. Line-scanning can acquire substantially more frames per second than two-dimensional imaging and, when oriented along the length of a vessel, can resolve RBC motion over relatively large distances. Typically, sequential scans are visualized as a space-time image with distance on the abscissa and time advancing downward on the ordinate. The blood plasma is loaded with fluorescent dye, allowing individual RBCs to appear as dark spots. These dark spots produce streaks in the space-time data if there is sufficient overlap of the same RBCs between scans, where the slope of each streak is inversely proportional to the cell's speed. Previous methods have quantified blood velocities from this data using Singular Value Decomposition (SVD) or Radon transform-based algorithms to determine the angle of the streaks[19,21].

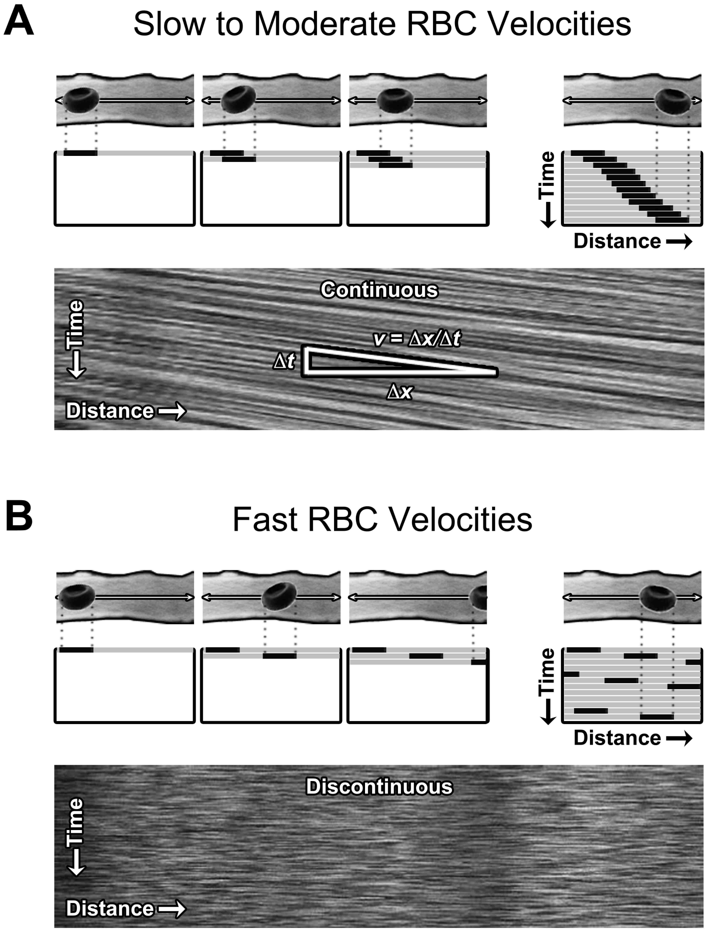

Figure 2.4: Loss of RBC continuity in space-time data when high velocities are measured with line-scans. A, *Top,* schematic of line-scan data of slow to moderate RBC velocities. Each sequential line-scan appears beneath the previous one, with time advancing from top to bottom. RBCs appear as continuous diagonal streaks in the space-time image when RBC velocities are relatively slow compared to the line-scan rate. *Bottom,* space-time image of *in vivo* line-scan data where RBCs appear as continuous dark streaks. Previous analytical methods have determined velocities by calculating the inverse slope of the streaks. **B,** *Top,* schematic of line-scan data of fast RBC velocities. RBCs may appear as discontinuous streaks or as just a few dark spots in the space-time image. The large number of RBCs confounds identification of individual streaks. *Bottom,* space-time image of *in vivo* line-scan data where RBCs velocity is high relative to the line-scan rate.

As the velocities of the RBCs increase relative to the line-scanning rate, the cell images no longer create discernable streaks. At high velocities (as we observe in arteriovenous shunts), the SVD and Radon transform-based approaches no longer work. To overcome this limitation, we developed a method to analyze the same space-time data irrespective of the slope produced by moving RBCs. This alternative approach is described in Chapter 3.

REFERENCES

1 Denk, W., Strickler, J. H. & Webb, W. W. Two-photon laser scanning fluorescence microscopy. *Science* **248**, 73-76 (1990).

2 Helmchen, F. & Denk, W. Deep tissue two-photon microscopy. *Nat Methods* **2**, 932-940, doi:10.1038/nmeth818 (2005).

3 Davy, A., Bush, J. O. & Soriano, P. Inhibition of gap junction communication at ectopic Eph/ephrin boundaries underlies craniofrontonasal syndrome. *PLoS Biol* **4**, e315, doi:06-PLBI-RA-0452R3 [pii] 10.1371/journal.pbio.0040315 (2006).

4 Muzumdar, M. D., Tasic, B., Miyamichi, K., Li, L. & Luo, L. A global double-fluorescent Cre reporter mouse. *Genesis* **45**, 593-605, doi:10.1002/dvg.20335 (2007).

5 Gossen, M. & Bujard, H. Studying gene function in eukaryotes by conditional gene inactivation. *Annu Rev Genet* **36**, 153-173, doi:10.1146/annurev.genet.36.041002.120114 (2002).

6 Carlson, T. R. *et al.* Endothelial expression of constitutively active Notch4 elicits reversible arteriovenous malformations in adult mice. *Proc Natl Acad Sci U S A* **102**, 9884-9889 (2005).

7 Murphy, P. A. *et al.* Endothelial Notch4 signaling induces hallmarks of brain arteriovenous malformations in mice. *Proc Natl Acad Sci U S A* **105**, 10901-10906 (2008).

8 Feil, R. *et al.* Ligand-activated site-specific recombination in mice. *Proceedings of the National Academy of Sciences of the United States of America* **93**, 10887-10890 (1996).

9 Indra, A. K. *et al.* Temporally-controlled site-specific mutagenesis in the basal layer of the epidermis: comparison of the recombinase activity of the tamoxifen-inducible Cre-ER(T) and Cre-ER(T2) recombinases. *Nucleic Acids Res* **27**, 4324-4327 (1999).

10 Claxton, S. *et al.* Efficient, inducible Cre-recombinase activation in vascular endothelium. *Genesis* **46**, 74-80, doi:10.1002/dvg.20367 (2008).

11 Wang, Y. *et al.* Ephrin-B2 controls VEGF-induced angiogenesis and lymphangiogenesis. *Nature* **465**, 483-486, doi:10.1038/nature09002 (2010).

12 Pitulescu, M. E., Schmidt, I., Benedito, R. & Adams, R. H. Inducible gene targeting in the neonatal vasculature and analysis of retinal angiogenesis in mice. *Nat Protoc* **5**, 1518-1534, doi:10.1038/nprot.2010.113 (2010).

13 Wang, L. *et al.* Restricted expression of mutant SOD1 in spinal motor neurons and interneurons induces motor neuron pathology. *Neurobiol Dis* **29**, 400-408, doi:10.1016/j.nbd.2007.10.004 (2008).

14 Gulati, S., Muller, S. J. & Liepmann, D. Direct measurements of viscoelastic flows of DNA in a 2:1 abrupt planar micro-contraction. *Journal of Non-Newtonian Fluid Mechanics* **155**, 51-66 (2008).

15 Willert, C. E. & M., G. Digital particle image velocimetry. *Experiments in Fluids* **10**, 181-193 (1991).

16 Dunn, A. K., Bolay, H., Moskowitz, M. A. & Boas, D. A. Dynamic imaging of cerebral blood flow using laser speckle. *J Cereb Blood Flow Metab* **21**, 195-201, doi:10.1097/00004647-200103000-00002 (2001).

17 Srinivasan, V. J. *et al.* Optical coherence tomography for the quantitative study of cerebrovascular physiology. *J Cereb Blood Flow Metab* **31**, 1339-1345, doi:10.1038/jcbfm.2011.19 (2011).

18 Santisakultarm, T. P. & Schaffer, C. B. Optically quantified cerebral blood flow. *J Cereb Blood Flow Metab* **31**, 1337-1338, doi:10.1038/jcbfm.2011.18 (2011).

19 Drew, P. J., Blinder, P., Cauwenberghs, G., Shih, A. Y. & Kleinfeld, D. Rapid determination of particle velocity from space-time images using the Radon transform. *J Comput Neurosci* **29**, 5-11, doi:10.1007/s10827-009-0159-1 (2010).

20 Jones, E. A., Baron, M. H., Fraser, S. E. & Dickinson, M. E. Measuring hemodynamic changes during mammalian development. *Am J Physiol Heart Circ Physiol* **287**, H1561-1569, doi:10.1152/ajpheart.00081.2004 (2004).

21 Kleinfeld, D., Mitra, P. P., Helmchen, F. & Denk, W. Fluctuations and stimulus-induced changes in blood flow observed in individual capillaries in layers 2 through 4 of rat neocortex. *Proceedings of the National Academy of Sciences of the United States of America* **95**, 15741-15746 (1998).

22 Nishimura, N. *et al.* Targeted insult to subsurface cortical blood vessels using ultrashort laser pulses: three models of stroke. *Nat Methods* **3**, 99-108, doi:10.1038/nmeth844 (2006).

23 Schaffer, C. B. *et al.* Two-photon imaging of cortical surface microvessels reveals a robust redistribution in blood flow after vascular occlusion. *PLoS Biol* **4**, e22, doi:10.1371/journal.pbio.0040022 (2006).

24 Kamoun, W. S. *et al.* Simultaneous measurement of RBC velocity, flux, hematocrit and shear rate in vascular networks. *Nat Methods* **7**, 655-660, doi:10.1038/nmeth.1475 (2010).

III

Line-Scanning Particle Image Velocimetry: an Optical Approach for Quantifying a Wide Range of Blood Flow Speeds in Live Animals

Tyson N. Kim, Patrick W. Goodwill, Yeni Chen, Steven M. Conolly, Chris B. Schaffer, Dorian Liepmann, Rong A. Wang

Affiliations:

Laboratory for Accelerated Vascular Research, Division of Vascular Surgery, Department of Surgery, University of California, San Francisco, United States of America (T.N.K., Y.C., R.A.W); Department of Bioengineering, University of California, Berkeley, United States of America (P.W.G, S.M.C, D.L.); Department of Biomedical Engineering, Cornell University, United States of America (C.B.S)

Correspondence to:

Rong A. Wang, PhD, Department of Surgery, HSW 1618, Box 0507, 513 Parnassus Avenue, San Francisco, CA 94143-0507. Tel 415-476-6855. Fax 415-564-5698. E-mail rong.wang@ucsfmedctr.org

Abstract

Background: The ability to measure blood velocities is critical for studying vascular development, physiology, and pathology. A key challenge is to quantify a wide range of blood velocities in vessels deep within living specimens with concurrent high-resolution imaging of vascular cells. Two-photon laser scanning microscopy (TPLSM) has shown tremendous promise in analyzing blood velocities hundreds of micrometers deep in animals with cellular resolution. However, current TPLSM-based approaches are limited to the lower range of blood velocities and are not adequate to study faster velocities in many normal or disease conditions.

Methodology/Principal Findings: We developed line-scanning particle image velocimetry (LS-PIV) using TPLSM and quantified peak blood velocities up to 84 mm/s in live mice harboring brain arteriovenous malformation, a disease characterized by high flow. With this method, we were able to accurately detect the elevated blood velocities and exaggerated pulsatility along the abnormal vascular network in these animals. LS-PIV robustly analyzed noisy data from vessels as deep as 850 μm below the brain surface. In addition to analyzing *in vivo* data, we validated the true accuracy of LS-PIV up to 800 mm/s using simulations with known velocity and noise parameters.

Conclusions/Significance: To our knowledge, these blood velocity measurements are the fastest recorded with TPLSM. Partnered with transgenic mice carrying cell-specific fluorescent reporters, LS-PIV will also enable the direct *in vivo* correlation of cellular,

biochemical, and hemodynamic parameters in high flow vascular development and diseases such as atherogenesis, arteriogenesis, and vascular anomalies.

Introduction

A functional vascular supply is critical for efficient transport of nutrients, fluids, signaling molecules, and circulating cells between tissues and organs in the vertebrate system. Lack of appropriate vascular development and maintenance contributes to the pathogenesis of many diseases and can involve excess angiogenesis, abnormal remodeling, and insufficient growth or regression of vessels [1,2,3]. Importantly, hemodynamic forces have long been recognized to play a defining role in shaping blood vessels [4,5] and in mediating vascular disease. Surgical manipulation of blood flow can cause abnormalities in heart and vessel development [6,7] and primary defects in heart contractility have detrimental effects on vessel and cardiac remodeling [8,9,10]. Recent studies have also identified genetic programs involved in specifying arteries and veins prior to circulation [11,12], raising important questions on the interplay of genetic and hemodynamic cues in arteriovenous development and plasticity. This interplay is enigmatic yet critical toward understanding vascular diseases such as arteriovenous malformation (AVM), an often dangerous condition characterized by enlarged, tangled shunts that bypass normal capillary beds. These high-flow lesions are believed to persist and enlarge under the influence of hemodynamic forces [13,14], yet little direct evidence links flow with cellular and molecular mechanisms for their pathogenesis. The ability to correlate blood flow with cellular and molecular-level dynamics in living animals would improve our understanding of vascular development and disease. However, a key obstacle has been the inability to quantify high blood velocities in individual vessels deep in living specimens with concurrent high-resolution imaging of vascular cells.

Video-rate imaging methods have been widely used for measuring blood flow within microvessels [15,16] and microfluidic devices [17,18] but perform poorly when focusing deep into biological tissue due to severe image blurring imposed by light-scattering. For this reason, two-photon laser scanning microscopy (TPLSM) has been the tool of choice for studying hemodynamics at the resolution of individual capillaries in mice and rats [19], because it can penetrate hundreds of micrometers by mitigating the effects of light-scattering on image generation [20,21,22]. However, this depth imaging ability comes at the cost of imaging speed and has hindered the quantification of faster blood velocities. Thus, previous investigations using TPLSM have generally focused on blood velocities under 10 mm/s, although one study reported analysis up to 35 mm/s [23]. The adult mouse harbors far greater blood velocities throughout the body that can exceed 180 mm/s in the carotid artery [24] and 500 mm/s in the suprarenal aorta [25,26]. The ability to analyze a large range of blood velocities in mice with microscopic resolution and deep imaging would enable detailed correlation of cellular, molecular, and local hemodynamic cues in high-flow processes such as atherogenesis, arteriogenesis, and AVM.

TPLSM and confocal line-scan geometries have been used to track red blood cell (RBC) motion in a vessel-specific [19,27,28,29,30] or multi-vessel [31] fashion. Line-scanning can acquire substantially more frames per second than two-dimensional imaging and, when oriented along the length of a vessel, can resolve RBC motion over relatively large distances. Typically, sequential scans are visualized as a space-time image with distance on the abscissa and time advancing downward on the ordinate. The blood plasma is loaded with fluorescent dye, allowing individual RBCs to appear as dark spots. These dark spots produce streaks in the space-time data if there is sufficient overlap of the same RBCs between scans. The slope of each streak is inversely proportional to the cell's speed and previous methods have quantified moderate blood velocities by determining the angle of the streaks [19,27]. However, as the velocities of the RBCs increase relative to the line-scanning rate, the cell images no longer create discernable streaks.

To overcome this limitation, we developed a method to analyze a significantly wider range of velocities using TPLSM or confocal microscopy. Line-scanning particle image velocimetry (LS-PIV) determines the RBC displacements between pairs of line-scans. Here we describe the operating principles of LS-PIV and test its robustness to noise and increasing blood flow speed. We demonstrate the power of this technique by quantifying blood flow velocities with high temporal and spatial resolution within a mouse model of brain AVM [32,33].

Methods

Full experimental details are provided in the Supplemental Materials.

Mice

This study was carried out in strict accordance with NIH regulations and the Institutional Animal Care and Use Committee at the University of California San Francisco. The protocol was approved by the IACUC at UCSF (Approval Number: AN085404-01). *Tie2-tTA* and *TRE-Notch4** mice were generated by our lab as previously described [32] and crossed to produce mice harboring brain AVMs [33]. Tetracycline sucrose water (0.5 mg/mL Tetracycline hydrochloride, Sigma, and 50 mg/mL D-sucrose, Fisher BioReagents) was administered to pregnant mothers and withdrawn when pups were born to allow expression of endothelial Notch4* in neonates. Wild-type mice were used to study normal brain vasculature. *Ephrin-B2*$^{+/H2B\text{-}eGFP}$ mice [34] were kindly provided by the Soriano lab and aided with *in vivo* visualization of arterial endothelium with cellular resolution. Mice were backcrossed into FVB/N by nine generations or greater.

***In Vivo* Imaging**

TPLSM imaging of mouse brain was performed as previously described [35]. In brief, three week-old mice were anesthetized with 0.5-2% isoflurane in 2 L/min of oxygen and warmed with a homeothermic blanket (Harvard Apparatus). The head was immobilized with a stereotax (myNeuroLab.com) for surgery and imaging. The scalp was treated with betadine and given subcutaneous injection of 0.125% bupivacaine prior to surgery. A small craniotomy was performed over the right cortex, bathed in artificial cerebral spinal fluid, covered with a 5 mm coverglass (World Precision Instruments), and sealed with dental acrylic (Lang Dental) to provide optical access to the brain. Mice were administered with subcutaneous injections of 0.1 mg/kg buprenorphine pre-operatively and twice daily for three days. For imaging, the blood was fluorescently labeled with 2000 KDa Texas Red-dextran that was prepared according to a published protocol [36] and filtered with 1000 KDa dialysis tubing (Spectrum Labs).

Texas Red and GFP fluorescence were excited simultaneously using low-energy femtosecond laser pulses centered at 870 nm (Mai Tai HP, Newport Spectra-Physics). Images and line-scan data were obtained with a locally constructed two-photon laser scanning microscope (Supplemental Materials and Figure S1) using a long working distance 1.0 NA water dipping objective (Zeiss) and MPScope 1.0 software [37] to control the microscope and record data.

LS-PIV implemented with TPLSM

Figure 1 illustrates the operating principles of LS-PIV. In brief, line-scans were recorded at 2.6 kHz along the central axis of vessels. The data was cropped to a region-of-interest (ROI) along a straight segment of each vessel, with a typical length of 10 μm for capillaries and 50 μm or greater for arteries. Displacement of RBCs between sequential line-scans was determined from their cross-correlation. The shift from the origin to the center of the peak of the cross-correlation is a measure of the spatial shift of RBCs between image frames. Because the line-scan trajectory was pre-selected, multiple RBCs within the imaging field collectively contributed to the strength of the velocity calculation per time point. To determine the shift with maximum accuracy, the peak was fitted with a Gaussian distribution. The shift in pixels was then converted to velocity by dividing by the time interval between the line-scans. All operations were executed in 32-bit Matlab (Mathworks) and are further described in the Supplemental Materials.

Results

Operational principles of LS-PIV

We initially found that existing TPLSM-based methods could not quantify RBC velocities in large brain AVMs of Notch4* mice. RBCs often moved too quickly to be tracked as individual streaks in the space-time data (Figure S2A-B). However, we reasoned that many of the same cells were re-imaged in sequential line-scans and could still be used to analyze velocity. We therefore developed LS-PIV and first tested it in cortical arteries with moderate RBC speeds. Figure 2 shows analysis of line-scan data measured from an arterial segment in a collateral loop. These cerebral collateral vessels were ideal for early tests as they generally harbored lower RBC velocities than similarly sized arteries in arborizing networks. Arteries were identified by their morphology, direction of flow, and endothelial expression of histone-tagged GFP under control of the endogenous promoter for arterial marker *ephrin-B2* [34] (N=34 vessels in 3 mice, Figure 2A). The blood plasma was labeled with high-molecular-weight Texas Red-dextran and the cortical vasculature was imaged through a cranial window over the right parietal cortex. Image stacks were acquired with 1 μm steps along the optical axis and visualized as average projections (Figure 2A).

Line-scans were recorded along the central axis of vessels and analyzed in a ROI of 50 μm corresponding to 3-4 endothelial cells along the adjacent wall (Figure 2B). These data were organized into space-time images with time advancing downward on the ordinate and with distance on the abscissa. Individual RBCs appeared as dark streaks at these moderate velocities (Figure 2C). LS-PIV was applied between every pair of sequential line-scans to produce a running cross-correlation of RBC motion. The initial result was converted to a probability distribution with units of mm/s by dividing by the scan interval (Figure 2D). The final velocity for each time-point was calculated from the most probable value in the corresponding correlation (Figure 2E). These results demonstrated that LS-PIV could analyze RBC velocities without the need to modify existing TPLSM or surgical preparation. Additionally, LS-PIV provided exceptional temporal resolution equal to the line-scan rate (2.6 kHz on our system) and made it easy to see heartbeats and rapid changes in blood velocity.

Performance of LS-PIV with increasing noise and velocity

We sought to validate LS-PIV under demanding conditions using both *in vivo* and simulation data. Previous methods were constrained by their range of analyzable flow speeds or by depth-dependent image quality. We therefore tested the performance of LS-PIV under different signal-to-noise ratios (SNR) and increasing RBC velocity. A major source of image noise in TPLSM results from laser scatter and production of extra-focal fluorescence as the imaging plane is positioned deeper into the specimen [20,38]. We found that utilizing Texas Red-dextran to label the plasma allowed for deeper imaging depths than fluorescein-dextran (data not shown), likely because of Texas Red-dextran's large two-photon cross-section and low absorption of red fluorescence by the blood. SNR values were determined from the raw line-scan data in individual vessels using the contrast of RBCs amid the fluorescent plasma. Typical best data was acquired at the surface of the brain and had an SNR of ~8. High noise data, generally obtained hundreds of micrometers below the surface, had an SNR of ~2 or less. Figure 3A-B shows increasing noise from progressively deeper imaging in the living brain and LS-PIV analysis down to 850 μm using line-scan data with an SNR of 2.2. To our knowledge, these RBC velocity measurements are the deepest ones recorded with TPLSM without the use of amplified [39] or longer wavelength femtosecond laser pulses [40], and demonstrate the robustness of LS-PIV with well-established imaging parameters.

Next, we examined the true accuracy and range of LS-PIV using simulated line-scan data where it was possible to precisely define velocity and noise parameters (Figure 4A). These data were generated using a randomized distribution of particles that was shifted in known spatial increments over time. The size of each particle was further randomized between 1 to 7 μm to mimic RBCs at different orientations and positions relative to the scan line. Speed was increased with oscillations at 10 Hz to simulate mouse heart rate, and normally distributed noise was added for typical best or very poor data corresponding to an SNR of 8 or 1, respectively. Under both noise conditions, LS-PIV accurately quantified velocities above previously reported values using a ROI of 100 μm (Figure 4B). Actual velocities are displayed as a dark blue line, analysis of corresponding data with an SNR of 8 is displayed with light blue dots, and analysis of corresponding data with an SNR of 1 is displayed with red dots (Figure 4B). LS-PIV demonstrated high fidelity beyond 150 mm/s using the data with an SNR of 8, and with gradually increasing error after 50 mm/s using the poor data with an SNR of 1. This error manifested as increased scatter and the appearance of distinct outliers corresponding with rapid changes in high velocity (Figure 4B, arrows). Outliers are a common occurrence in PIV data and can be removed using median filters [18]. We further tested LS-PIV with SNRs ranging from 0.33 to 8 and validated these results with analysis using singular valued decomposition (SVD) [19], demonstrating good agreement with the previous method at lower velocities (Figure S3). Importantly, LS-PIV works well at high velocities and with low signal-to-noise conditions. As a practical upper limit, LS-PIV could analyze speeds up to 800 mm/s using an ROI of 426 μm (Figure S4A). LS-PIV performed well under capillary-level velocities and in periodic reversals in flow direction (Figure S4B).

We found that RBC displacement in capillaries was often small compared to the pixel resolution of the microscope when two sequential line-scans were compared, which potentially decreased the accuracy of the speed determination. We eliminated this inherent error in the raw data by processing non-neighboring line-scans in time (i.e., every line-scan with its 5th neighboring scan) thereby increasing the delay between cross-correlated line-scans and allowing RBC displacement to be large enough to resolve. Thus, LS-PIV has a large dynamic range and enables TPLSM-based quantification of high RBC velocities while maintaining the ability to study spatiotemporal hemodynamics in individual capillaries.

Analysis of RBC velocities in normal and AVM cerebrovasculature

Functional implementation of TPLSM has made it possible to study hemodynamics in living organisms with extremely high detail. However, previous investigations could quantify only the lower range of blood velocities typically found in rodents. We were interested in using LS-PIV to investigate hemodynamics in a mouse model of Notch-mediated AVM and quantifying the fastest reported RBC velocities measured by *in vivo* TPLSM.

We first measured RBC velocities within major artery-to-vein networks overlying the cortex of control mice (N=28 vessels in 3 mice, Figure 5A-B). The blood plasma was labeled with Texas Red-dextran and arteriovenous identity of vessels was determined by their morphology and flow direction. Line-scans were then recorded along the central axis of contiguous vessel segments between a major branch of the middle cerebral artery and a surface vein draining to the superior sagittal sinus (Figure 5A'-B'). Representative analyses in a subset of these vessels are displayed (Figure 5C). We found that LS-PIV clearly resolved peak arterial velocities up to 44 mm/s in controls (the fastest we measured) as well as slow capillary velocities, which were typically below 2 mm/s. Flow remained pulsatile due to heartbeat in all measured vessels, including capillaries and venules. RBC velocity progressively decreased from arteries to capillaries and thereafter increased modestly as flow coalesced into major veins. A slower ~0.5-2 Hz modulation in RBC speed corresponded with the respiratory rate of the anesthetized animals and was extracted from analysis of arteries or veins (data not shown).

We next combined *in vivo* TPLSM with a mouse model of Notch-mediated AVMs [33] and directly investigated hemodynamics within the aberrant artery-to-vein topology in the brain. The most important determinant of hemodynamics within an AVM is its resistance to blood flow. This is largely dependent on the narrowest cross-sectional point along the flow path, where increases in diameter result in dramatic loss of resistance and from which many pathophysiological phenomena of AVMs are speculated to follow [13]. We therefore identified individual arteriovenous shunts and measured center axis velocities in contiguous vessel segments in both the up- and down-stream pathways (N=42 vessels in 3 mice, Figure 6A). These vessels were tortuous and dramatically enlarged. Representative analyses in a subset of these vessels are displayed in Figure 6B. We found that LS-PIV clearly resolved peak RBC velocities up to 84 mm/s (the fastest we measured) and that velocities were elevated and markedly pulsatile within all compartments of the vasculature. Interestingly, velocities often spiked within AV shunts (Figure 6B, purple segments) compared with up- and down-stream segments. These shunts exhibited laminar flow when we examined their average, peak systolic, and end-diastolic spatial flow profiles (Figure S5). Average RBC velocities progressively decreased toward and from the AV shunts within the measurable field (Figure 6A'), without increasing again in the coalescing veins. These results highlight the impact that shunts have on hemodynamics within the arteriovenous network and demonstrate the utility of LS-PIV in studying a wide range of flow speeds with microscopic resolution.

Discussion

Advances in genetic labeling techniques and functional imaging approaches have helped establish TPLSM and confocal microscopy as a powerful, noninvasive ways to study vascular biology in whole-tissue explants and living organisms [20,21,22,28]. Hemodynamics have been investigated with capillary-level resolution in brain [19], kidney [41], and tumor [42,43]. However, the adult mouse harbors far faster RBC velocities than can be analyzed by previous TPLSM- or confocal-based methods. LS-PIV enables analysis of a wide range of RBC velocities by easy integration with well-established *in vivo* imaging and line-scan acquisition approaches. We demonstrated the utility of this method by robustly quantifying blood velocities in a mouse model of brain AVM. To our knowledge, these are the fastest RBC velocities analyzed using multi-photon or confocal microscopy. Our simulations indicate that LS-PIV may analyze velocities from capillaries to greater than 800 mm/s, potentially covering the full range of blood velocities generated in mice [25,26].

An important feature of LS-PIV is its ability to resolve the spatial flow profile within individual vessels. As a proof-of-principle, we measured the flow in a control artery and a Notch-mediated AV shunt by acquiring multiple axial line-scans spaced every few micrometers across the diameters of their lumens (Figure S5). Complete profile measurements took roughly 10-15 minutes, which could be drastically shortened by using pre-patterned line-scan arrays and reducing the number of scans per vessel. Such systematic approaches, combined with the temporal resolution of LS-PIV, allow for quantification of pulsatile dynamics including the spatial profiles of peak systolic and end-diastolic flow (Figure S5). These highly resolved measurements have the potential to address long-standing questions on how local hemodynamic forces influence endothelium and vascular development *in vivo*. For example, it is established from *in vitro* studies that hemodynamic shear stress regulates endothelial cell proliferation, shape, alignment, and gene expression [44,45,46,47]. Arterial and pulsatile waveforms regulate ‘athero-prone’ and ‘athero-protective’ genes [48,49] suggesting that peak systolic or end-diastolic shear forces may be important stimuli for flow-responsive programs. There is currently no method to correlate high shear rates from fast blood flow directly with cellular-level dynamics and vascular remodeling in animals. Application of LS-PIV in a systematic fashion will shed light on the role of high pulsatile shear in vessel development, maintenance, and disease.

LS-PIV may be combined with a growing number of transgenic approaches to study the relationship between hemodynamics, cellular behavior, and biochemical signaling *in vivo*. For example, *ephrin-B2*$^{+/H2B\text{-}eGFP}$ mice [34] allow visualization of arterial endothelium with cellular resolution by TPLSM (Figure 2A-B) which could be used to track these cells over time. Tissue-specific and temporally inducible methods may be used to test the role of key biochemical constituents on vessel maintenance or malformation within various hemodynamics environments. We use the *Tie2-tTA* and *TRE-Notch4** mice [32,33] to express Notch4* in endothelium of post-natal mice. Combining LS-PIV with such genetic approaches will be helpful in studying the role of hemodynamic cues in developmental programs.

An important limitation of TPLSM has traditionally been its slow scanning rate along the optical ('z') axis, which has been achieved by translating the position of the sample relative to the objective lens with a stepper motor. While sufficient for three-dimensional imaging, this approach has considerable inertial constraints that prevent rapid laser scanning oblique to the ('xy') image plane. Two previous approaches have attempted to obviate the need for rapid scanning along the optical axis to quantify blood flow in three-dimensions: residence time line scanning (RTLS) velocimetry [31] and Doppler optical coherence tomography (DOCT) [50]. RTLS velocimetry extrapolates RBC velocities at all orientations from two-photon line-scans collected in the 'xy' plane. This analysis utilizes the angle between the scan line and vessel axis, and the residence time of the RBCs as they pass the scan region. However, RTLS will not work to calculate high velocities at oblique angles because RBCs pass too quickly through the scan line to be imaged more than once. Alternatively, DOCT can quantify blood flow in three-dimensions and simultaneously across many vessels by measuring the Doppler shift of light scattered off moving RBCs. Though a powerful approach for measuring network flow in an unbiased fashion, DOCT is currently applicable to speeds under 10 mm/s, and in larger vessels rather than capillaries [51]. Additional methods are required to analyze high RBC velocities with microscopic resolution in three-dimensions. Recently, rapid three-dimensional scanning has been achieved using acousto-optic deflectors (AOD) to steer the laser beam without moving the animal or the objective lens [52]. This approach reportedly has an effective scan range of 50 μm along the optical axis using a high numerical aperture objective, which would be sufficient for direct line-scan measurements of a wide range of RBC velocities. Implementation of three-dimensional AOD scanning with LS-PIV would enable analysis of high blood velocities in all orientations.

In conclusion, TPLSM has been the tool of choice for studying hemodynamics with capillary-level resolution and large penetration depths, but has traditionally been limited to studying slow blood flows. We have developed LS-PIV, which may be easily integrated with well-established *in vivo* imaging and line-scan data acquisition approaches, in order to quantify higher blood velocities with TPLSM or confocal microscopy. LS-PIV performed robustly with noisy data in vessels as deep as 850 μm below the brain surface and with very high accuracy as validated with simulation data. As a proof of principle, we investigated blood velocities within the vascular network of brain AVM in mice. LS-PIV is uniquely suited to study high RBC velocities with optical resolution deep in living animals. Partnered with transgenic mice with cell-specific fluorescent reporters or with exogenous dyes, LS-PIV will enable the direct *in vivo* correlation of cellular, biochemical, and hemodynamic cues in high flow processes such as atherogenesis, arteriogenesis, and AVMs.

Acknowledgements

We thank Morgan Anderson for technical assistance with experiments and analysis of data. We thank Dr. Corinne Nielsen, Dr. Marc Bolliger, Dr. Henrik Lindskog, and Pamela Derish for their critical readings and discussions.

Sources of Funding

This work was supported by the Foundation for Accelerated Vascular Research (formerly the Pacific Vascular Research Foundation) and the Frank A. Campini Foundation, the Mildred V. Strouss Trust, NIH R01 HL075033, NIH R01 NS067420, and American Heart Association Grant in Aid 10GRNT4170146 (to R.A.W), the NIH T32 GM07618 (to UCSF MSTP), the Tobacco-Related Disease Research Program Fellowship 19DT-0007 and NIH F30 1F30HL099005 (to T.N.K).

Disclosures

None.

References

1. Carmeliet P (2003) Angiogenesis in health and disease. Nat Med 9: 653-660.
2. Jain RK (2003) Molecular regulation of vessel maturation. Nat Med 9: 685-693.
3. Adams RH, Alitalo K (2007) Molecular regulation of angiogenesis and lymphangiogenesis. Nat Rev Mol Cell Biol 8: 464-478.
4. Murray CD (1926) The Physiological Principle of Minimum Work Applied to the Angle of Branching of Arteries. J Gen Physiol 9: 835-841.
5. Murray CD (1926) The Physiological Principle of Minimum Work: I. The Vascular System and the Cost of Blood Volume. Proc Natl Acad Sci U S A 12: 207-214.
6. Kurz H (2000) Physiology of angiogenesis. J Neurooncol 50: 17-35.
7. le Noble F, Moyon D, Pardanaud L, Yuan L, Djonov V, et al. (2004) Flow regulates arterial-venous differentiation in the chick embryo yolk sac. Development 131: 361-375.
8. Conway SJ, Kruzynska-Frejtag A, Kneer PL, Machnicki M, Koushik SV (2003) What cardiovascular defect does my prenatal mouse mutant have, and why? Genesis 35: 1-21.
9. Huang C, Sheikh F, Hollander M, Cai C, Becker D, et al. (2003) Embryonic atrial function is essential for mouse embryogenesis, cardiac morphogenesis and angiogenesis. Development 130: 6111-6119.
10. Lucitti JL, Jones EA, Huang C, Chen J, Fraser SE, et al. (2007) Vascular remodeling of the mouse yolk sac requires hemodynamic force. Development 134: 3317-3326.
11. Herbert SP, Huisken J, Kim TN, Feldman ME, Houseman BT, et al. (2009) Arterial-venous segregation by selective cell sprouting: an alternative mode of blood vessel formation. Science 326: 294-298.
12. Wang HU, Chen ZF, Anderson DJ (1998) Molecular distinction and angiogenic interaction between embryonic arteries and veins revealed by ephrin-B2 and its receptor Eph-B4. Cell 93: 741-753.
13. Morgan M, Winder M (2001) Haemodynamics of arteriovenous malformations of the brain and consequences of resection: a review. J Clin Neurosci 8: 216-224.
14. Corti P, Young S, Chen CY, Patrick MJ, Rochon ER, et al. (2011) Interaction between alk1 and blood flow in the development of arteriovenous malformations. Development 138: 1573-1582.
15. Kamoun WS, Schmugge SJ, Kraftchick JP, Clemens MG, Shin MC (2008) Liver microcirculation analysis by red blood cell motion modeling in intravital microscopy images. IEEE Trans Biomed Eng 55: 162-170.

16. Rosenblum WI, El-Sabban F (1981) Measurement of red cell velocity with a two-slit technique and cross-correlation: use of reflected light, and either regulated dc or unregulated ac power supplies. Microvasc Res 22: 225-227.
17. Gulati S, Muller SJ, Liepmann D (2008) Direct measurements of viscoelastic flows of DNA in a 2:1 abrupt planar micro-contraction. J Non-Newtonian Fluid Mech 155: 51-66.
18. Willert CE, M. G (1991) Digital particle image velocimetry. Exp Fluids 10: 181-193.
19. Kleinfeld D, Mitra PP, Helmchen F, Denk W (1998) Fluctuations and stimulus-induced changes in blood flow observed in individual capillaries in layers 2 through 4 of rat neocortex. Proc Natl Acad Sci U S A 95: 15741-15746.
20. Helmchen F, Denk W (2005) Deep tissue two-photon microscopy. Nat Methods 2: 932-940.
21. Rubart M (2004) Two-photon microscopy of cells and tissue. Circ Res 95: 1154-1166.
22. Zipfel WR, Williams RM, Webb WW (2003) Nonlinear magic: multiphoton microscopy in the biosciences. Nat Biotechnol 21: 1369-1377.
23. Shih AY, Friedman B, Drew PJ, Tsai PS, Lyden PD, et al. (2009) Active dilation of penetrating arterioles restores red blood cell flux to penumbral neocortex after focal stroke. J Cereb Blood Flow Metab 29: 738-751.
24. Parzy E, Miraux S, Franconi JM, Thiaudiere E (2009) In vivo quantification of blood velocity in mouse carotid and pulmonary arteries by ECG-triggered 3D time-resolved magnetic resonance angiography. NMR Biomed 22: 532-537.
25. Amirbekian S, Long RC, Jr., Consolini MA, Suo J, Willett NJ, et al. (2009) In vivo assessment of blood flow patterns in abdominal aorta of mice with MRI: implications for AAA localization. Am J Physiol Heart Circ Physiol 297: H1290-1295.
26. Huo Y, Guo X, Kassab GS (2008) The flow field along the entire length of mouse aorta and primary branches. Ann Biomed Eng 36: 685-699.
27. Drew PJ, Blinder P, Cauwenberghs G, Shih AY, Kleinfeld D (2010) Rapid determination of particle velocity from space-time images using the Radon transform. J Comput Neurosci 29: 5-11.
28. Jones EA, Baron MH, Fraser SE, Dickinson ME (2004) Measuring hemodynamic changes during mammalian development. Am J Physiol Heart Circ Physiol 287: H1561-1569.
29. Nishimura N, Schaffer CB, Friedman B, Tsai PS, Lyden PD, et al. (2006) Targeted insult to subsurface cortical blood vessels using ultrashort laser pulses: three models of stroke. Nat Methods 3: 99-108.
30. Schaffer CB, Friedman B, Nishimura N, Schroeder LF, Tsai PS, et al. (2006) Two-photon imaging of cortical surface microvessels reveals a robust redistribution in blood flow after vascular occlusion. PLoS Bio 4: e22.
31. Kamoun WS, Chae SS, Lacorre DA, Tyrrell JA, Mitre M, et al. (2010) Simultaneous measurement of RBC velocity, flux, hematocrit and shear rate in vascular networks. Nat Methods 7: 655-660.
32. Carlson TR, Yan Y, Wu X, Lam MT, Tang GL, et al. (2005) Endothelial expression of constitutively active Notch4 elicits reversible arteriovenous malformations in adult mice. Proc Natl Acad Sci U S A 102: 9884-9889.

33. Murphy PA, Lam MT, Wu X, Kim TN, Vartanian SM, et al. (2008) Endothelial Notch4 signaling induces hallmarks of brain arteriovenous malformations in mice. Proc Natl Acad Sci U S A 105: 10901-10906.
34. Davy A, Bush JO, Soriano P (2006) Inhibition of gap junction communication at ectopic Eph/ephrin boundaries underlies craniofrontonasal syndrome. PLoS Biol 4: e315.
35. Kleinfeld D, Denk W (2000) Two-photon imaging of neocortical micro-circulation. In: Yuste R, Lanni F, Konnerth A, eds. Imaging neurons: A laboratory manual. Cold Spring Harbor, New York: Cold Spring Harbor Laboratory Press 231-2315.
36. Hornig S, Christoph B, Gafe A, Wotschadlo J, Liebert T, et al. (2008) Biocompatible fluorescent nanoparticles for pH-sensoring. Soft Matter 4: 1169-1172.
37. Nguyen QT, Tsai PS, Kleinfeld D (2006) MPScope: a versatile software suite for multiphoton microscopy. J Neurosci Methods 156: 351-359.
38. Oheim M, Beaurepaire E, Chaigneau E, Mertz J, Charpak S (2001) Two-photon microscopy in brain tissue: parameters influencing the imaging depth. J Neurosci Methods 111: 29-37.
39. Theer P, Hasan MT, Denk W (2003) Two-photon imaging to a depth of 1000 microm in living brains by use of a Ti:Al2O3 regenerative amplifier. Opt Lett 28: 1022-1024.
40. Kobat D, Durst ME, Nishimura N, Wong AW, Schaffer CB, et al. (2009) Deep tissue multiphoton microscopy using longer wavelength excitation. Opt Express 17: 13354-13364.
41. Kang JJ, Toma I, Sipos A, McCulloch F, Peti-Peterdi J (2006) Quantitative imaging of basic functions in renal (patho)physiology. Am J Physiol Renal Physiol 291: F495-502.
42. Brown EB, Campbell RB, Tsuzuki Y, Xu L, Carmeliet P, et al. (2001) In vivo measurement of gene expression, angiogenesis and physiological function in tumors using multiphoton laser scanning microscopy. Nat Med 7: 864-868.
43. Kashiwagi S, Tsukada K, Xu L, Miyazaki J, Kozin SV, et al. (2008) Perivascular nitric oxide gradients normalize tumor vasculature. Nat Med 14: 255-257.
44. Chien S (2007) Mechanotransduction and endothelial cell homeostasis: the wisdom of the cell. Am J Physiol Heart Circ Physiol 292: H1209-1224.
45. Tzima E, Irani-Tehrani M, Kiosses WB, Dejana E, Schultz DA, et al. (2005) A mechanosensory complex that mediates the endothelial cell response to fluid shear stress. Nature 437: 426-431.
46. Li YS, Haga JH, Chien S (2005) Molecular basis of the effects of shear stress on vascular endothelial cells. J Biomech 38: 1949-1971.
47. del Alamo JC, Norwich GN, Li YS, Lasheras JC, Chien S (2008) Anisotropic rheology and directional mechanotransduction in vascular endothelial cells. Proc Natl Acad Sci U S A 105: 15411-15416.
48. Dai G, Kaazempur-Mofrad MR, Natarajan S, Zhang Y, Vaughn S, et al. (2004) Distinct endothelial phenotypes evoked by arterial waveforms derived from atherosclerosis-susceptible and -resistant regions of human vasculature. Proc Natl Acad Sci U S A 101: 14871-14876.

49. Buschmann I, Pries A, Styp-Rekowska B, Hillmeister P, Loufrani L, et al. (2010) Pulsatile shear and Gja5 modulate arterial identity and remodeling events during flow-driven arteriogenesis. Development 137: 2187-2196.
50. Srinivasan VJ, Atochin DN, Radhakrishnan H, Jiang JY, Ruvinskaya S, et al. (2011) Optical coherence tomography for the quantitative study of cerebrovascular physiology. J Cereb Blood Flow Metab 31: 1339-1345.
51. Santisakultarm TP, Schaffer CB (2011) Optically quantified cerebral blood flow. J Cereb Blood Flow Metab 31: 1337-1338.
52. Duemani Reddy G, Kelleher K, Fink R, Saggau P (2008) Three-dimensional random access multiphoton microscopy for functional imaging of neuronal activity. Nat Neurosci 11: 713-720.

Supplemental Material

Detailed Methods

Microscope and Imaging

We constructed a TPLS microscope to acquire *in vivo* images and line-scan data (Figure S1). We generated 100 fs pulses at 80 MHz with a Titanium:Sapphire laser oscillator (Mai Tai HP; Newport Spectra-Physics) that was pumped by a continuous wave diode laser (Millenia; Newport Spectra-Physics) and passed through a dispersion compensator (DeepSee; Newport Spectra-Physics). Intensity was controlled by rotating a $\lambda/2$ wave-plate relative to a polarizing splitter and utilizing the transmitted beam. The laser was then routed onto a microscope platform based on a previous design [1] that was optimized for deep tissue imaging and blood velocity measurements. The laser pulses were raster-scanned by galvanometric mirrors (Cambridge Technology) and relay-imaged to the back aperture of a 1.0 numerical aperture, 20x water-immersion objective (Zeiss). Fluorescence was collected by the same objective, reflected by a primary dichroic mirror (700 nm long-pass; Chroma), split into red and green channels with a secondary dichroic mirror (560 nm long-pass; Chroma), spectrally cleaned with additional band-pass filters (Chroma), and relayed to photomultiplier tubes (PMT; H7422P-40MOD; Hamamatsu). The PMT signal was amplified (10^5 transimpendence gain), low-pass filtered (4 pole Bessel at f_c = 300 kHz), and digitized. The anesthetized mouse's head was immobilized with a stereotax and placed on a three-dimensional translation stage (11SI70521 Rev. 01; Newport) that allowed precise positioning of the brain relative to the imaging focus. MPScope 1.0 software was used to control the microscope and to acquire image and line-scan data [2].

LS-PIV in Detail

The blood plasma was loaded with fluorescent dye that allowed clear imaging of perfused vessels. RBCs did not take up dye and could be resolved as dark particles amid the bright background using TPLSM (Figure S2A). Line-scans were positioned along the central axis of vessels and captured at a rate of 2.6 kHz. This central location corresponded to the path of maximum axial velocity, allowing multiple RBCs to contribute collectively to analysis per time point. The line-scan data was cropped to an ROI within the measured vessel, from which LS-PIV determined displacement of RBCs between sequential line-scans using cross-correlation in Fourier space. Importantly, displacement can be determined by this method when RBCs move too quickly to form continuous streaks within the space-time data (Figure S2B). Velocity is calculated as $v = \Delta x / \Delta t$, where Δt is the time between line-scans and also determines the temporal resolution of analysis.

Let us consider a single RBC captured by a line-scan. We can approximate its image point spread function as a Gaussian $h(\mathrm{x},\sigma)$ with center x and standard deviation σ. The line-scan image can then be written as a convolution of the point spread function with the RBC density made of delta functions:

$$s_1(x) = \rho(x) * h(x,\sigma), \quad \rho(x) = \sum_{1}^{N} \delta(x - x_n)$$

where x is the instantaneous location of the active area of the line-scan, $\rho(\mathrm{x})$ is the RBC density, and x_n is the location of a RBC. If we take a second line-scan quickly after the first, we can write the signal from that second scan as:

$$s_2(x) = \rho(x) * \delta(x + \Delta x) * h(x,\sigma)$$

where Δx is the distance moved by the RBCs in the time, Δt , between the two scans. For the ideal case, the cross-correlation of the two images results in:

$$\begin{aligned} g(x) &= s_1(x) \otimes s_2(x) \\ &= N \cdot h(x,\sigma\sqrt{2}) \otimes \delta(x + \Delta x) \end{aligned}$$

This tells us that the cross-correlation of the two images, in which the second image is a shifted version of the first, will yield a Gaussian distribution centered at shift distance, Δx. Further, this result shows us that the signal-to-noise ratio increases with the number of particles in the field of view. The velocity along the line-scan is then the center peak of the cross-correlation divided by the time between the two images:

$$v = \Delta x / \Delta t$$

In practice, there are a number of techniques beyond simple cross-correlation that we use to optimize analysis. First, we remove background (such as from non-moving tissue) by subtracting the average time-invariant signal from the line-scan data. Analysis of the Fourier transform has demonstrated that phase information, not amplitude, is more important in describing an object's position [3]. We therefore employ a filtering technique in the Fourier domain consisting of symmetric phase-weighted filtering, which reduces side-lobes that frequently appear in the cross-correlation [4]. We then convert back to the spatial domain where we average across a number of cross-correlation frames to increase the SNR. To arrive at a maximum accurate velocity, we fit a Gaussian distribution to the cross-correlation. All analyses were executed in 32-bit Matlab (Mathworks).

Supplemental References

1. Nishimura N, Rosidi NL, Iadecola C, Schaffer CB (2010) Limitations of collateral flow after occlusion of a single cortical penetrating arteriole. J Cereb Blood Flow Metab 30: 1914-1927.
2. Nguyen QT, Tsai PS, Kleinfeld D (2006) MPScope: a versatile software suite for multiphoton microscopy. J Neurosci Methods 156: 351-359.
3. Oppenheim AV, Lim JS (1981) The importance of phase in signals. Proc IEEE 529-541.
4. Wernet MP (2005) Symmetric phase only filtering: a new paradigm for DPIV data processing. Meas Sci Technol 16: 601-618.

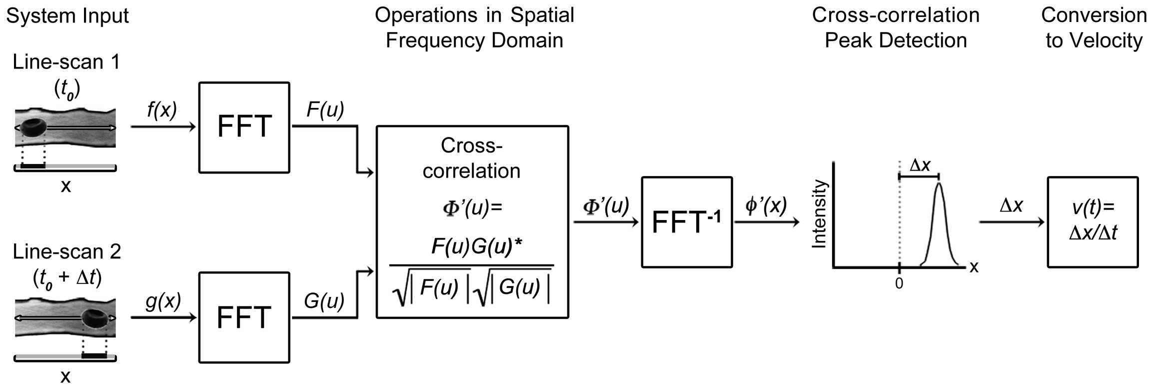

Figure 1. Illustration of generalized LS-PIV. RBCs appear dark amid fluorescently labeled plasma. Two successive line-scans are recorded along the central axis of the vessel, capturing the displacement of an RBC across time interval Δt . The line-scans are Fourier-transformed, cross-correlated with a symmetric phase-weighted filtering operation, and inverse Fourier-transformed. A peak detection operation is performed to locate the correlation peak corresponding to the RBC displacement, which is converted to velocity by dividing by the time interval between the scans.

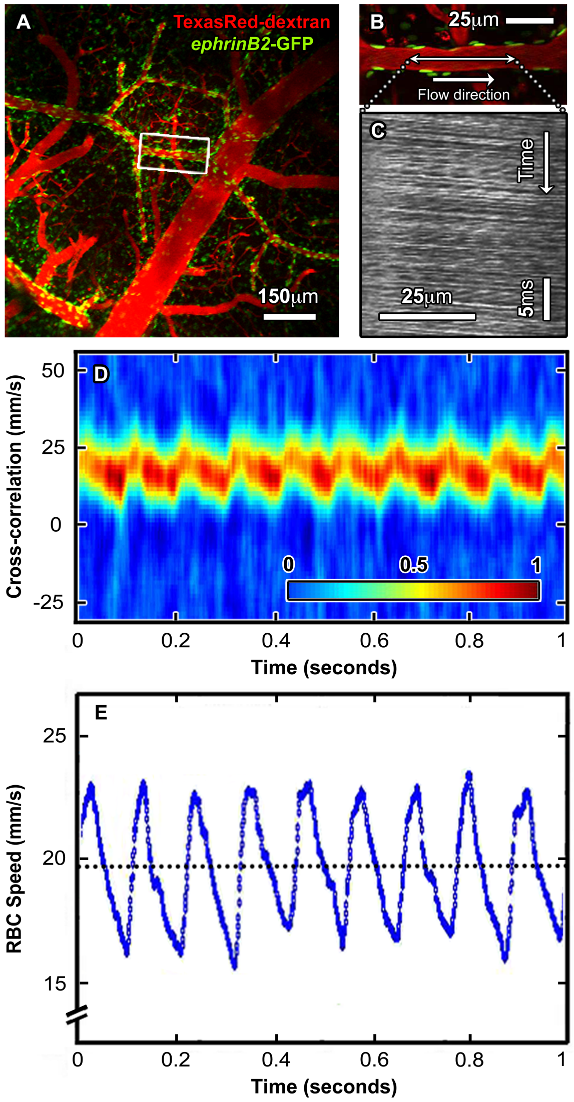

Figure 2. LS-PIV analysis of *in vivo* two-photon line-scan data measured in cortical artery. **A**, TPLSM projection of cortical vasculature in *ephrin-B2*$^{+/H2B\text{-}eGFP}$ mouse with the blood plasma labeled by intravenous injection of Texas Red-dextran. *Ephrin-B2*$^{+/H2B\text{-}eGFP}$ mice express nuclear GFP in arterial endothelial cells, which allows these vessels to be distinguished with cellular resolution. **B**, TPLSM image through the center of an arteriole from the white box in (A). The double-headed arrow indicates the location where line-scans were recorded and the single-headed arrow represents the direction of flow. **C**, Line-scan data from the vessel in (B) where each sequential line-scan appears beneath the one before, forming a space-time image with time increasing from top to bottom. Each dark streak corresponds to a single RBC as it moves along the scan path. **D,** LS-PIV applied between pairs of sequential line-scans from vessel (C). Individual cross-correlation results are oriented along the y-axis with time advancing left to right. Each respective probability distribution is normalized and color-coded according to the inset key. The y-axis is converted from units of distance to units of speed by dividing by the time interval between line-scans. **E,** The final RBC velocity along the scan line is determined from the peak value at each time point in (D). The dotted line represents time-averaged velocity. The temporal resolution of analysis is shown here at 1.3 kHz (1/2 of maximum) to better illustrate individual points.

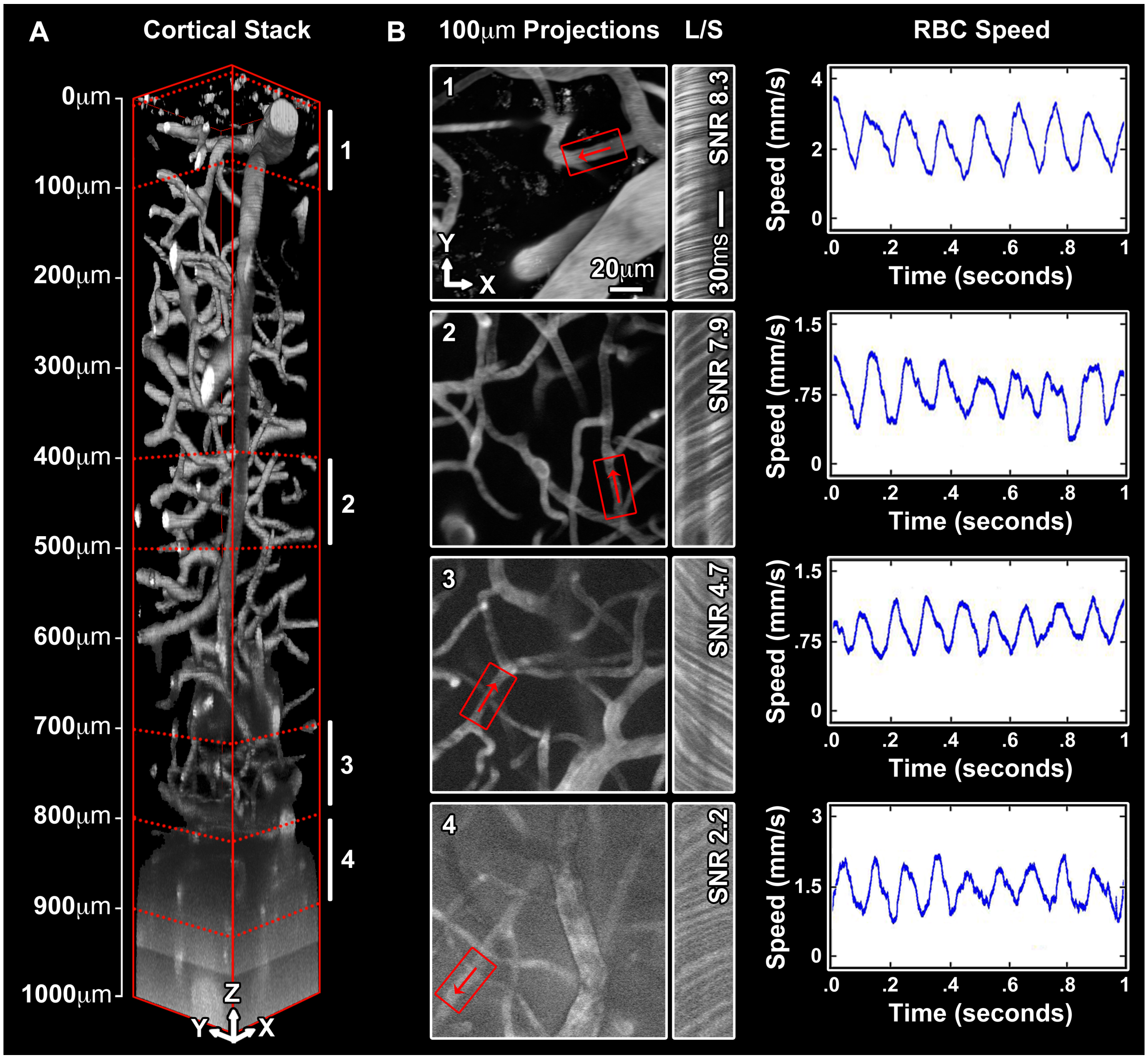

Figure 3. Effects of depth-dependent noise on LS-PIV analysis. A, Three-dimensional rendering of cortical vessels imaged with TPLSM demonstrating depth-dependent decrease in signal-to-noise ratio (SNR). The blood plasma was labeled with Texas Red-dextran and a 1000 μm stack was acquired with images at 1 μm spacing along the z-axis starting from the brain surface. **B,** 100 μm-thick projections of regions 1-4 in panel (A). RBC velocities were measured along the central axis of vessels shown in red boxes, with red arrows representing orientation of flow. The raw line-scan data (L/S) are depicted to the right of each field and labeled with their respective SNR. Corresponding LS-PIV analyses are depicted to the far right.

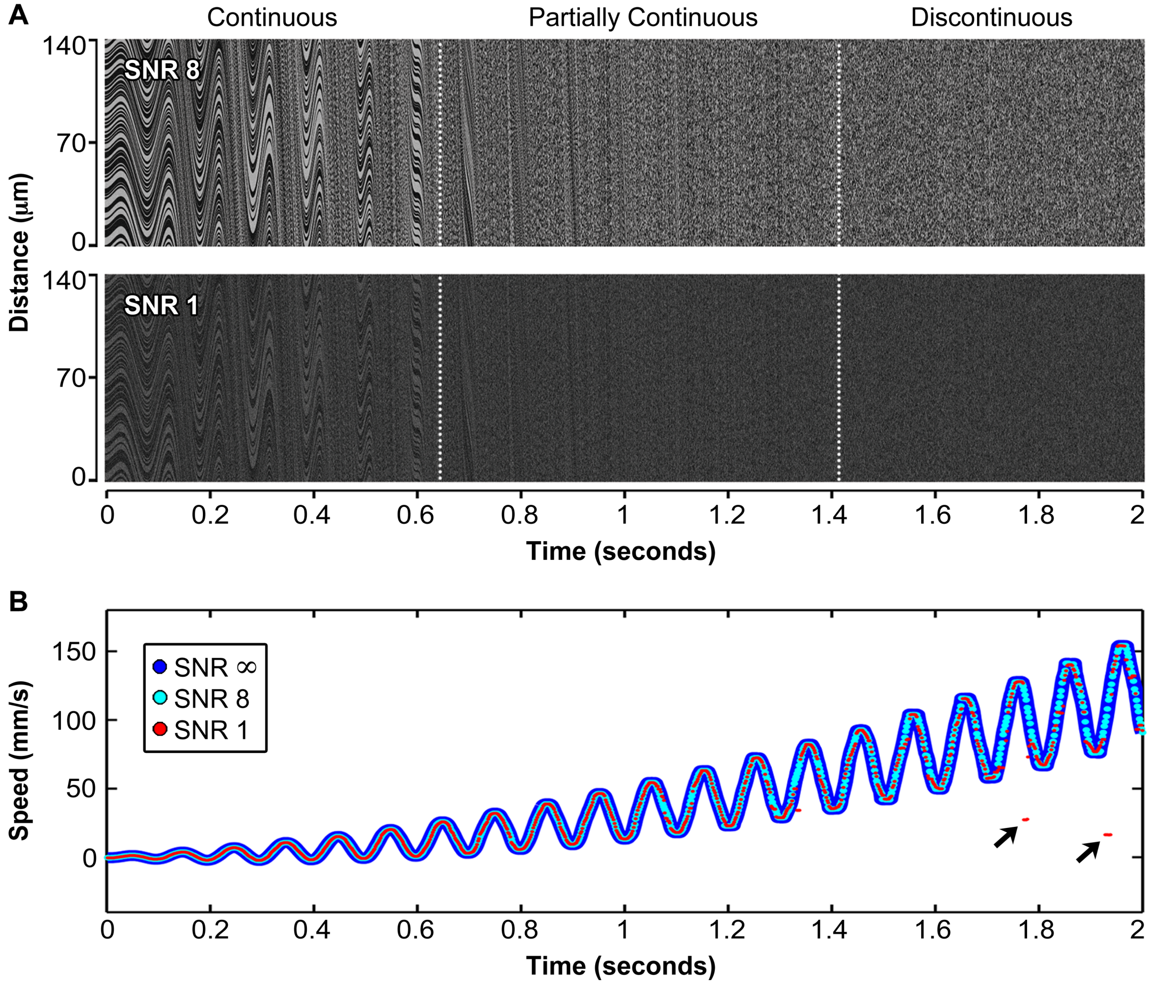

Figure 4. Accuracy of LS-PIV analysis with noise and increasing speed. A, *Top,* simulation line-scan data with a low level of normally distributed noise with SNR of 8, typical of good *in vivo* data. *Bottom,* simulation line-scan data with a high level of normally distributed noise with SNR of 1, representing poor data. These data were generated using a randomized distribution of particles that was shifted in known spatial increments over time. The size of each particle was further randomized between 1 to 7 μm to mimic RBCs at different orientations and positions relative to the scan line. Speed was increased over time and oscillated at 10 Hz to simulate mouse heart rate. Particles initially appear as continuous dark lines within the time-space data, and become discontinuous at higher speed. For comparison, these data are displayed with time along the x-axis aligned with their velocity analyses in (B). **B,** LS-PIV analysis of line-scan data from panel (A). Actual particle speed is represented by a dark blue line (SNR of infinity) with increased thickness to aid in visualization of overlapping points. Analyses of data with an SNR of 8 or 1 are displayed as light blue dots or red dots, respectively. Arrows indicate distinct outliers from analysis of high velocity data with an SNR of 1, which could be removed using median filters.

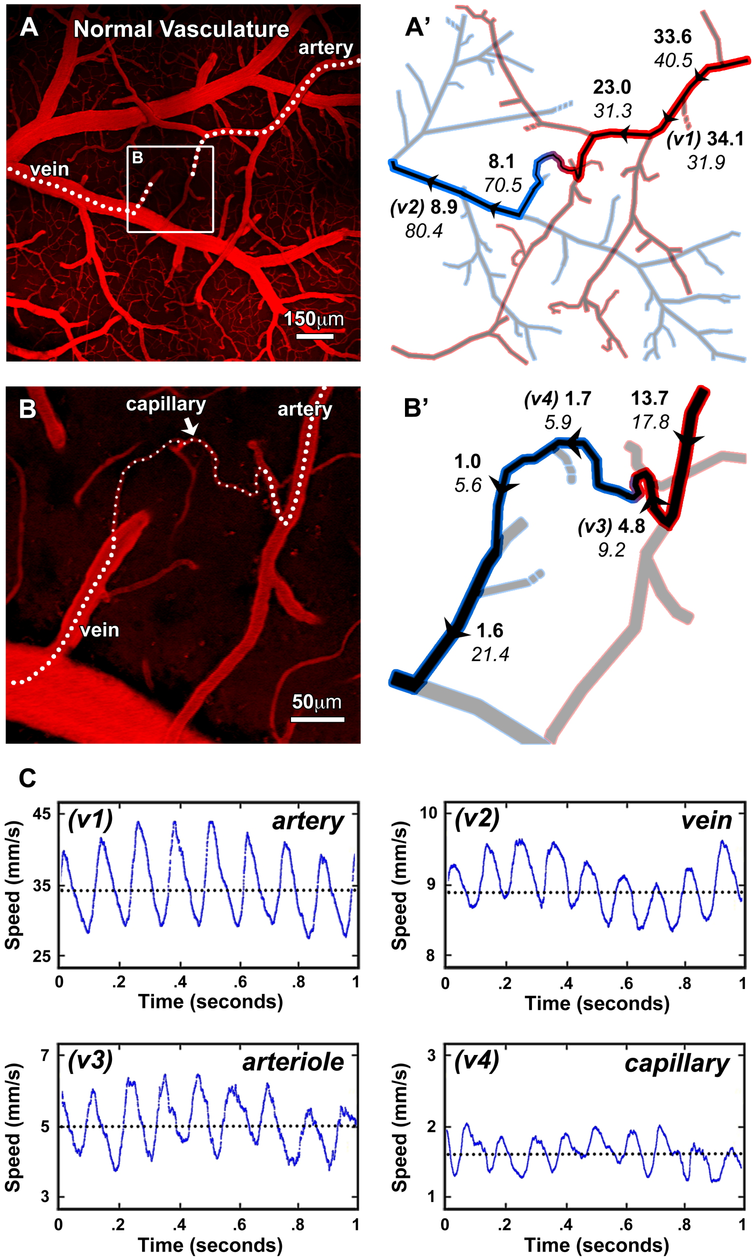

Figure 5. RBC velocities along the normal vessel network in mouse cortex. A, Low-magnification TPLSM image of cortical vasculature in control mouse with the blood plasma labeled by Texas Red-dextran. **A',** Diagram of the vascular network from image (A) with arteries shown in red and veins in blue. An artery-to-vein pathway is highlighted and labeled with arrowheads to indicate the direction of flow and specific locations of velocity and diameter measurements. Bold numbers represent average center-axis velocity in units of mm/s and italic numbers represent diameter in units of μm corresponding to the adjacent arrowheads. **B,** High magnification TPLSM image from the white box in (A) demonstrating an artery, vein, and interconnecting capillary. **B',** Diagram of the vascular network from image (B). **C,** Representative analyses in a subset of vessels (v1-v4) from panels (A') and (B').

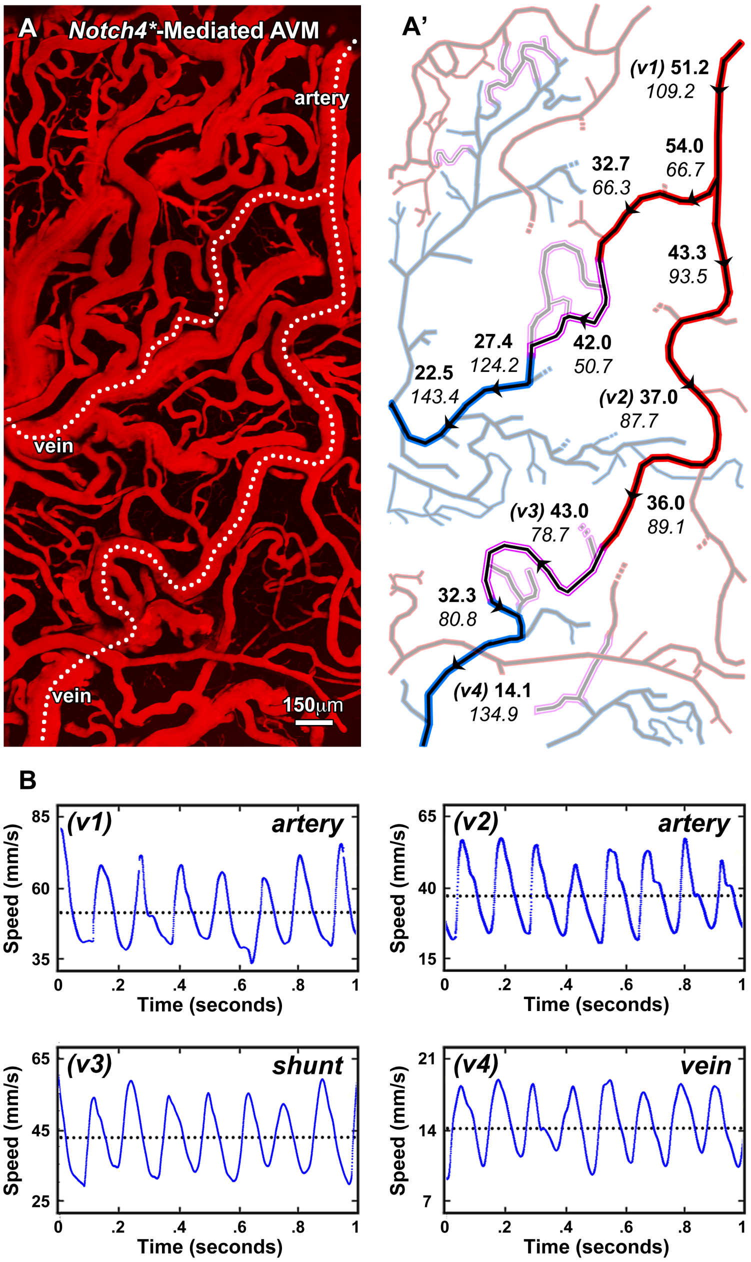

Figure 6. RBC velocities along the vessel network of brain AVMs in mice. A, Low-magnification TPLSM image of cortical vasculature in Notch4* mouse model with the blood plasma labeled by Texas Red-dextran. **A',** Diagram of the vascular network from image (A) with arteries shown in red, veins in blue, and shunts in purple. Artery-to-vein pathways are highlighted and labeled with arrowheads to indicate the direction of flow and specific locations of velocity and diameter measurements. Bold numbers represent average center-axis velocity in units of mm/s and italic numbers represent diameter in units of μm corresponding to the adjacent arrowheads. **B,** Representative analyses in a subset of vessels (v1-v4) from panels (A').

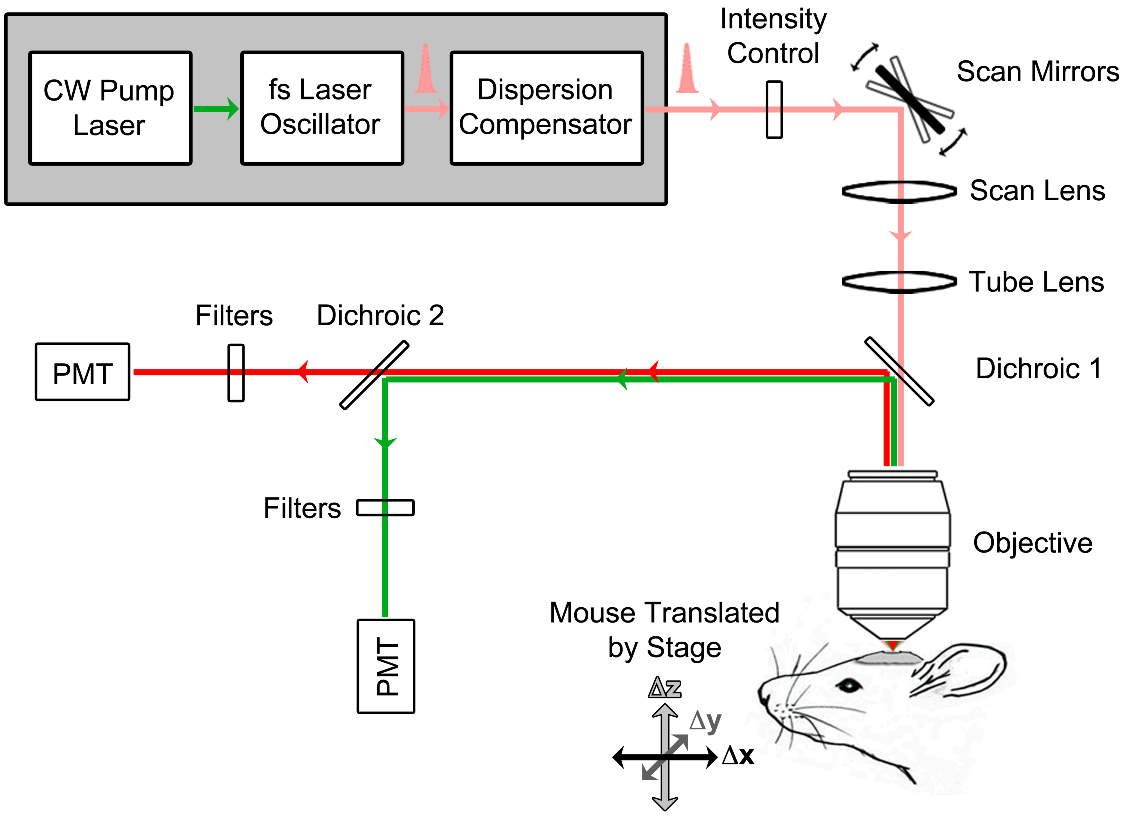

Supplemental Figure 1. Schematic of the two-photon laser scanning microscope. Images and line-scan data were obtained using a locally constructed TPLSM. 100 fs, 80 MHz pulses were generated by a Titanium:Sapphire laser oscillator (Mai Tai HP; Newport Spectra-Physics) and passed through a dispersion compensator (DeepSee; Newport Spectra-Physics). Laser intensity was controlled by rotating a $\lambda/2$ wave-plate relative to a polarizing splitter, and the attenuated beam was directed onto the microscope platform. The laser pulses were raster-scanned by galvonometric mirrors and relay-imaged to the back aperture of a 1.0 NA water-immersion objective (Zeiss). Two-photon excited fluorescence was collected by the same objective, reflected by a dichroic mirror (700 nm long pass, dichroic 1), split into red or green channels by a second dichroic mirror (560 nm long pass, dichroic 2), spectrally cleaned with additional band-pass filters (Chroma), and relayed to photomultiplier tubes (PMT; H7422P-40MOD; Hammamatsu). The anesthetized mouse was immobilized with a stereotax (myNeurolab.com) and placed on a three-dimensional translation stage (11SI70521 Rev. 01; Newport) that allowed precise positioning of the mouse relative to the focus of the microscope. MPScan 1.0 software was used to control the microscope and record image data.

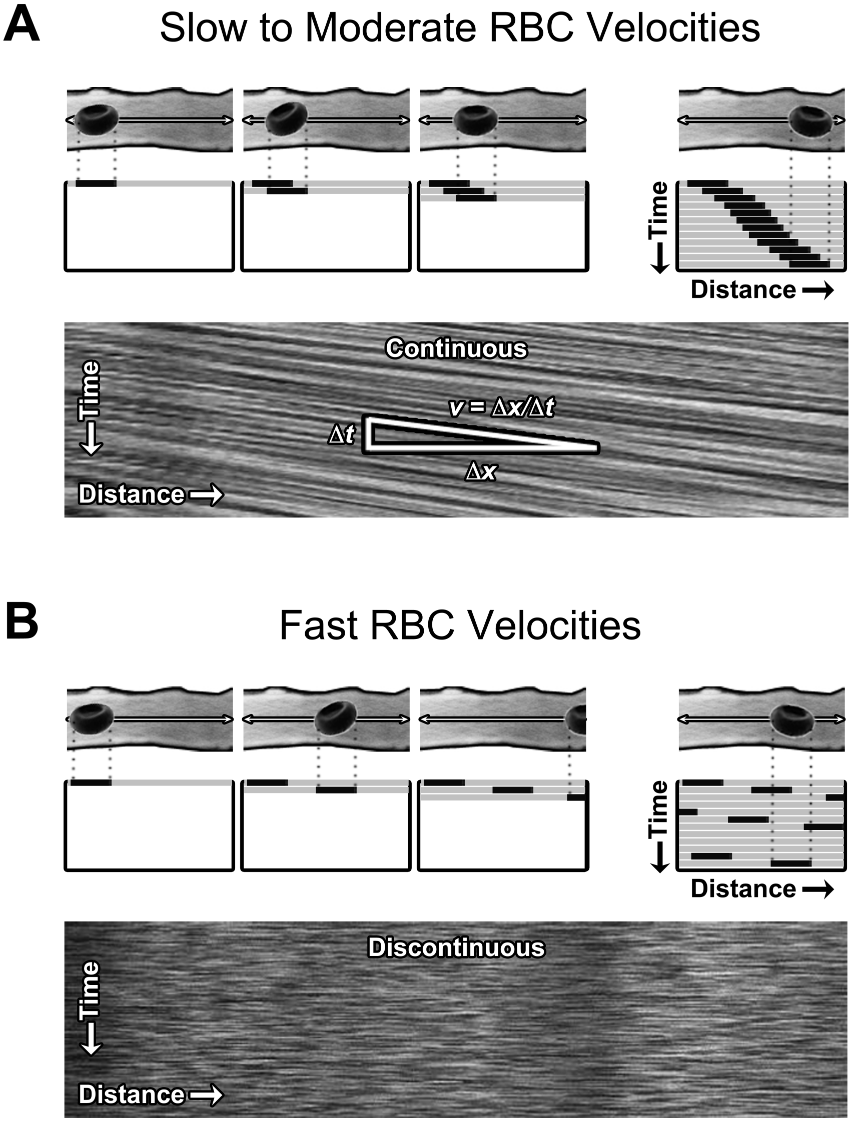

Supplemental Figure 2. Loss of RBC continuity in space-time data when high velocities are measured with line-scans. **A,** *Top,* schematic of line-scan data of slow to moderate RBC velocities. Each sequential line-scan appears beneath the previous one, with time advancing from top to bottom. RBCs appear as continuous diagonal streaks in the space-time image when RBC velocities are relatively slow compared to the line-scan rate. *Bottom,* space-time image of *in vivo* line-scan data where RBCs appear as continuous dark streaks. Previous analytical methods have determined velocities by calculating the inverse slope of the streaks. **B,** *Top,* schematic of line-scan data of fast RBC velocities. RBCs may appear as discontinuous streaks or as just a few dark spots in the space-time image. The large number of RBCs confounds identification of individual streaks. *Bottom,* space-time image of *in vivo* line-scan data where RBCs velocity is high relative to the line-scan rate.

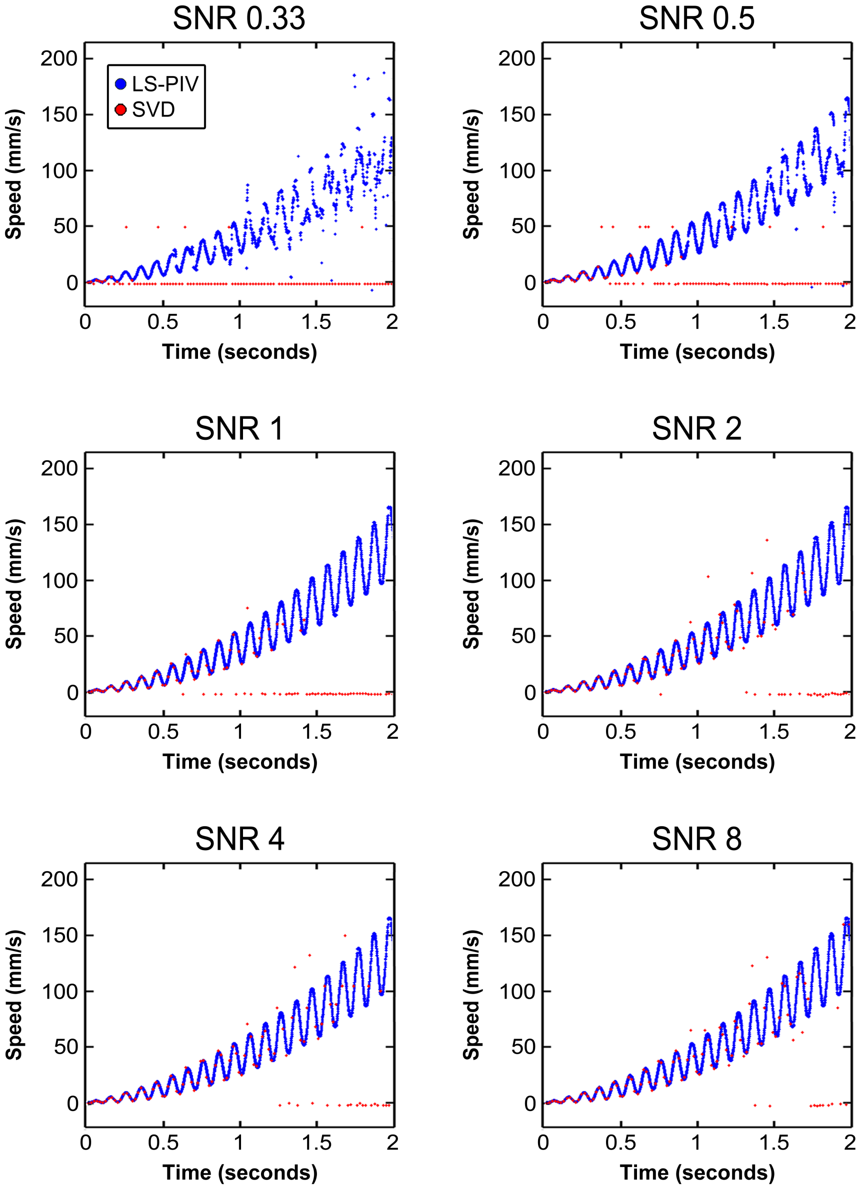

Supplemental Figure 3. Effects of noise on performance of LS-PIV and SVD. Analyses of simulation line-scan data using LS-PIV and previously published singular valued decomposition (SVD). Data had increasing velocity and SNRs ranging from 0.33 to 8. Blue and red dots correspond to LS-PIV and SVD analysis, respectively. Analysis parameters were matched between LS-PIV and SVD using a 100 μm-long region of interest and the same processing time. Agreement between these methods was best at lower velocities and diverged with increasing speed.

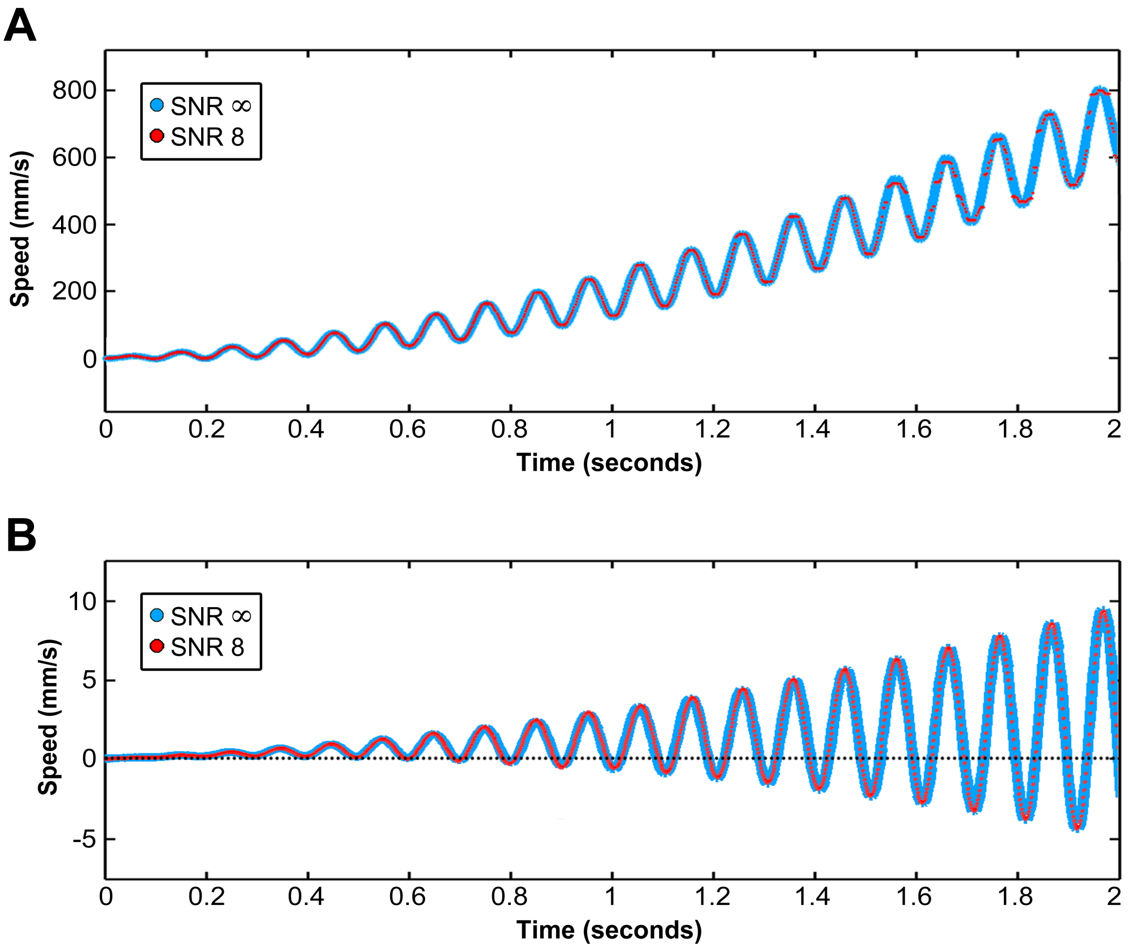

Supplemental Figure 4. Performance of LS-PIV with high velocities and flow reversal.
A, LS-PIV analysis of simulation line-scan data with velocity increasing to 800 mm/s. Actual particle velocity is represented by the blue line (SNR of infinity). Analysis was performed on data with an SNR of 8, within a 426 μm-long region of interest, and displayed as red dots. **B,** LS-PIV analysis on simulation line-scan data with increasing velocity and reversal of flow. Actual particle velocity is represented by the blue line (SNR of infinity). Analysis was performed on data with an SNR of 8 and displayed as red dots.

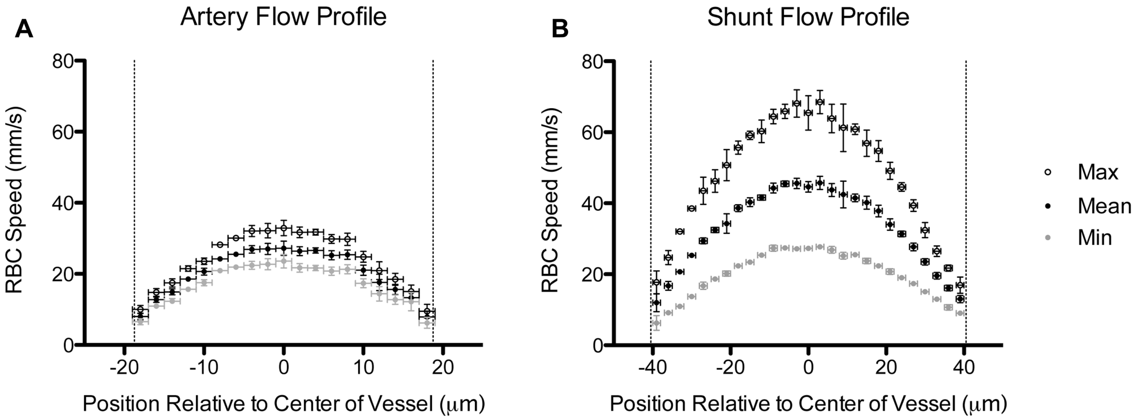

Supplemental Figure 5. Cross-sectional flow profiles in control artery and AV shunt. **A**, RBC speed as a function of transverse position in a control artery. **B,** RBC speed as a function of transverse position in an AV shunt. Maximum, mean, and minimum RBC speeds were calculated from pulsatile velocities across 5 second scans. Five separate datasets were analyzed at each position in the vessel to determine the final velocities and their standard deviations (vertical error bars). Measurements were acquired serially along the vessel diameter over the span of ~15 minutes. Vertical dotted lines represent the position of the vessel walls. Interestingly, measured RBC velocities did not go to zero at the wall, likely because of the cells' finite size and inability to move closer to the boundary than half their width. Positional error was estimated additively from the optical resolution, translation stage jitter, and motion artifact of the animals (horizontal error bars).

IV

Notch4 Normalization Reduces Blood Vessel Size in Arteriovenous Malformations

Chapter 4 is a reprint of material as it appears in Patrick A. Murphy, Tyson N. Kim, Gloria Lu, Andrew W. Bollen, Chris B. Schaffer, and Rong A. Wang, "*Notch4* Normalization Reduces Blood Vessel Size in Arteriovenous Malformations", Science Translational Medicine 4, 117 (2012). Dr. Patrick Murphy is the principal author of this work and wrote the manuscript, which is also his thesis work. The dissertation writer is a second author with equal contribution, who contributed to tools and technology, performing experiments, and analyzing the data. Reprinted with permission from AAAS.

VASCULAR DISEASE

Notch4 Normalization Reduces Blood Vessel Size in Arteriovenous Malformations

**Patrick A. Murphy,[1]*† Tyson N. Kim,[1]* Gloria Lu,[1] Andrew W. Bollen,[2]
Chris B. Schaffer,[3] Rong A. Wang[1]‡**

Abnormally enlarged blood vessels underlie many life-threatening disorders including arteriovenous (AV) malformations (AVMs). The core defect in AVMs is high-flow AV shunts, which connect arteries directly to veins, "stealing" blood from capillaries. Here, we studied mouse brain AV shunts caused by up-regulation of Notch signaling in endothelial cells (ECs) through transgenic expression of constitutively active *Notch4* (*Notch4). Using four-dimensional two-photon imaging through a cranial window, we found that normalizing Notch signaling by repressing *Notch4** expression converted large-caliber, high-flow AV shunts to capillary-like vessels. The structural regression of the high-flow AV shunts returned blood to capillaries, thus reversing tissue hypoxia. This regression was initiated by vessel narrowing without the loss of ECs and required restoration of EphB4 receptor expression by venous ECs. Normalization of Notch signaling resulting in regression of high-flow AV shunts, and a return to normal blood flow suggests that targeting the Notch pathway may be useful therapeutically for treating diseases such as AVMs.**

INTRODUCTION

Abnormally enlarged high-flow blood vessels often continue to expand, leading to life-threatening ruptures. These dangerous vascular lesions underlie the pathology of a wide range of "high-flow" vascular diseases such as arteriovenous (AV) malformations (AVMs), hereditary hemorrhagic telangiectasia, and aneurysms (*1*). The hemodynamic stress exerted on the vasculature by these high-flow lesions can cause hemorrhagic rupture (*1*, *2*). The ability to safely and noninvasively constrict the high-flow large vessels by molecular intervention holds promise to treat these life-threatening conditions for which there are currently limited effective treatments.

Normally, arteries carry blood from the heart to the capillaries through a series of vessels with a successive reduction in caliber to reduce blood flow. Capillaries, where exchange of nutrients and wastes occurs, are the smallest diameter vessels with the lowest blood flow. Postcapillary venules join sequentially wider veins to return blood back to the heart. This AV interface is critical for proper tissue perfusion. High-flow AV shunts are direct connections of arteries to veins, displacing the perfusing capillaries, thus creating positive feedback between increased vessel diameter and accelerated blood flow, and often resulting in vessel rupture. High-flow AV shunts are the fundamental defect in AVMs, causing both tissue ischemia and hemorrhage.

Notch receptors are transmembrane proteins that promote arterial at the expense of venous endothelial cell (EC) specification by enhancing expression of arterial molecular markers, such as *ephrin-B2*, and suppressing the expression of venous markers, such as *EphB4* (*3*). The transmembrane signaling molecule *ephrin-B2* was the first gene found to be expressed by the ECs of arteries but not veins, and is a key marker of arterial ECs (*4*). Its cognate tyrosine kinase receptor, *EphB4*, was the first venous endothelial marker identified (*4*). COUP-TFII, a member of the orphan nuclear receptor superfamily expressed by venous but not arterial ECs, acts upstream of Notch and actively promotes venous EC specification by repressing the expression of Notch (*5*). These AV-distinctive genes are crucial in the morphogenesis of the embryonic vasculature, and their differential expression patterns in arterial and venous vessels persist in adult vascular endothelium (*6*, *7*), suggesting that postnatal retention of AV specification may have a role in maintaining vascular structure and function. Supporting this notion, we and others have reported that Notch activity in the endothelium is aberrantly increased in patients with brain AVMs (*8*, *9*). This suggests that aberrant Notch signaling may be a molecular defect underlying AVMs and that targeting Notch signaling may be a new therapeutic strategy for the treatment of high-flow vascular diseases such as AVMs.

Here, we use a mouse model of Notch-mediated AVMs (*10*) and two-photon excited fluorescence imaging (*11*) to obtain four-dimensional (4D) vascular topology and blood velocity data from the mouse brain vasculature. We demonstrate that high-flow AV shunts can be shrunk to capillary-like vessels after normalization of Notch signaling through an EphB4-dependent mechanism that does not require the loss of ECs.

RESULTS

Repression of *Notch4** causes the specific regression of high-flow AV shunts

In our *Notch4*-Tet* (*Tie2-tTA;TRE-Notch4**) mouse model of AVM, Notch4*, a truncated Notch4 lacking the extracellular domain and thus constitutively active, is expressed specifically in ECs using a temporally regulatable tetracycline-repressible system (*12*). *Notch4** is under the control of the tetracycline-responsive element (*TRE*) and is only activated by the tetracycline transactivator (tTA) driven by the *Tie2* promoter expressed in ECs. Treatment with doxycycline, a tetracycline derivative, led to rapid repression of Notch4* expression to baseline

---

[1] Laboratory for Accelerated Vascular Research, Division of Vascular Surgery, Department of Surgery, University of California, San Francisco, San Francisco, CA 94143, USA . [2] Department of Pathology, University of California, San Francisco, San Francisco, CA 94143, USA. [3] Department of Biomedical Engineering, Cornell University, Ithaca, NY 14853, USA.

*These authors contributed equally to this work.

†Present address: Koch Institute for Integrative Cancer Research, Massachusetts Institute of Technology, Cambridge, MA 02139, USA.

‡To whom correspondence should be addressed. E-mail: rong.wang@ucsfmedctr.org

levels by 24 hours (fig. S1). Because *Notch4** was rapidly repressed by doxycycline, henceforth, we refer to doxycycline-mediated Notch4* repression simply as *Notch4** repression. *Notch4** expression leads to high-flow AV shunts in the brains of these mice (*10*). To directly test whether these high-flow AV shunts can be normalized after the repression of *Notch4**, we combined two-photon microscopy with a cranial window placed over the right parietal cortex of the mouse brain (fig. S2) to visualize vascular topology and hemodynamics over time.

To avoid the potential confounding effects of hemorrhage and illness in severely affected *Tie2-tTA;TRE-Notch4** mice, we focused on high-flow AV shunts in the mice about postnatal day 12 (P12), when most of the animals had just developed abnormal AV shunts. The minimum diameter of these AV shunts at P11 to P13 averaged 22.2 μm ± SD 7.3, ranging from 8.1 to 51.3 μm (n = 46 shunts in 13 mice), about 2 to 10 times the diameter of the capillaries in age-matched controls, which averaged 4 μm ± SD 0.5, ranging from 2.7 to 5.0 μm (n = 9 capillaries in 3 mice, $P < 0.000002$; Fig. 1, A to D). Centerline flow velocity through AV shunts was much higher than in control capillaries, averaging 37.7 mm/s ± SD 14.4 (n = 11 shunts in 11 mice), compared to 2.1 mm/s ± SD 1.0 in control capillaries (n = 9 capillaries in 3 mice, $P < 0.0000008$; Fig. 1, A to D), and as reported (*13*).

We then analyzed the vessel diameter and blood flow in AV shunts before and after *Notch4** repression. We found that both the diameter and the flow were significantly decreased within 48 hours of Notch4* repression (Fig. 1, E to M) relative to that in untreated mutant animals (fig. S3). The diameter changed primarily in the AV shunt and distal vein; adjacent arterial vessels were less affected (Fig. 1, E to L). To determine whether advanced AVMs also regressed upon Notch4* repression, we examined severely affected, ataxic mice at a later time point (P22) and found that the mature AVMs also regressed (fig. S4).

Not all AV shunts enlarge with continued *Notch4** expression, a variability likely caused by systemic or regional hemodynamic changes. Therefore, we sought to identify a subset of "growth-prone" AV shunts to further test the effects of Notch4* repression. We found that among a growth-prone population of AV shunts, defined by continued growth over several days, all were induced to regress by *Notch4** repression (ten AV shunts in eight mice, fig. S5). In contrast, with continued *Notch4** expression, all of this population continued to grow (five AV shunts in two mice, fig. S5). Supporting these data, we also show similar findings in a separate experiment using mice with a mixed genetic background (fig. S8B).

When imaging for >1 week was possible, we observed the complete regression of the AV shunt such that the AV shunts returned to microvessels resembling capillaries (fig. S6), a finding also confirmed by ex vivo analysis (fig. S6). Structurally, this regression involved the normalization of smooth muscle cell coverage; that is, the wrapping of smooth muscle cells around vessels, typical of arteries, was restored after Notch4* repression (fig. S7). Time point analysis of vessel narrowing indicated that the onset of diameter and velocity reductions occurred within 12 to 24 hours of *Notch4** repression (fig. S8). These data suggest that Notch4* repression results in the prompt narrowing of high-flow AV shunts.

*Notch4** repression directly induces narrowing of AV shunts

Given that reductions in blood flow are known to cause vessel regression (*14*), we asked whether *Notch4** repression leads to shunt regression directly or indirectly through the reduction of AV shunt flow. To discriminate between these possibilities, we measured blood flow in the upstream feeding artery, the AV shunt, and an adjacent artery.

If *Notch4** repression directly reduces the diameter of the AV shunt, we would expect increased resistance and decreased flow through the AV shunt (Fig. 2A). Consequently, the total flow through the feeding artery would also be reduced. Furthermore, the AV shunt blood flow would redistribute to adjacent arteries, thus increasing blood flow in adjacent arteries. Our empirical measurements matched these predictions; total blood flow was reduced, but flow through an adjacent artery to the AV shunt was increased (Fig. 2, B to D).

It is possible that regression of the AV shunt might also be caused indirectly by the effects of reduced flow in the AV shunt after *Notch4** repression (Fig. 2A). Two possible scenarios might lead to reduced flow in the AV shunt. In one, resistance in the adjacent artery is reduced, "stealing" blood flow from the AV shunt. However, in this scenario, total systemic resistance to flow should also be reduced, and thus, combined flow through the AV shunt and the adjacent artery should be increased, which we did not observe. In a second scenario, systemic flow is reduced by events either upstream or downstream of the AV shunt and adjacent artery. However, in this scenario, flow through both the AV shunt and the adjacent artery should be reduced, which we also did not observe. These data suggest that there is a direct mechanism for AV shunt regression after *Notch4** repression.

The mechanism for vessel regression does not require the loss of ECs

To understand the cellular mechanism of AV shunt regression, we asked whether reduction in the total number of ECs or the area covered by individual ECs could be involved. To this end, we used the *ephrin-B2–H2B–eGFP* mouse line to provide nuclear labeling of ECs within the AV shunt (*10*). In the presence of *Notch4**, ECs in the AV shunt, regardless of arterial or venous origin, expressed *ephrin-B2–H2B–eGFP*. The H2B-eGFP (enhanced green fluorescent protein) fusion protein is extremely stable and can persist for months (*15*). Thus, within the AV shunt, in the short time frame of examination, *ephrin-B2–H2B–eGFP* serves as a general EC marker without arterial specificity.

We performed 4D imaging of AV shunt diameters and cell numbers in 23 AV shunts in seven *Tie2-tTA;TRE-Notch4*;ephrin-B2–H2B–eGFP* mice, at time points up to 48 hours after Notch4* repression. Figure 3A shows such an example: AV shunt regression was detected between 20 and 28 hours, but the cell count was not reduced in the regressing AV shunts at 28 hours or even at 36 hours after further vessel regression. Another example is provided in fig. S9. More analysis at 0 and 24 or 28 hours after Notch4* repression showed that all shunts regressed by 40% ± SD 14% by 24 or 28 hours. The onset of AV shunt regression was variable, sometimes occurring as early as 12 hours after Notch4* repression. About 70% (18 of 23) of these AV shunts regressed without detectable loss of cells at 24 or 28 hours, judged by counting the $eGFP^+$ nuclei. These results suggest that AV shunt regression did not depend on the loss of vascular cells. We confirmed that this was the case with an alternative method of tracking EC nuclei using our *Tie2-tTA* induction system in conjunction with a *TRE-H2B-eGFP* reporter. We first verified that this reporter was a specific and robust marker of EC nuclei; analysis of cell labeling in the sections revealed that 91.4% ± SEM 3.4% of 4′,6-diamidino-2-phenylindole–positive ($DAPI^+$) ECs but none of the adjacent mural cells were GFP^+ (fig. S10). We then analyzed vessel diameter and EC number up to 36 hours after Notch4* repression. By 12 hours, we detected vessel regression in 36 of 38 AV shunts

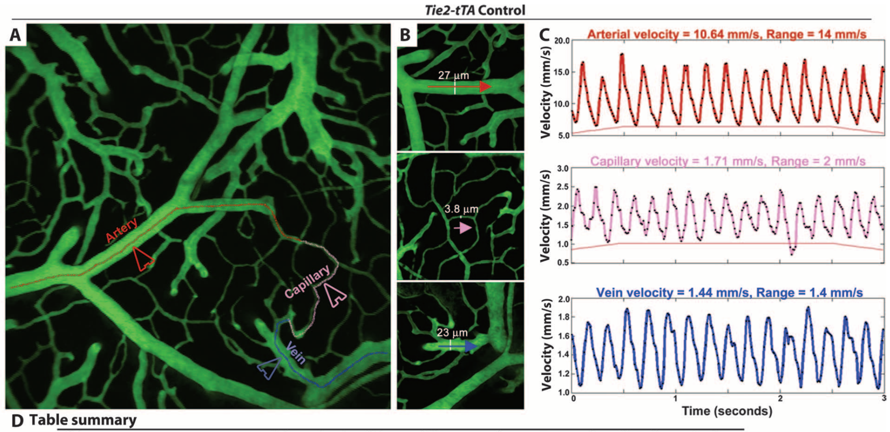

D Table summary

Diameter	Mean (µm) ± SD	AV connections measured	Number of mice
*Tie2-tTA; TRE-Notch4**	22.2 ± 7.3	46	13
Tie2-tTA	4 ± 0.5	9	3

Centerline blood velocity	Mean (mm/s) ± SD	AV connections measured	Number of mice
*Tie2-tTA; TRE-Notch4**	37.7 ± 14.4	11	11
Tie2-tTA	2.1 ± 1	9	3

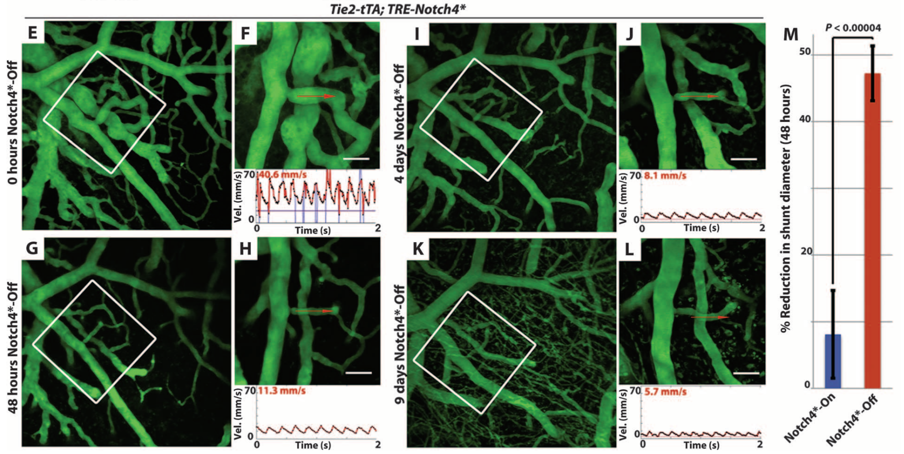

Fig. 1. Repression of *Notch4** induces the normalization of AVMs. (**A** to **C**) Two-photon time-lapse imaging of cortical brain vessels through a cranial window in wild-type mice. Plasma was labeled by intravenous injection of FITC-dextran. (A) Line depicts the path of blood from artery through arteriole, capillary, venule, and vein. (B) Images of the artery, capillary, and vein in which blood velocity was measured by line scan along the axis are depicted. Diameters of the vessels were measured transaxially. (C) Velocity tracing, as calculated from line scans. Note that both the velocity and the pulse (the range in velocity) were reduced from artery to capillary to vein. (**D**) Table summarizes measurements in control and Notch4* mutant mice. (**E** to **L**) Two-photon time-lapse imaging of cortical brain vessels through a cranial window in *Notch4** mutant mice. Vessel topology was visualized by intravenous FITC-dextran. AV shunts (E and F) were reduced in diameter after the repression of *Notch4** by doxycycline (G to L). Centerline velocity in the regressing AV shunt was obtained by direct measurement of the velocity of individual red blood cells (F, H, J, and L). Repression of *Notch4** decreased blood flow velocity in the AV shunt within 48 hours (compare F to H). (**M**) Quantification of the changes in shunt diameter without repression of *Notch4** (*Notch4**-On) or with repression of *Notch4** (*Notch4**-Off) at 48 hours. Diameter was measured at the narrowest point between artery and vein in *Notch4**-On mice before and after treatment ($n = 22$ AV shunts in 10 mice with and $n = 35$ AV shunts in 11 mice without *Notch4** repression). Reduction in shunt diameter in *Notch4**-On condition is 6% and in *Notch4**-Off condition is 49%. $P < 0.0003$ by Student's *t* test. Error bars represent SEM between individual AV shunts. Scale bars, 50 µm.

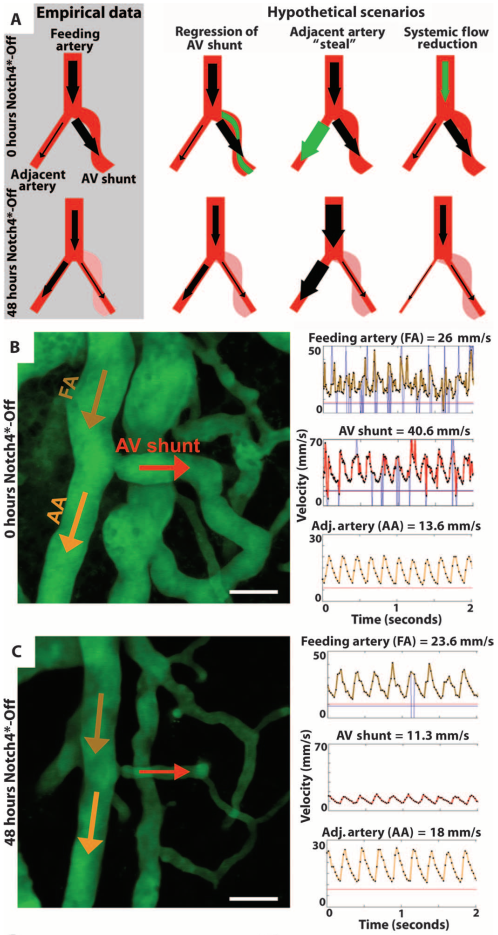

D

Δ Flow

	48 hours Notch4*-Off (n = 7)	48 hours Notch4*-On (n = 8)	
AV shunt	−62.8% ± 10.3	−7.4% ± 17.4	$P = 0.02$
Adj. artery	40.2% ± 25.1	−26.6% ± 18.0	$P = 0.06$
Combined	−47.8% ± 6.7	−7.7% ± 16.0	$P = 0.05$

Fig. 2. AVM narrowing is the primary event in AVM regression. (**A**) Illustration of potential ways in which AV shunt regression takes place. The primary event can be either the acute narrowing of the AV shunt or a reduction in flow, caused by either "steal" from an adjacent artery or a systemic reduction in flow. The acute AV shunt narrowing model, predicting the increase in adjacent artery flow and reduction in feeding artery flow, best fits the empirical observations. We do not observe increased feeding artery flow, as predicted by the adjacent artery steal model, or a decrease in adjacent artery flow, as predicted by a systemic flow reduction model. (**B** and **C**) Two-photon time-lapse imaging of cortical brain vessels through a cranial window in *Notch4** mutant mice. Vessel topology was visualized by plasma labeling by intravenous FITC-dextran. Centerline velocity in the regressing AV shunt, feeding artery (FA), and adjacent artery (AA) was obtained by direct measurement of the velocity of individual red blood cells. Repression of *Notch4** decreased blood flow velocity by 48 hours in shunt and feeding artery but increased velocity in the adjacent artery. (**D**) Summary of percent Δ in calculated flow in vessels either 48 hours after *Notch4** suppression or after 48 hours with no *Notch4** suppression. Scale bars, 50 μm.

from the four mice examined (fig. S11A). Only 9 of the 36 regressing AV shunts exhibited loss of ECs. Twenty-seven AV shunts regressed without detectable loss of ECs (fig. S11B). We did detect EC loss later (fig. S11B), after AV shunt regression, but this was not correlated with either shunt diameter or degree of regression (fig. S11, C and D). An example of this is shown in Fig. 3B, where AV shunt regression was detected between 12 and 20 hours, but cell count was not reduced until 36 hours after Notch4* repression. These data suggest that the initiation of AV shunt regression does not require the loss of ECs.

Ex vivo staining for VE-cadherin, a marker of cell-cell junctions between ECs, in mutant mice before and after repression of *Notch4** suggests that the area encompassed by individual ECs was reduced during vessel regression (fig. S12). Therefore, mean area, but not the total number, of ECs was reduced during the acute regression of AV shunts after *Notch4** repression.

EphB4 is up-regulated in AV shunts after *Notch4** repression

We then asked whether recovery of venous specification, which was repressed in the presence of *Notch4**, might underlie the observed regression of AV shunts after *Notch4** repression. *Coup-TFII* is a venous marker that acts upstream of Notch. Therefore, we hypothesized that *Coup-TFII* expression would be retained in the cells of venous origin in the AV shunt, making it possible to trace the original venous segment and to assess the reestablishment of venous specification upon Notch4* repression. To determine *Coup-TFII* expression, we used a nuclear *lacZ* reporter of *Coup-TFII* promoter activity, *Coup-TFII*$^{+/fl\text{-}stop\text{-}nLacZ}$;*Tie2-Cre* (*5*). The *lacZ* expression is controlled by a floxed-STOP sequence. *Tie2-Cre*–mediated excision ensures that the *lacZ* reports the expression of *Coup-TFII* in *Tie2*$^{+}$ endothelial and hematopoietic cell lineages.

In wild-type control mice, *Coup-TFII* expression was localized to the EC nuclei of the venous branches, including capillaries, but was absent in the arterial branches in the brain (Fig. 4A). In mutant mice expressing *Notch4** (Fig. 4, B and C), regardless of whether *Notch4** was ON or OFF, *Coup-TFII* expression was maintained throughout the venous branches, as in control animals. Thus, *Coup-TFII* expression marked the venous boundary of AV shunts, suggesting that part of the AV shunts originated from the vein.

EphB4, in contrast to Coup-TFII, is a venous marker that acts downstream of Notch (*4*, *16*), making it possible to trace the effects of *Notch4** on the repression of venous specification. We used a *lacZ* reporter of *EphB4* promoter activity (*16*) to examine EphB4 expression before and after *Notch4** repression. In control mice, *EphB4*$^{tau\text{-}lacZ}$ was expressed throughout the veins, venules, and capillaries of the brain vasculature (Fig. 4D). *Notch4** expression decreased the expression of *EphB4*$^{tau\text{-}lacZ}$, resulting in patchy expression in the vein and very little expression in AV shunts (Fig. 4E).

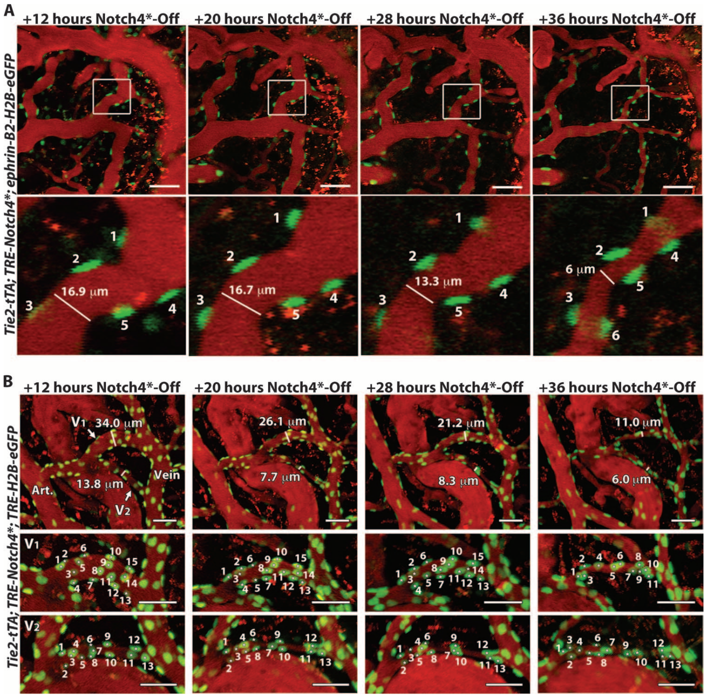

Fig. 3. Regression is initiated by reorganization of ECs. (**A**) Two-photon time-lapse imaging through a cranial window in mouse brain of nuclei marked by *ephrin-B2*$^{+/H2B\text{-}eGFP}$ in a *Notch4** mutant mouse. Plasma was labeled by intravenous Texas Red–dextran. In the AV shunt shown, vessel diameter was reduced by 28 hours after Notch4* repression, whereas the GFP$^+$ nuclei of ECs were retained after vessel regression at 36 hours. Because these images are Z-stacks through the vessel, cell 6 presented at 36 hours was also present earlier but out of the imaging plane. (**B**) Two-photon time-lapse imaging through a cranial window of nuclei marked by *Tie2-tTA/TRE-GFP* in a Notch4* mutant mouse. Plasma was labeled by intravenous Texas Red–dextran. In the AV shunt shown, vessel diameter was reduced by 20 hours after Notch4* repression, whereas the GFP$^+$ nuclei representing ECs were retained at 20 hours, and even at 28 hours when the vessel regressed further. At 36 hours, further regression was evident, and some EC loss was observed in the large shunt, V1, but not in the smaller shunt, V2. Scale bars, 50 μm.

To examine arterial marker expression during vessel regression, we used an ephrin-B2 reporter. We have previously shown that ephrin-B2 expression is up-regulated through the AV shunt in Notch4*-On mutants (*10*). Here, using *ephrin-B2*$^{tau\text{-}lacZ}$ reporter mice, we confirmed this up-regulation (Fig. 4H) and show that ephrin-B2 expression was normalized when Notch4* was turned off (Fig. 4I). To determine whether Notch4* repression leads to the normalization of a broader arterial specification program in the AV shunts, we examined the expression of additional arterial-specific proteins Dll4, Jag1, and Cx40 (Fig. 4, J to U). We found that all of these genes were expressed preferentially in the arteries in control mice; however, their expression extended throughout AV shunts and veins when Notch4* was switched on in mutant mice, and became normalized when Notch4* was switched off (Fig. 4, J to U).

These data, combined with the *Coup-TFII* expression pattern, suggest that *Notch4** induced arterial identity and repressed venous identity in the venous segment of AV shunts. Repression of *Notch4** resulted in the loss of the arterial markers ephrin-B2, Dll4, Jag1, and Cx40 (Fig. 4, I, O, R, and U, respectively) with a concomitant increase in *EphB4* expression in the regressing AV shunts (Fig. 4F).

To determine whether *EphB4* was reexpressed at the cellular level, we used the *TRE-H2B-eGFP* reporter to mark ECs in *Tie2-tTA;TRE-Notch4*;TRE-H2B-eGFP* mice expressing *Notch4** transgenes by eGFP expression (Fig. 5A). We found that EphB4 protein expression was repressed to ~50% of control levels in the *TRE-H2B-eGFP*$^+$ venous ECs of *Tie2-tTA;TRE-Notch4*;TRE-H2B-eGFP* mutant mice relative to *Tie2-tTA;TRE-H2B-eGFP* control mice. Once the Notch4* transgene was turned off, EphB4 expression normalized to control levels in the venous cell population.

Inhibition of EphB4 signaling impairs regression of AV shunts

To determine whether EphB4 signaling is necessary for the regression of AV shunts, we used a soluble form of the EphB4 (sEphB4) receptor to competitively inhibit EphB4 receptor signaling (*17*) after repression of *Notch4** (Fig. 5B). If regression depends on EphB4 signaling, sEphB4 receptor should inhibit the reduction in AV shunt diameter induced by suppression of *Notch4**. Indeed, the mean change in the diameter of AV shunts (−11.5% ± SD 20.8) was significantly reduced relative to mice not treated with sEphB4 (−49.3% ± SD 19.3, $P < 0.004$). As a control for the recombinant protein treatment, we examined AV shunt regression in mice injected with recombinant human fibronectin. The mean change in AV shunt diameter in these mice (39.7% ± SD 16.9) was not significantly different from the regression in mice without recombinant protein treatment ($P > 0.5$). Thus, sEphB4 significantly impaired the regression of AV shunts.

Regression of AV shunts alleviates hypoxia

To investigate the functional effect of AV shunt regression, we asked whether AV shunt regression reversed vascular dysfunction. We first examined blood velocity in arterial branches adjacent to the AV shunt and found that blood velocity increased with *Notch4** repression but decreased with continued *Notch4** expression (Fig. 2D). Markedly, these decreasing velocities could be promptly increased by *Notch4** repression and shunt regression (fig. S5). Perfusion of capillary vessels

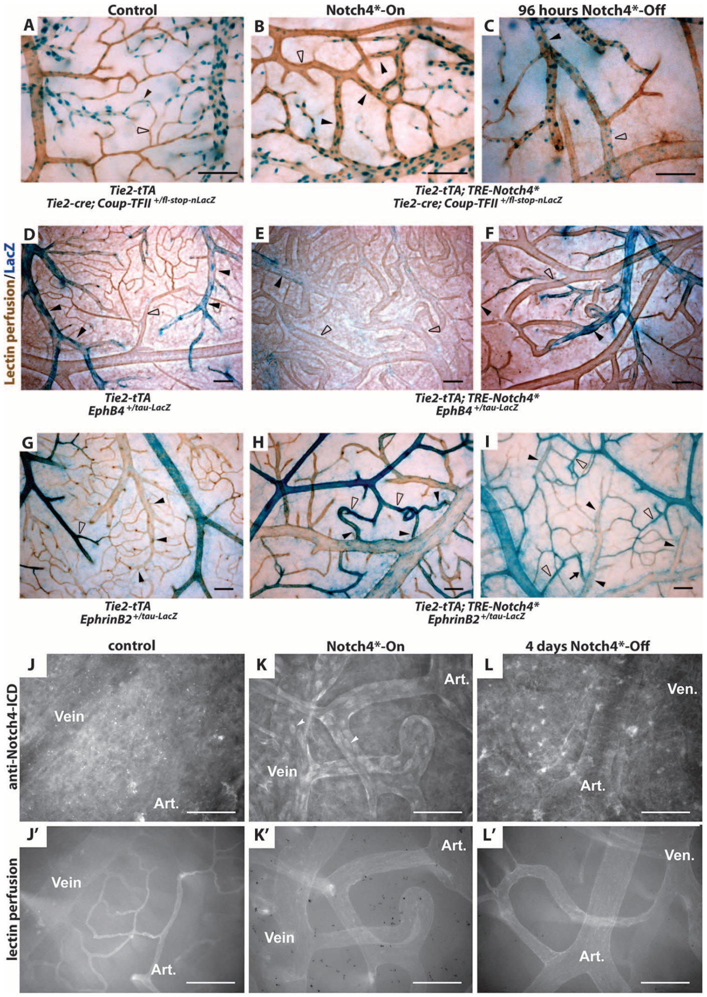

Fig. 4. Turning off Notch4* normalizes AV specification in AV shunts. (**A** to **I**) Whole-mount LacZ staining of the surface vasculature of the cerebral cortex reveals expression of Notch upstream venous specification gene *Coup-TFII*, downstream venous marker *EphB4*, and downstream arterial marker *ephrin-B2*. Perfused vessels were counterstained by colorimetric 3,3′-diaminobenzidine reaction with horseradish peroxidase–bound tomato lectin. (A to C) LacZ staining of *Tie2-cre* activated *Coup-TFII* reporter. (A) In control mice, *Coup-TFII* was expressed in the veins, venules, and capillaries up to the arterioles. (B) In *Notch4**-expressing mutants, *Coup-TFII* was expressed in the vein and venous portion of the AV shunt. (C) After repression of *Notch4**, the narrowest point in AV shunts was found between *Coup-TFII*–positive and *Coup-TFII*–negative endothelium. (D to F) LacZ staining of *EphB4* reporter. (D) In control mice, *EphB4* was expressed in the veins and venules up to the capillaries. (E) In *Notch4**-expressing mutants, *EphB4* expression was reduced through AV shunts, venules, and veins. (F) After the repression of *Notch4**, *EphB4* expression was increased in the regressing AV shunt. (G) In control mice, *ephrin-B2* expression was detected in the arteries and arterioles up to the capillaries. (H) In *Notch4**-expressing mutants, *ephrin-B2* expression was detected in the arteries, the AV shunts, and extending into the veins. (I) After repression of *Notch4**, *ephrin-B2* expression was decreased in the regressing AV shunts and veins. Closed arrowheads indicate venules; open arrowheads indicate arterioles. $n = 3$ (A to C, G, and I), $n = 4$ (H), and $n = 8$ (D to F) for each condition. Scale bars, 100 μm. (**J** to **U**) Whole-mount immunofluorescence staining of cerebral cortex after FITC-lectin perfusion. (J to L) Endothelial localization of Notch4-ICD was undetectable in control mice (J) but was present in a focal manner consistent with nuclear localization throughout the artery and vein in Notch4*-On mice (arrowheads in K); this was reduced once Notch4* was turned off (L). Arterial markers Dll4 (M to O), Jag1 (P to R), and Cx40 (S to U) were expressed in the artery but not the vein in control mice (M, P, and S). All of these markers were up-regulated in the artery, through the AV shunt, and into the vein in Notch4*-On mice (N, Q, and T). When Notch4* was turned off, the expression in the AV shunt and vein was lost but remained in the artery (O, R, and U). $n = 5$ for all mutants, $n = 2$ for each control. Scale bars, 100 μm. See next page for continuation of figure.

(Fig. 6, A to C) with a tomato lectin that binds to the endothelium suggests that tissue perfusion was globally increased after AV shunt regression.

Using hypoxyprobe staining, we then examined hypoxia in *Notch4** mutant mice with neurological defects before and after *Notch4** repression. The hypoxyprobe detects tissue exposed to a partial oxygen pressure of <10 mmHg, close to the hypoxic threshold expected to cause dysfunction of neuronal cells (*18*). We detected an increase in hypoxyprobe staining in the cerebellum and cerebral cortex of sick *Notch4**-expressing mice relative to their littermate controls (Fig. 6, D and F). When *Notch4** was repressed for 72 hours in severely affected *Notch4** mutant mice, hypoxyprobe staining intensity was significantly reduced, and approached that of control animals (Fig. 6E).

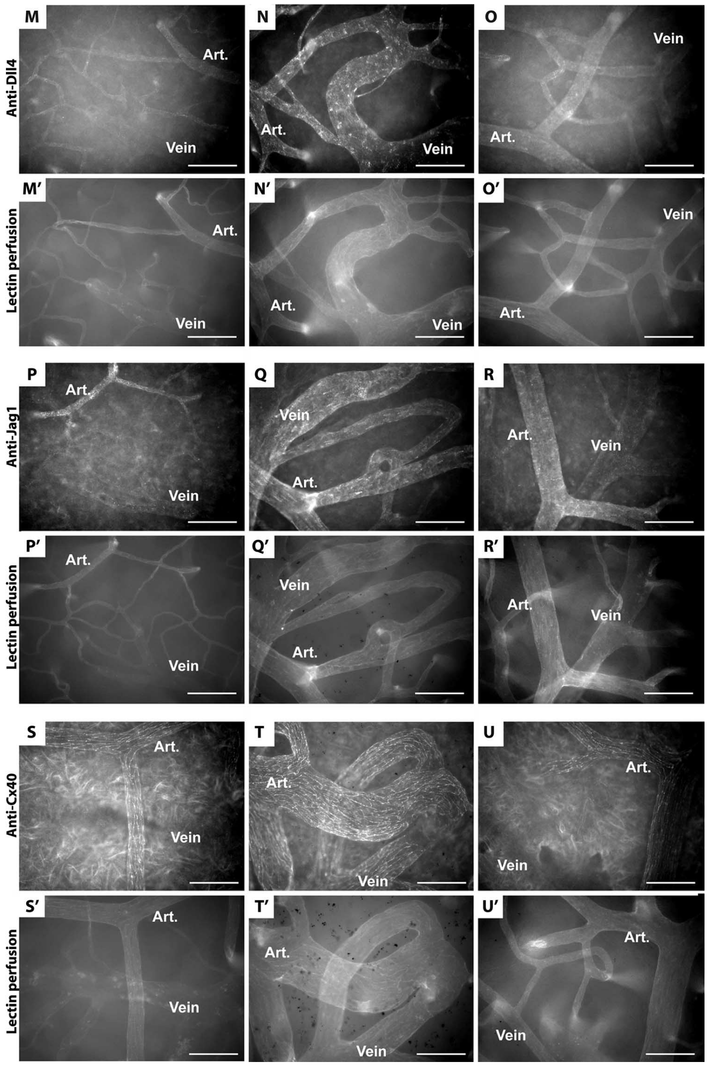

Fig. 4. Turning off Notch4* normalizes AV specification in AV shunts. (Continued from previous page)

Finally, we determined the histopathological changes in the brain parenchyma with and without *Notch4** repression. Histological analysis of *Notch4** mutant mice without *Notch4** repression revealed foci of pyknotic nuclei, often surrounding a core of decreased nuclear density, consistent with ischemia-induced necrosis (four of six mice, Fig. 6G). Such regions occasionally also contained evidence of hemorrhage. *Notch4** repression for several weeks eliminated these pyknotic and acellular regions (nine of nine mice), although structural damage could still be detected (Fig. 6H), presumably representing the evolution of the earlier ischemic damage. In support of this, hemosiderin deposits suggested the resolution of earlier hemorrhages. These findings suggest structural healing of earlier lesions after *Notch4** repression. Thus, regression of AV shunts induced by *Notch4** repression normalizes cerebrovascular flow patterns and tissue oxygenation, providing a physiological explanation for recovered brain function.

DISCUSSION

Here, we report that genetic reprogramming of AV specification converts high-flow AV shunts to low-flow microvessels. Using in vivo time-lapse imaging at single-cell resolution, we show that *Notch4** repression leads to a narrowing of AV shunts that was not dependent on loss of ECs, initiating AVM regression. Mechanistically, this involves the restoration of venous programming in the high-flow AV shunts by *Notch4** repression.

Notch induces reversible arterial programming of the venous compartment

Previously, we have observed expanded expression of the arterial marker *ephrin-B2* in the vasculature after up-regulation of Notch signaling in mice (*10*, *12*, *19*). Arterial ECs in coronary artery development have been reported to arise from venous vessels (*20*). However, it is currently unknown whether venous ECs had been reprogrammed to an arterial specification or whether arterial ECs had expanded. Using venous markers upstream (*Coup-TFII*) (*5*) and downstream (*EphB4*) (*19*) of Notch, we now show that Notch is sufficient to reprogram differentiated venous endothelium in the postnatal mouse. We show here, in normal brain endothelium, that *Coup-TFII* is preferentially expressed in venous but not arterial endothelium. Upstream of Notch, *Coup-TFII* expression is not affected by *Notch4** expression, identifying ECs of venous origin. Expression of *Notch4** led to the misexpression of the arterial markers ephrin-B2, Dll4, Jag1, and Cx40

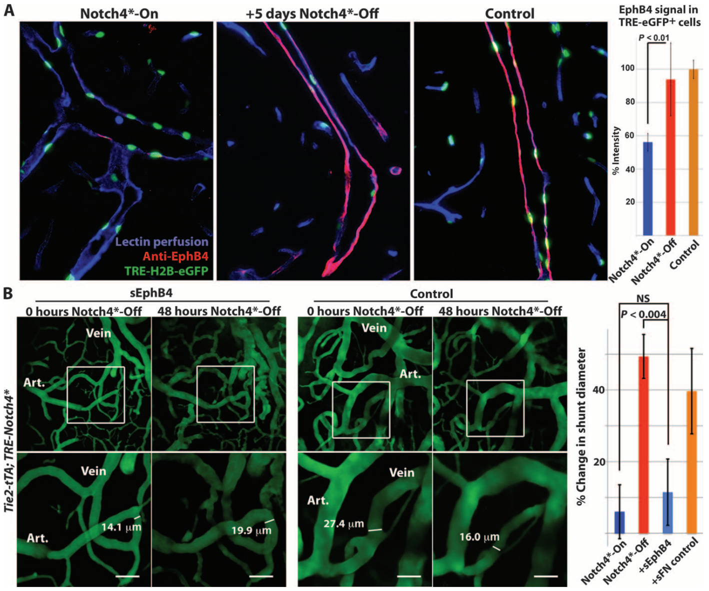

Fig. 5. Venous marker EphB4 is reexpressed in venous ECs and is required for AV shunt regression. (**A**) Sagittal sections showing veins in the cerebellum of *Tie2-tTA;TRE-Notch4*;TRE-H2B-eGFP* mutants before and 5 days after Notch4* repression, with littermate *Tie2-tTA;TRE-H2B-eGFP* control mice. EphB4 expression in TRE-eGFP$^+$ cells was visualized by immunofluorescence staining. EphB4 expression was selectively reduced in Notch4*-expressing mutant mice but recovered after Notch4* repression. Graph shows quantification of EphB4 fluorescence signal intensity in TRE-GFP$^+$ cells. n = 4 for mutants, n = 3 for controls, an average of ~12 cells per vessel and >5 vessels per mouse. (**B**) Two-photon time-lapse imaging of cortical brain vessels through a cranial window in *Notch4** mutant mice. Plasma was labeled by intravenous FITC-dextran. Treating *Notch4** mutant mice with soluble EphB4 (sEphB4) inhibited the regression of the AV shunt examined 48 hours after *Notch4** repression. In a *Notch4** mutant mouse littermate treated with soluble human fibronectin (sFN) as control, the AV shunt was reduced in diameter 48 hours after *Notch4** repression. Shown is quantification of changes in minimal AV shunt diameter after 48 hours in mice without repression of *Notch4** (*Notch4**-On, n = 35 AV shunts in 11 mice), with repression of *Notch4** (*Notch4**-Off, n = 22 AV shunts in 10 mice), with repression of *Notch4** and sEphB4 intravenous treatment (+sEphB4, n = 26 AV shunts in 5 mice), and with repression of *Notch4** and sFN control intravenous treatment (+sFN control, n = 13 AV shunts in 2 mice). Scale bars, 50 µm. Error bars represent SEM between individual AV shunts.

in Coup-TFII–positive veins, confirming that *Notch4** expression converts venous ECs into arterial ECs. Expression of *Notch4** also led to the suppression of the venous marker *EphB4* in the Coup-TFII–positive cells, demonstrating a simultaneous loss of venous expression in ECs of the venous lineage. Besides AV marker expression, venous segments converted by *Notch4** repression also exhibit the features of arteries, including arterial structure and flow velocity. Thus, our data suggest that Notch is sufficient to induce veins to become arteries.

We further demonstrate that this conversion of veins to arteries by Notch up-regulation is reversible. *Notch4** repression led to reexpression of the venous marker *EphB4* in *Coup-TFII*–positive vessels, as well as structural and hemodynamic normalization. Thus, our results suggest that venous vessels induced to become arteries by *Notch4** expression reverted back to veins after repression of *Notch4**. The reversible arterial specification in postnatal vasculature suggests that AV lineage specification is genetically pliable, and a single genetic manipulation is sufficient to switch AV specification postnatally.

AV reprogramming elicits narrowing of high-flow AV shunts without EC loss

The mechanism underlying the regression of AV shunts after *Notch4** repression involves *ephrin-B2* and *EphB4*-mediated EC reorganization, rather than a reduction of EC number. Although the role of *Eph/ephrin* signaling in the endothelium is not yet clear, our finding is consistent with the established functions of *ephrin-B2/EphB4* in regulating cell migration through repulsive signaling (*21*). We think that once reexpressed in *Coup-TFII*$^+$ ECs, *EphB4* mediates *ephrin-B2* signaling and elicits EC repulsion involving actomyosin contraction (Fig. 7). Supporting a critical role for *ephrin-B2/EphB4* signaling in this normalization process, the specific regression of vessels occurs at the AV interface, whereas the adjacent arteries often do not regress. Furthermore, the regression of AV shunts after *Notch4** repression can be blocked by sEphB4.

The mechanism of AV normalization after *Notch4** repression is distinct from the apoptotic mechanism of vessel regression after withdrawal of the growth factor VEGF (vascular endothelial growth factor). Microvessels in tumors and normal tissues regress after VEGF inhibition (*22*). Regression in these vessels is attributed to apoptosis of ECs (*23*). Another model of vessel regression is the hyaloid vasculature of the eye (*24*). In vivo imaging of hyaloid vessel regression shows that apoptosis of ECs obstructs the lumen and capillary blood flow, triggering the apoptosis of remaining ECs in the capillary segment and ultimately its regression (*25*). Thus, apoptosis and a subsequent reduction in blood flow are thought to precipitate vessel regression in these settings.

Our findings suggest that the cellular mechanism underlying the regression of the high-flow vessels after *Notch4** repression does not involve EC apoptosis, but likely is due to reorganization of ECs resulting from restoration of venous identity.

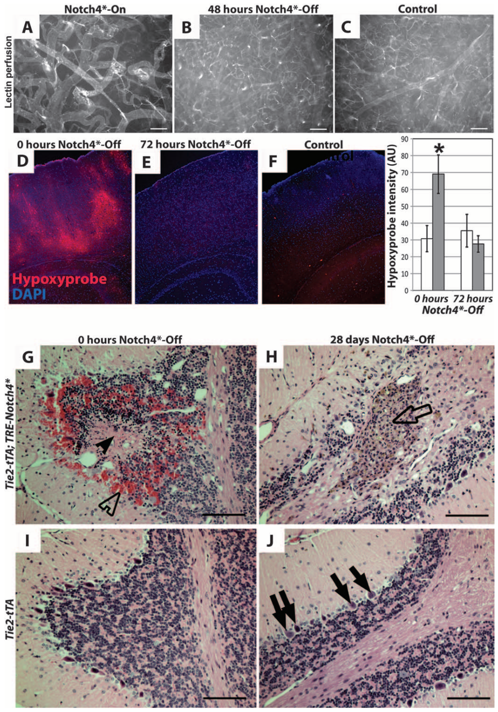

Fig. 6. *Notch4** repression normalizes vascular perfusion and tissue oxygenation. (**A** to **C**) Vascular perfusion of surface vessels of the cerebral cortex by fluorescent tomato lectin. After repression of *Notch4**, capillary perfusion was increased. (**D** to **F**) Immunofluorescence (red) staining for hypoxyprobe (pimonidazole) adduct in coronal section of mouse cortex. Patches of staining were visible in mutant mice with neurological defects before *Notch4** suppression (D). Staining was reduced 72 hours after suppression of *Notch4** (E). Control tissue shows an absence of staining (F). Quantification of staining intensity in cortical brain relative to nonspecific immunoglobulin G controls. Control before treatment is 30.8 arbitrary units (AU) ± SD 20.6; Notch4* mutant before treatment is 69.0 AU ± SD 34.2; control after treatment is 35.5 AU ± SD 25.6; Notch4* mutant after treatment is 27.6 AU ± SD 13.8. $P < 0.05$ versus all other groups by one-way analysis of variance (ANOVA) and Newman-Keuls multiple comparison test. $n = 9$ at 0 hours *Notch4**-Off, $n = 8$ at 72 hours *Notch4**-Off. (**G** to **J**) Hematoxylin and eosin staining of sagittal paraffin sections of cerebellum. In *Notch4** mutant mice before *Notch4** repression (0 hours *Notch4**-Off), areas of hemorrhage (open arrowhead) and necrotic tissue (closed arrowhead) were visible (G). After 28 days of *Notch4** suppression (28 days *Notch4**-Off), areas of scarring were visible (open arrow), but areas of hemorrhage and necrotic tissue had been resolved (H). The numbers of Purkinje cells were decreased in (H) when compared to these cells in the corresponding area in control (J) (solid arrows). Granular cells [open arrow in (H)] were found in the scarred area. Scale bars, 100 μm.

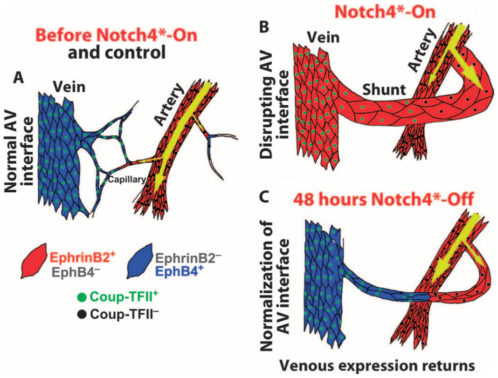

Fig. 7. Model for AVM regression after *Notch4** repression. (**A**) In control mice, Notch and ephrin-B2 are expressed in arteries and capillaries. Coup-TFII and EphB4 are expressed in veins and capillaries. (**B**) In mutant mice, *Notch4** is forcibly expressed throughout the endothelium, causing the repression of EphB4 and the expression of ephrin-B2 in AV shunts. The venous marker Coup-TFII, upstream of Notch, is retained, demarcating the original arterial-venous boundary. (**C**) Repression of *Notch4** allows EphB4 to be reexpressed in the Coup-TFII^{+} venous segment. Normalization of ephrin-B2/EphB4 signaling in ECs results in their reorganization, which initiates AV shunt narrowing and AVM regression.

Future implications

Direct in vivo imaging in this study demonstrates the regression of high-flow large vessels to capillary-like vessels by a single genetic manipulation that represses expression of *Notch4**. Markedly, vascular normalization was not accompanied by hemorrhage and vascular damage. Rather, AV shunt regression safely reversed tissue hypoxia and tissue dysfunction. We have focused on AVMs in mouse brain, but the finding likely applies to AVMs in other tissues given that we have previously identified *Notch4**-mediated AVMs in the liver, skin, uterus, and lung in the mouse (*12*, *19*, *26*). Thus, we believe that exploiting the tractable brain AVM mouse model system will provide important clues into the cellular and molecular regulation of AVMs in general. AV shunts are a core component of a range of high-flow vascular lesions (*1*). Thus, our demonstration of complete and safe normalization of dangerous high-flow AV shunts in animals may spur development of molecular therapeutic strategies to induce the regression of these dangerous high-flow vessels and treat these devastating diseases.

MATERIALS AND METHODS

Mice

Tie2-cre, *Tie2-tTA*, and *TRE-Notch4** mice are published (*8*, *10*, *12*, *19*), as are *ephrin-B2*$^{+/H2B\text{-}eGFP}$ (*27*), *EphB4*$^{+/tau\text{-}lacZ}$ (*16*), *ephrin-B2*$^{+/tau\text{-}lacZ}$ (*4*), *mT/mG* (*28*), *TRE-H2B-eGFP* (*29*), and *Coup-TFII*$^{+/fl\text{-}stop\text{-}nLacZ}$ mice (*30*). Tetracycline solution [Tet (0.5 mg/ml), sucrose (50 mg/ml), Sigma] was administered to mothers and withdrawn at birth (*10*). Doxycycline treatment was initiated with intraperitoneal injection

[500 μl of 1 mg/ml in phosphate-buffered saline (PBS)], followed by doxycycline diet (200 mg/kg, Bio-Serv) (*10*, *12*). All animals were treated in accordance with the guidelines of the University of California San Francisco Institutional Animal Care and Use Committee.

sEphB4 treatment

Two hundred microliters of recombinant human EphB4 extracellular domain (200 μg/ml) (R&D Systems) was injected by tail vein (final concentration of ~4 mg/kg), followed by 100 μl of 200 μg/ml 24 hours later (*17*). Recombinant human fibronectin (R&D Systems) at the same concentration was a negative control.

In vivo imaging

Chronic in vivo brain vascular imaging was performed as described (*11*, *31*), with modifications for immature mice (*32*). Briefly, a craniotomy was performed over the right cortex. A 5-mm glass coverslip (World Precision Instruments) was placed over artificial cerebrospinal fluid and fixed into place. A custom metal bar was attached adjacent to the window, allowing it to be secured by a custom adaptor arm on a stereotactic base (Cunningham). For imaging, mice were anesthetized with isoflurane (1.25 to 1.5%) in pure oxygen on a homeothermic heat blanket (Harvard Apparatus). Fluorescent contrast agents were injected by tail vein [2000-kD fluorescein isothiocyanate (FITC)–dextran (Sigma), 155-kD tetramethyl rhodamine isothiocyanate (TRITC)–dextran (Sigma), or 2000-kD Texas Red–dextran, prepared according to published protocols (*33*) and filtered by dialysis]. Two-photon microscopy was performed with a locally constructed microscope, to be described in detail in a future publication.

Immunostaining

Conjugated *Lycopersicon esculentum*–lectin (Vector Labs) was injected as we described (*10*, *12*). Brain was fixed by 1% paraformaldehye (PFA) fixation via the left ventricle. Tissue was incubated in blocking solution [2% bovine serum albumin (BSA), 0.1% Triton X-100 in PBS], primary antibody overnight, and secondary antibody overnight. Antibodies were anti–VE-cadherin (BD Pharmingen, clone 11D4.1, 1:200 dilution) and anti–α-smooth muscle actin (Sigma, clone 1A4, 1:200 dilution) (*12*, *34*). Staining for AV marker expression followed a similar protocol, except that blocking was with 10% donkey serum and 0.1% Triton X-100 in PBS. Antibodies (2 μg/ml in block) were anti–Notch4-ICD (intracellular domain) (Millipore), anti-Jag1 (R&D Systems), anti-Dll4 (R&D Systems), and anti-Cx40 (Santa Cruz).

Notch4 staining followed published protocols (*10*). Briefly, brains were perfusion-fixed with or without previous *L. esculentum*–lectin (Vector Labs) injection. After overnight fixation in 1% PFA, brains were sagitally bisected and dehydrated in 30% sucrose in PBS overnight and embedded in OCT (optimal cutting temperature). Sections (10 μm) were cut, blocked (3% donkey serum, 2% BSA, 0.2% Triton X-100 in PBS), and then incubated with anti–Notch4-ICD antibody (Millipore, formerly Upstate, 1:500 dilution) overnight in block, washed, incubated with secondary antibody, washed, and stored in VectaShield + DAPI (Vector Labs).

X-galactosidase/3,3′-diaminobenzidine co-staining

Under ketamine/xylazine and isoflurane anesthesia, 25 μg of biotinylated *L. esculentum*–lectin (Vector Labs) was injected via the inferior vena cava and allowed to circulate for 2 min. Perfusion was performed through the left ventricle with PBS, followed by fixative (0.25% glutaraldehyde, 50 mM EGTA, and 100 mM $MgCl_2$ in PBS). After short fixation, the cortex was stained for β-galactosidase at room temperature according to published X-galactosidase protocols (*35*). The cortex was then fixed with 1% PFA and blocked (10% BSA and 0.1% Triton X-100 in PBS), incubated with 1:1000 streptavidin-conjugated horseradish peroxidase (Jackson ImmunoResearch) in block, washed, and stained with a DAB (3,3′-diaminobenzidine) kit (Vector Labs).

SUPPLEMENTARY MATERIAL

www.sciencetranslationalmedicine.org/cgi/content/full/4/117/117ra8/DC1
Fig. S1. *Notch4** repression occurs within 24 hours of doxycycline treatment.
Fig. S2. Placement of the chronic imaging window.
Fig. S3. Specific regression of AV shunts after repression of *Notch4**.
Fig. S4. Repression of Notch4* induces regression of well-established large AV malformation.
Fig. S5. AV shunts are stable until repression of *Notch4**.
Fig. S6. AV shunts regress to capillary diameter vessels in mice with and without cranial window.
Fig. S7. Smooth muscle coverage is normalized by suppression of Notch4*.
Fig. S8. Velocity changes coincide with narrowing of AV shunts and distal vein beginning by 12 to 24 hours after *Notch4** repression.
Fig. S9. Narrowing of ephrin-B2–GFP^+ AV shunt occurs specifically after *Notch4** repression.
Fig. S10. *Tie2-tTA;TRE-H2B-eGFP* marks brain endothelial cells.
Fig. S11. Loss of endothelial cells is not required for AV shunt regression.
Fig. S12. Endothelial cells are narrowed in regressing AV shunts.

REFERENCES AND NOTES

1. M. C. Garzon, J. T. Huang, O. Enjolras, I. J. Frieden, Vascular malformations: Part I. *J. Am. Acad. Dermatol.* **56**, 353–370 (2007).
2. R. M. Friedlander, Clinical practice. Arteriovenous malformations of the brain. *N. Engl. J. Med.* **356**, 2704–2712 (2007).
3. C. Roca, R. H. Adams, Regulation of vascular morphogenesis by Notch signaling. *Genes Dev.* **21**, 2511–2524 (2007).
4. H. U. Wang, Z. F. Chen, D. J. Anderson, Molecular distinction and angiogenic interaction between embryonic arteries and veins revealed by ephrin-B2 and its receptor Eph-B4. *Cell* **93**, 741–753 (1998).
5. L. R. You, F. J. Lin, C. T. Lee, F. J. DeMayo, M. J. Tsai, S. Y. Tsai, Suppression of Notch signalling by the COUP-TFII transcription factor regulates vein identity. *Nature* **435**, 98–104 (2005).
6. D. Shin, G. Garcia-Cardena, S. Hayashi, S. Gerety, T. Asahara, G. Stavrakis, J. Isner, J. Folkman, M. A. Gimbrone Jr., D. J. Anderson, Expression of ephrinB2 identifies a stable genetic difference between arterial and venous vascular smooth muscle as well as endothelial cells, and marks subsets of microvessels at sites of adult neovascularization. *Dev. Biol.* **230**, 139–150 (2001).
7. R. Benedito, A. Duarte, Expression of *Dll4* during mouse embryogenesis suggests multiple developmental roles. *Gene Expr. Patterns* **5**, 750–755 (2005).
8. P. A. Murphy, G. Lu, S. Shiah, A. W. Bollen, R. A. Wang, Endothelial Notch signaling is upregulated in human brain arteriovenous malformations and a mouse model of the disease. *Lab. Invest.* **89**, 971–982 (2009).
9. Q. ZhuGe, M. Zhong, W. Zheng, G. Y. Yang, X. Mao, L. Xie, G. Chen, Y. Chen, M. T. Lawton, W. L. Young, D. A. Greenberg, K. Jin, Notch-1 signalling is activated in brain arteriovenous malformations in humans. *Brain* **132**, 3231–3241 (2009).
10. P. A. Murphy, M. T. Lam, X. Wu, T. N. Kim, S. M. Vartanian, A. W. Bollen, T. R. Carlson, R. A. Wang, Endothelial Notch4 signaling induces hallmarks of brain arteriovenous malformations in mice. *Proc. Natl. Acad. Sci. U.S.A.* **105**, 10901–10906 (2008).
11. C. B. Schaffer, B. Friedman, N. Nishimura, L. F. Schroeder, P. S. Tsai, F. F. Ebner, P. D. Lyden, D. Kleinfeld, Two-photon imaging of cortical surface microvessels reveals a robust redistribution in blood flow after vascular occlusion. *PLoS Biol.* **4**, e22 (2006).
12. T. R. Carlson, Y. Yan, X. Wu, M. T. Lam, G. L. Tang, L. J. Beverly, L. M. Messina, A. J. Capobianco, Z. Werb, R. Wang, Endothelial expression of constitutively active *Notch4* elicits reversible arteriovenous malformations in adult mice. *Proc. Natl. Acad. Sci. U.S.A.* **102**, 9884–9889 (2005).
13. M. Unekawa, M. Tomita, Y. Tomita, H. Toriumi, K. Miyaki, N. Suzuki, RBC velocities in single capillaries of mouse and rat brains are the same, despite 10-fold difference in body size. *Brain Res.* **1320**, 69–73 (2010).
14. E. A. Jones, F. le Noble, A. Eichmann, What determines blood vessel structure? Genetic prespecification vs. hemodynamics. *Physiology* **21**, 388–395 (2006).
15. E. Fuchs, The tortoise and the hair: Slow-cycling cells in the stem cell race. *Cell* **137**, 811–819 (2009).

16. S. S. Gerety, H. U. Wang, Z. F. Chen, D. J. Anderson, Symmetrical mutant phenotypes of the receptor *EphB4* and its specific transmembrane ligand *ephrin-B2* in cardiovascular development. *Mol. Cell* **4**, 403–414 (1999).
17. N. Kertesz, V. Krasnoperov, R. Reddy, L. Leshanski, S. R. Kumar, S. Zozulya, P. S. Gill, The soluble extracellular domain of EphB4 (sEphB4) antagonizes EphB4-EphrinB2 interaction, modulates angiogenesis, and inhibits tumor growth. *Blood* **107**, 2330–2338 (2006).
18. E. L. Rolett, A. Azzawi, K. J. Liu, M. N. Yongbi, H. M. Swartz, J. F. Dunn, Critical oxygen tension in rat brain: A combined ^{31}P-NMR and EPR oximetry study. *Am. J. Physiol. Regul. Integr. Comp. Physiol.* **279**, R9–R16 (2000).
19. Y. H. Kim, H. Hu, S. Guevara-Gallardo, M. T. Lam, S. Y. Fong, R. A. Wang, Artery and vein size is balanced by Notch and ephrin B2/EphB4 during angiogenesis. *Development* **135**, 3755–3764 (2008).
20. K. Red-Horse, H. Ueno, I. L. Weissman, M. A. Krasnow, Coronary arteries form by developmental reprogramming of venous cells. *Nature* **464**, 549–553 (2010).
21. M. E. Pitulescu, R. H. Adams, Eph/ephrin molecules—A hub for signaling and endocytosis. *Genes Dev.* **24**, 2480–2492 (2010).
22. R. K. Jain, Normalization of tumor vasculature: An emerging concept in antiangiogenic therapy. *Science* **307**, 58–62 (2005).
23. F. Baffert, T. Le, B. Sennino, G. Thurston, C. J. Kuo, D. Hu-Lowe, D. M. McDonald, Cellular changes in normal blood capillaries undergoing regression after inhibition of VEGF signaling. *Am. J. Physiol. Heart Circ. Physiol.* **290**, H547–H559 (2006).
24. I. B. Lobov, S. Rao, T. J. Carroll, J. E. Vallance, M. Ito, J. K. Ondr, S. Kurup, D. A. Glass, M. S. Patel, W. Shu, E. E. Morrisey, A. P. McMahon, G. Karsenty, R. A. Lang, WNT7b mediates macrophage-induced programmed cell death in patterning of the vasculature. *Nature* **437**, 417–421 (2005).
25. A. Meeson, M. Palmer, M. Calfon, R. Lang, A relationship between apoptosis and flow during programmed capillary regression is revealed by vital analysis. *Development* **122**, 3929–3938 (1996).
26. D. Miniati, E. B. Jelin, J. Ng, J. Wu, T. R. Carlson, X. Wu, M. R. Looney, R. A. Wang, Constitutively active endothelial Notch4 causes lung arteriovenous shunts in mice. *Am. J. Physiol. Lung Cell. Mol. Physiol.* **298**, L169–L177 (2010).
27. A. Davy, J. O. Bush, P. Soriano, Inhibition of gap junction communication at ectopic Eph/ephrin boundaries underlies craniofrontonasal syndrome. *PLoS Biol.* **4**, e315 (2006).
28. M. D. Muzumdar, B. Tasic, K. Miyamichi, L. Li, L. Luo, A global double-fluorescent Cre reporter mouse. *Genesis* **45**, 593–605 (2007).
29. T. Tumbar, G. Guasch, V. Greco, C. Blanpain, W. E. Lowry, M. Rendl, E. Fuchs, Defining the epithelial stem cell niche in skin. *Science* **303**, 359–363 (2004).
30. N. Takamoto, L. R. You, K. Moses, C. Chiang, W. E. Zimmer, R. J. Schwartz, F. J. DeMayo, M. J. Tsai, S. Y. Tsai, *COUP-TFII* is essential for radial and anteroposterior patterning of the stomach. *Development* **132**, 2179–2189 (2005).
31. A. Holtmaat, T. Bonhoeffer, D. K. Chow, J. Chuckowree, V. De Paola, S. B. Hofer, M. Hübener, T. Keck, G. Knott, W. C. Lee, R. Mostany, T. D. Mrsic-Flogel, E. Nedivi, C. Portera-Cailliau, K. Svoboda, J. T. Trachtenberg, L. Wilbrecht, Long-term, high-resolution imaging in the mouse neocortex through a chronic cranial window. *Nat. Protoc.* **4**, 1128–1144 (2009).
32. C. Portera-Cailliau, R. M. Weimer, V. De Paola, P. Caroni, K. Svoboda, Diverse modes of axon elaboration in the developing neocortex. *PLoS Biol.* **3**, e272 (2005).
33. S. Hornig, C. Biskup, A. Gräfe, J. Wotschadlo, T. Liebert, G. J. Mohr, T. Heinze, Biocompatible fluorescent nanoparticles for pH-sensoring. *Soft Matter* **4**, 1169–1172 (2008).
34. R. Braren, H. Hu, Y. H. Kim, H. E. Beggs, L. F. Reichardt, R. Wang, Endothelial FAK is essential for vascular network stability, cell survival, and lamellipodial formation. *J. Cell Biol.***172**, 151–162 (2006).
35. B. Carpenter, Y. Lin, S. Stoll, R. L. Raffai, R. McCuskey, R. Wang, VEGF is crucial for the hepatic vascular development required for lipoprotein uptake. *Development* **132**, 3293–3303 (2005).

Acknowledgments: We thank C. Tomas-Miranda and W. Jiang for experimental assistance, S. Tsai for the *Coup-TFII*$^{+/fl\text{-}stop\text{-}nLacZ}$ mice, R. Daneman for critical reading, and members of our laboratory for helpful discussions. **Funding:** This work was supported by the Foundation for Accelerated Vascular Research (formerly the Pacific Vascular Research Foundation), the Frank A. Campini Foundation, the Mildred V Strouss Trust, NIH R01 HL075033, NIH RO1 NS067420, and American Heart Association (AHA) grant-in-aid 10GRNT4170146 to R.A.W.; AHA 0715062Y and Tobacco-Related Disease Research Program (TRDRP) 18DT-0009 Predoctoral Fellowships to P.A.M.; TRDRP 19DT-007 and NIH F30 1F30HL099005-01A1 Predoctoral Fellowships to T.N.K.; and the University of California San Francisco Liver Center Morphology Core supported by NIH P30-DK026743. **Author contributions:** P.A.M., R.A.W., and T.N.K. designed the experiments; P.A.M., T.N.K., and G.L. performed the experiments; P.A.M., R.A.W., T.N.K., G.L., and A.W.B. analyzed the data; T.N.K., C.B.S., and P.A.M. contributed tools and technology; and P.A.M. and R.A.W. wrote the paper. **Competing interests:** The authors declare that they have no competing interests.

Submitted 17 May 2011
Accepted 22 December 2011
Published 18 January 2012
10.1126/scitranslmed.3002670

Citation: P. A. Murphy, T. N. Kim, G. Lu, A. W. Bollen, C. B. Schaffer, R. A. Wang, *Notch4* normalization reduces blood vessel size in arteriovenous malformations. *Sci. Transl. Med.* **4**, 117ra8 (2012).

V

Constitutively active Notch4 causes brain arteriovenous malformation from capillary-like vessels through endothelial reprogramming

Introduction

Brain arteriovenous malformations (BAVMs) are a dangerous condition characterized by enlarged, tangled shunts that bypass normal capillary beds. These high-flow lesions are believed to persist and enlarge under the influence of blood flow[1,2], and abnormal hemodynamic stress exerted on the vasculature can lead to life-threatening ruptures[1,2]. Hemodynamic forces have been recognized to play a role in shaping blood vessels and were once thought to be the primary determinants of arteriovenous (AV) identity[3,4,5,6]. More recently, biochemical programs have been identified that are involved in specifying arteries and veins prior to circulation[7] raising important questions on the interplay of genetic and hemodynamic cues in development and maintenance of the AV hierarchy[7,8]. Elucidating the origin and pathogenesis of AVMs will provide a fundamental understanding of how the AV network is maintained and balanced in the living organism.

Observations in human skin AVMs suggest that these defects are initiated by the enlargement of post-capillary venules and grow over time[9]. In contrast, brain AVMs are often discovered in younger people and have morphologic similarities to early vasculature, leading to the favored model that BAVMs are a result of failed remodeling from embryonic development persisting as congenital lesions into adulthood [10,11]. A number of studies have identified mutations that are important for vascular development and lead to embryonic AVMs [2,12,13,14]. However, these genetic defects are also embryonic lethal and it remains unclear if they account for the presentation of AVMs in people. An alternative model is the *de novo* formation of postnatal AVMs, which could potentially arise from the fusion of arteries and veins or the enlargement of pre-existing capillaries. Such mechanisms would demonstrate the plasticity of the AV network and provide insight into programs that distinguish arteries and veins later in life.

We recently reported that expression of activated Notch4 (Notch4*) in endothelial cells results in AVMs in young and adult mice[15,16]. Additionally, we and others have linked increased Notch signaling in ECs with human brain AVMs[17,18], suggesting an important role for this signaling pathway in the pathogenesis of the disease. Notch signaling is an exquisitely sensitive regulator of lineage decisions in many aspects of embryonic development[19,20] and has emerged as a critical mediator in the arterial specification of endothelial cells. In embryo, Notch loss-of-function mutations exhibit enlarged arteriovenous connections with decreased expression of arterial marker ephrinB2 and increased expression of venous marker EphB4 ectopically in arteries[30,35] [12,13]. We found that expression of Notch4* in ECs resulted in upregulation of ephrin-B2 and concomitant reduction of EphB4 in AVMs and veins[16,21] in postnatal mice, suggesting that the balance of Notch activity is important both for AV development as well as maintenance.

We use our Notch-mediated mouse model of AVMs and *in vivo* two-photon laser scanning microscopy (TPLSM) to acquire vessel topology and blood velocity data over time in the neonatal brain. Here, we find that Notch activity in non-arterial vessels leads to the enlargement of pre-existing capillaries, thereby causing shunting and progressive growth of AVMs.

Results

Brain arteriovenous malformation is a devastating disease with poorly understood etiology. These tortuous, high-flow lesions are often identified before the age of 30 and demonstrate morphologic characteristics similar to embryonic vessels, leading to the hypothesis that brain AVMs arise from defects in early vascular development [2,6 PD]. However, this theory remains speculative due to the paucity of chronic imaging data on AVM development. We have previously reported a mouse model of AVM (*Tie2-tTA;TRE-Notch4*)* wherein Notch4*, a truncated and constitutively active Notch4 receptor, is expressed in ECs using the temporally regulatable tetracycline-responsive system [STM 12]. Expression of Notch4* is under control of the tetracycline-responsive element (TRE) and is activated by the tetracycline transactivator (tTA) which is driven in ECs by the Tie2 promoter. Induction of Notch4* in adulthood caused AVMs in liver, skin, and uterus [ref] and induction in neonatal life caused brain AVMs as early as postnatal day 12 (P12) [ref]. The temporal control of this system is an important feature offering the study of spontaneous AVM formation. We speculated that AVMs arise in our model by one of two possibilities: (1) the enlargement of pre-existing capillaries or (2) de novo connections that form between arteries and veins. To dynamically study the developmental origin of these AVMs, we implanted cranial windows over the right parietal cortex of young animals about P7 and employed *in vivo* two-photon laser-scanning microscopy (TPLSM) to record vessel topology and hemodynamics over time.

*Notch4**-mediated AVMs arise from the primary enlargement of capillary-like vessels

Multiple brain vascular fields were obtained across each cranial window using *in vivo* TPLSM. The blood plasma was labeled with high-molecular weight fluorescein-dextran, revealing branching networks of surface and penetrating vessels. Candidate regions for time-lapse imaging were selected based upon identifiable arteries and veins within the same field of view that were joined by capillary-like vessels. By daily imaging, we observed AV shunts enlarge from what appeared to be pre-existing capillaries (44/103 vessels in 8 mice). These lesions progressively enlarged in caliber (**Figure 1A, Supplemental movies 1 and 2**) while other capillary-like vessels did not enlarge (22/103 vessels in 8 mice) or pruned away over time (37/103 vessels in 8 mice). Control capillaries did not enlarge over time (**Figure 1B**). Large-scale involvement of the brain was examined at an advanced stage of disease by casting the vasculature with radio-opaque microfil and imaging with microCT. Here, we found that AVMs were extremely large and directly connected the largest branches of the middle cerebral artery and draining veins (**Supplemental Figure 1**). Interestingly, these branches were generally associated with one large AVM, suggesting that only a few of the initial AV shunts had progressed to this size.

AVMs have long been speculated to persist and enlarge under the influence of high blood flow [refs], however, the intrinsic coupling between flow and low-resistance shunts has obscured whether one may be the initiating pathology. Capillaries are necessarily the lowest flow vessels in the body and allow nutrient and waste exchange between the tissue and circulation. To test whether dysregulation in blood flow or vessel diameter was the primary defect, we examined the temporal relationship between increased blood velocity and lumen diameter during the onset of AV shunts. Red blood cell (RBC) velocities were analyzed from line-scans recorded along the narrowest vessel segments joining arteries and veins [refs]. **Figure 1C** shows the relationship between lumen diameter and blood velocity in three representative capillary-like vessels that were studied over time. Abnormal increases were determined as greater than twice the standard deviation of physiologic variability in capillaries of control animals. The initial enlargement of lumen diameter in AV shunts either coincided with the initial increase in velocity (4/18 capillary-like vessels in 4 mice) or preceded the initial increase in velocity (4/18 capillary-like vessels in 4 mice). Some capillary-like vessels enlarged without any significant increase in velocity during the acquisition period of several days (4/18 capillary-like vessels in 4 mice), while others exhibited neither an increase in diameter or velocity (6/18 capillary-like vessels in 4 mice). **Figure 1D** shows representative examples of lumen diameter and blood velocity in capillaries from control mice. The initial increase in velocity and diameter of AV shunts are visually depicted in **Figure 1E**. Note that the initial increase in diameters either coincided with or preceded the initial increase in velocities. These results suggest that the initial enlargement of capillary-like vessels may occur prior to blood flow changes and is the initiating pathology leading to AV shunts in our mouse model.

Expression of Notch4* in postnatal life rapidly converts cerebral capillary-like vessels into AV shunts

We examined Notch4-ICD staining in a subset of animals at ages P10, P12, and P18 to test whether Notch4* expression was rapidly associated with the onset of AV shunts (**Figure 2A**). These ages were selected to correspond with periods before AV shunts, coincident with onset of AV shunts, and after the formation of brain AVMs, respectively. Anti-Notch4-ICD was quantified by immunofluorescence in nuclei of endothelial cells as previously described [22,23]. Because Notch4* is a portion of the Notch4 receptor, the anti-Notch4-ICD staining could not distinguish Notch4* from endogenous Notch4. Therefore, nuclear accumulation of Notch4-ICD in mutant mice was normalized between age- and experiment-matched controls to evaluate the relative increase in Notch4-ICD (**Figure 2B**). Mutant mice exhibited 7.1±1.96% increase in staining relative to controls at P10. Staining in mutants increased by 40.1±5.1%, and 83.4±3.6% at P12 and P18, respectively. These animals also contained the *TRE-H2B-GFP* reporter [24], where expression of Notch4* and nuclear GFP were regulated in ECs by the *Tie2-tTA* construct [21]. GFP and Notch4-ICD staining intensities were positively correlated in EC nuclei of Notch4* mice (Pearson r = 0.5286, P value < 0.0001, **Supplemental Figure 2**), where 90.7% of GFP+ cells (greater than x3 background intensity) had a greater than 20% increase in Notch4-ICD staining relative to controls. We utilized TRE-H2B-GFP as a fluorescent method to monitor the spatio-temporal 'on' expression of transgene by *in vivo* TPLSM (**Figure 2C**). AVMs arose from capillary-like vessels that acquired GFP+ cells shortly before their enlargement into AV shunts (18/19 AVMs in 5 mice, Figure 2D). The enlargement of these vessels was correlated with the number of GFP+ nuclei that they contained (Pearson r = 0.7713, P value < 0.0001, **Figure 2D**). These results indicate that Notch4* expression increased shortly before the enlargement of capillary-like vessels, suggesting that AV shunts developed from the normal vasculature in postnatal life.

AV specification in cerebral vessels appears normal prior to onset of AV shunts

We then asked whether the AV specification of the vasculature was abnormal just prior to the onset of AV shunts in Notch4* mice. We therefore examined the expression pattern of arteriovenous markers that act either downstream or independently of Notch4 signaling. To examine arterial marker expression, we utilized the Notch1$^{+/\text{nlacZ}}$ [ref] reporter and ephrin-B2$^{+/\text{tau-lacZ}}$ mice [7]. Notch1 is arterial marker that acts in parallel with Notch4 in ECs. LacZ expression is nuclear in the Notch1$^{+/\text{nlacZ}}$ reporter, which was restricted to arteries in Notch4* and control mice without labeling capillaries or veins (**Figure 3A and 3B**). We previously reported AVMs in Notch4* mice exhibited arterial specification by increased expression of Notch-downstream arterial marker ephrin-B2 [21][and PNAS]. Here, we demonstrate ephrin-B2 expression is restricted to arteries in Notch4* and control mice without the presence of AV shunts at P10 (**Figure 3C and 3D**).

Next, we examined venous marker expression using EphB4$^{+/\text{tau-lacZ}}$ [8] and Coup-TFII$^{+/\text{fl-stop/nlacZ}}$; Tie2-Cre [P5, STM] mice. Coup-TFII is a venous marker upstream of Notch signaling [Tsai reference]. LacZ expression is nuclear in the Coup-TFII$^{+/\text{fl-stop/nlacZ}}$ mice and controlled by a flox-STOP sequence. Tie2-Cre enabled lacZ to report Coup-TFII in Tie2+ endothelium and hematopoietic lineages, which was expressed throughout the veins and into the capillaries in mutants and controls without AV shunts (**Figure 3E and 3F**). We previously reported Notch4* mice exhibited suppression of Notch-downstream venous marker EphB4 in AVMs and veins [21]. At P10, EphB4 is expressed throughout the veins of mutant and control mice without the presence of AV shunts (**Figure 3G and 3H**). Taken together, these results suggest that the arteriovenous specification of the vasculature in mutants was normal within a day or two of initial enlargement of AV shunts.

AVM formation is mediated through canonical Notch signaling

RBP-J, a DNA-binding protein, is ubiquitously expressed and is a critical mediator of canonical signaling of all four types of the Notch receptor [25]. The Notch intracellular domain translocates to the nucleus and acts as a transcriptional activator upon binding with RBP-J [26]. To determine if AVM formation in our model is mediated through canonical Notch signaling, we deleted *RBP-J* throughout the endothelium of postnatal mice prior to the onset of AV shunts. Notch4* and control mice were crossed with the RBP-J^{flox} [27] and *Cdh5-CreER* [ref] constructs and administered tamoxifen at P7 and P8 for Cre-mediated excision of *RBP-J* in Cdh5+ endothelial cells. Using this approach, we found that Notch4* mutants did not form AVMs by P18 when both alleles of *RBP-J* had been excised (43 image fields in 4 mice, **Figure 4A**) but still developed in Notch4* littermates that retained one endogenous *RBP-J* allele (20 fields in 3 mice, **Figure 4B**). Control animals did not exhibit noticeable cerebrovascular abnormalities upon excision of both *RBP-J* alleles (27 of fields in 5 mice**, Figure 4C**) or one *RBP-J* allele (23 fields in 4 mice**, Figure 4D**). Cre activity was verified in endothelium with the addition of the *mT/mG* reporter, allowing GFP expression upon Cre-mediated recombination in *Cdh5+* cells (**Figure 4A' to 4D'**). Taken together, these data suggest that the onset of AV shunts is mediated through the canonical signaling pathway in ECs of Notch4* mice. Additionally, we examined the survival in a subset of Notch4* animals with deletion of one or both *RBP-J* alleles, demonstrating improved survival in the latter group (**Figure 4E**).

Notch signaling in non-arterial vessels mediates AVM formation

Next, we directly examined whether Notch4* expression contributed to AVM formation through signaling in the arterial or non-arterial compartment. We employed two genetic approaches. First, we conditionally expressed Notch4* in arterial ECs under control of the *BMX-CreER$_2$;flox-stop-tTA* construct. BMX is a tyrosine kinase that is expressed in arterial endothelium, endocardium, and lymphatic vessels [28,29]. In brain, the *BMX-CreER$_2$* construct allows Cre-mediated recombination that is highly specific to arterial endothelium and is not detected in capillaries or veins (**Supplemental Figure 3**). We administered tamoxifen at P7 and P8 and examined the cerebral vessels at P18. *BMX-CreER;flox-stop-tTA;TRE-Notch4** animals demonstrated no AVMs or gross abnormalities in the cerebral vasculature (34 fields in 4 mice, **Figure 5A**). Conversely, *Cdh-CreER;flox-stop-tTA;TRE-Notch4** mice developed robust AVMs (33 fields in 3 mice, **Figure 2B**), indicating that arterial-specific expression of Notch4* did not cause brain AVMs.

Our second genetic approach was to test if blocking canonical Notch signaling in arterial ECs of Notch4* mice prevented AVM formation. *Tie2-tTA;TRE-Notch4** and control animals were crossed with the RBP-J^{flox} and *BMX-CreERT*$_2$ constructs and administered tamoxifen at P7 and P8 to allow Cre-mediated excision of *RBP-J* in arterial ECs. Notch4* mutants formed AVMs by P18 regardless of whether they were homozygous (34 fields in 4 mice, **Figure 6A**) or heterozygous (15 fields in 2 mice**, Figure 6B**) for the RBP-J^{flox} transgene. Control animals did not exhibit AVMs or noticeable cerebrovascular abnormalities when homozygous (28 fields and 5 mice, **Figure 6C**) or heterozygous (11 fields in 2 mice, **Figure 6D**) for the RBP-J^{flox} transgene. Cre activity was verified in arterial endothelium with the addition of *mT/mG* reporter, allowing GFP expression upon Cre-mediated recombination of *BMX+* cells (**Figure 6A' to 6D'**). Taken together, these results suggest that the formation of AVMs in Notch4* mice was mediated by Notch signaling in non-arterial endothelium. Interestingly, we also found that the *BMX-CreERT*$_2$;*mT/mG* construct labeled AVMs and veins upon administration of tamoxifen at P16 and P17 (**Supplemental Figure 4)**. This result is further evidence that Notch4* was not expressed in capillaries or veins upon induction with tamoxifen at P7 and P8, and suggests the possibility that *BMX* promoter activity is regulated by Notch4 signaling.

Discussions

To date, the etiology and developmental mechanisms of BAVM formation remains obscure. The favored model is that BAVMs are a result of failed remodeling from embryonic vasculature that persist as congenital lesions into adulthood [10]. This theory is based heavily on the morphological appearance of adult BAVMs due to lack of timelapse data on disease onset. We have previously reported that Notch4* expression in ECs leads to reprogramming of AV specification and the development of brain AVMs in neonatal life. Here, we use four-dimensional TPLSM to dynamically observe vascular remodeling in the young mouse brain and find that BAVMs can arise from the conversion of postnatal capillaries into high flow shunts. The initiation of these AV shunts involves an increase in capillary diameter that can precede elevated blood flow. Mechanistically, this transformation involves ectopic Notch signaling in non-arterial vessels and does not require Notch signaling in arteries.

De novo AVM formation

Our data support the theory of *de novo* AVM formation through enlargement of capillaries in the context of rapidly growing tissue. We previously found that Notch4* expression resulted in BAVMs during the neonatal period when the brain was rapidly growing, but not in postweaning mice [16]. Additionally, Notch4* expression in adult mice most greatly affected the liver, skin, and uterus – organs that continuously remodel though adult life [15].

Recent work in an alternate mouse model of AVM demonstrated that deletion of ALK1 with constitutive L1Cre resulted in robust brain, GI, and lung AVMs with lethality by P5 [30], supporting the hypothesis that growing tissues provide a permissive environment for AVM formation. Importantly, this study also found that postnatal deletion of ALK1 resulted in AVMs upon wounding in dermis, indicating that injury could provide necessary cues for the *de novo* formation of AVM in adult mice. In this setting, AVMs formed by active extension of arterial blood vessels that met growing venous branches and then enlarged. Although we did not observe AVMs developing from new connections in our Notch4* model, a compelling theory is that growing or healing tissues share common signaling elements that are permissive for enlargement of capillaries regardless of their origin.

Capillaries enlarge into AV shunts without mixing or extension of cells from the artery

Interestingly, recent work has demonstrated that dynamic 'cell-mixing' of ECs may contribute to angiogenic morphogenesis in a Notch-dependent fashion [31]. Using *in vivo* TPLSM*,* we observed that ECs can migrate within the walls of established vessels (**Supplemental Figure 5**). To further test whether active extension of arterial vessels might contribute to AVMs in our mouse model, we fluorescently labeled the arterial ECs using the *BMX-CreER;mT/mG* with tamoxifen induction at P1 and P2, and imaged the development of AVMs using *in vivo* TPLSM. AV shunts developed without the migration of ECs from the adjacent arteries (11/11 AVMs in 5 mice, **Figure 7**), further supporting the notion that AVMs can arise from the primary growth of capillaries.

Smooth muscle coverage is not required for the initial enlargement of capillaries

A common feature of human AVMs is increased vascular smooth muscle cell (SMC) coverage, which is speculated to be a result of AV shunting [32]. In our animal model, we observed enhanced smooth muscle coverage in AVMs and veins that was normalized upon suppression of Notch4* [21]. This phenotype led us to ask whether SMCs might directly contribute to the enlargement of capillaries into AV shunts. We examined early AV shunts in cerebral cortex at P12 by wholemount immunostaining with α–Smooth muscle actin (αSMA). Staining was visible in arteries and veins, but was often absent from small AVMs (**Figure 8**). These results suggest that SMCs do not play a direct role in the onset of AV shunts and further supports the notion that SMC coverage in AVMs is a consequence of shunting. Importantly, recent work has demonstrated that pericytes can directly regulate capillary constriction in retina and cerebellar slices [33], raising the possibility that pericyte dysfunction might contribute to the initial enlargement of capillaries in Notch4* mice. A detailed investigation of the interaction between endothelial Notch signaling and apposed pericytes through paracrine or cell-cell signaling may shed light on an important mechanism maintaining capillaries and preventing their enlargement into AV shunts.

We employed two-photon laser scanning microscopy and a neonatal cranial window for *in vivo* observation of vessels in the mouse brain and studied the formation of brain AVM over time. Using this approach, we demonstrate that AVMs may arise from capillaries during postnatal life upon endothelial expression of Notch4*. The onset of AV shunts involves an increase in capillary diameter that can precede elevated blood flow, suggesting that disruption of capillary caliber is the initiating pathology in the formation of AVMs. We have focused on brain, but our findings likely apply in other organs such as liver, uterus, skin, and lung where we have also identified AVMs in Notch4* mice [15]. Our data supports a model of *de novo* AVM formation in actively remodeling tissues. Our mouse model may also be used to shed light on the permissive conditions for AVM formation by investigating the molecular congruencies across these organs during periods of AVM development or quiescence.

Methods

In Vivo Imaging

Cranial windows for long-term imaging were performed as previously described [34,35,36,37] with modifications for immature mice [21,38]. In brief, one-week-old mice were anesthetized with 0.5-2% isoflurane in 2 L/min of oxygen and warmed with a homeothermic blanket (Harvard Apparatus). The scalp was treated with betadine and given subcutaneous injection of 0.125% bupivacaine prior to surgery. The head was immobilized for surgery and imaging by attaching a custom-milled metal bar to the cranium, allowing it to be secured to an adapter arm that was added to a stereotactic base (myNeuroLab.com**).** A small craniotomy was performed over the right cortex, bathed in artificial cerebral spinal fluid, covered with a 5 mm round coverslip (World Precision Instruments), and sealed in place with dental acrylic (Lang Dental) to provide optical access to the brain. Mice were administered with subcutaneous injections of 0.1 mg/kg buprenorphine pre-operatively and twice daily for three days.

The blood was fluorescently labeled for *in vivo* imaging with either 2000 KDa fluorescein-dextran (Sigma) or 2000 KDa Texas Red-dextran prepared according to a published protocol [39] and filtered with 1000 KDa dialysis tubing (Spectrum Labs). Low-energy femtosecond laser pulses were centered at 870 nm to simultaneously excite Texas Red-dextran and GFP, or at 800 nm to excite fluorescein-dextran. Line-scan data was typically recorded at 2.6 kHz along the central axis of vessels and analyzed for blood velocity using previously described methods [34,35,36,37]. Image and line-scan data were obtained using a locally constructed TPLSM. 100 fs, 80 MHz pulses were generated by a Titanium:Sapphire laser oscillator (Mai Tai HP; Newport Spectra-Physics) and passed through a dispersion compensator (DeepSee; Newport Spectra-Physics). Laser intensity was controlled by rotating a $\lambda/2$ wave-plate relative to a polarizing splitter, and the attenuated beam was directed onto the microscope platform. The laser pulses were raster-scanned by galvonometric mirrors and relay-imaged to the back aperture of a long working distance 1.0 NA water-immersion objective (Zeiss). Two-photon excited fluorescence was collected by the same objective, reflected by a dichroic mirror (700 nm long pass), split into red or green channels by a second dichroic mirror (560 nm long pass), spectrally cleaned with additional band-pass filters (Chroma), and relayed to photomultiplier tubes (PMT; H7422P-40MOD; Hammamatsu). A three-dimensional translation stage (11SI70521 Rev. 01; Newport) allowed precise positioning of the mouse relative to the focus of the microscope. MPScan 1.0 software was used to control the microscope and record image data [40].

Mice

This study was carried out in strict accordance with NIH regulations and the Institutional Animal Care and Use Committee at the University of California San Francisco. The protocol was approved by the IACUC at UCSF (Approval Number: AN085404-01). *Tie2-tTA*, *TRE-Notch4**, and *Tie2-Cre* mice were generated by our lab as previously described [15,41]. For *Tie2-tTA; TRE-Notch4** breedings, Tetracycline sucrose water (0.5 mg/mL Tetracycline hydrochloride, Sigma, and 50 mg/mL D-sucrose, Fisher BioReagents) was administered to pregnant mothers and withdrawn when pups were born to allow expression of Notch4* in endothelial cells. In a subset of experiments, mice were given intraperitoneal injection of doxycycline (0.5 mg in 500mL of phosphate-buffered saline) and fed doxycycline diet (Bio-Serv) to repress Notch4* expression later in life. *Ephrin-B2*$^{+/H2B\text{-}eGFP}$ mice [42] were kindly provided by the Soriano lab and aided with *in vivo* visualization with arterial specification of endothelium over time. The *ephrin-B2*$^{+/tau\text{-}LacZ}$ [7], *EphB4*$^{+/tau\text{-}LacZ}$ [8], *Notch1*$^{+/tau\text{-}LacZ}$ [reference], *Coup-TFII*$^{+/fl\text{-}stop\text{-}nLacZ}$ [43] reporter lines were used to visualize the arteriovenous specification of blood vessels by X-gal staining. The *TRE-H2B-eGFP* [24] fluorescent reporter was used to label endothelial nuclei and examine *Tie2-tTA*-mediated gene expression by *in vivo* TPLSM. Cre-recombinase was temporally regulated in endothelium using *Cdh5-CreERT*$_2$ [44] or in arterial endothelium using *BMX-CreERT*$_2$ mice, both kindly provided by the Adams lab. These *CreERT*$_2$ lines were used to fluorescently label ECs with *mT/mG* [45], activate the tetracycline regulatable system in flox-stop-tTA mice [46] or abrogate Notch signaling with the RBP-J$^{flox/flox}$ constructs [27].

Induction of Cre-mediated Recombination

Tamoxifen solution was prepared at 20 mg/mL in corn oil and administered according to published methods [44] with minor modifications. Three different regimens of tamoxifen were utilized to activate Cre-mediated recombination for AVM formation or regression experiments. For peri-natal induction, newborn pups were given 0.2 mg of tamoxifen by intragastric injection at P1 and P2. For induction closely preceding AV shunt formation, pups were given 0.5 mg of tamoxifen by intragastric injection at P7 and P8. For induction after the development of AVMs, juvenile mice were given 1 mg of tamoxifen by intraperitoneal injection at P17 and P18. All littermates were treated with the same dose of tamoxifen to generate appropriate experimental controls.

Gamma Secretase Inhibitor Treatment

DAPT (N-[N-(3,5-Difluorophenacetyl-L-alanyl)]-Sphenylglycine t-Butyl Ester, Sigma) was prepared and administered according to published methods [47]. In brief, 100 mg/kg DAPT was dissolved in 10% ethanol and 90% corn oil. Mice were administered DAPT or vehicle daily by intraperitoneal injection at a volume of 10 μL/g.

X-galactosidase/3,3-diaminobenzidine Staining

25 μg of biotinylated L. esculentum-lectin (Vector Labs) was injected via the inferior vena cava and allowed to circulate for 2 minutes in anesthetized mice. Animals were then perfused transcardially with PBS followed by LacZ fixative (0.25% glutaraldehyde, 50 mM EGTA, 100

mM $MgCl_2$ in PBS). Brains were harvested and briefly bathed in LacZ fixative. The cortex was removed and stained for β-galactosidase at room temperature according to published protocol [48]. The cortex was then fixed with 1% PFA, blocked (10% BSA and 0.1% Triton X-100 in PBS), and incubated with 1:1000 streptavidin-conjugated horseradish peroxidase (Jackson ImmunoResearch) in block overnight. Specimens were washed for several hours and then stained with DAB kit (3,3-diaminobenzidine, Vector Labs).

Immunostaining

25 μg of biotinylated L. esculentum-lectin (Vector Labs) was mixed with Cy5-streptavidin conjugated (Jackson ImmunoResearch) and injected into the inferior vena cava and allowed to circulate for 2 minutes in anesthetized mice. Animals were perfused transcardially with PBS and then with 1% paraformaldehyde (PFA). The brains were harvested and fixed briefly in 1% PFA. For wholemount staining, tissue was blocked (2% bovine serum albumin, 0.1% Triton X-100 in PBS) and incubated with anti-VE-cadherin (BD Pharmingen, clone 11d4.1, 1:200 dilution) and anti-α-smooth muscle actin (Sigma, clone 1A4, 1:200 dilution) antibodies overnight in block. Notch4-ICD staining in sections was conducted according to published protocol [16]. In brief, harvested brains were fixed in 1% PFA overnight. Brains were bisected along the longitudinal fissure, dehydrated in 30% sucrose in PBS overnight, and embedded in optimal cutting temperature compound (OCT) for frozen sectioning. The brains were cut in 10 μm sagittal sections, blocked (3% donkey serum, 2% BSA, 0.2% Triton X-100 in PBS), incubated with anti-Notch4-ICD antibody (Millipore, formerly Upstate, 1:2000 dilution) or non-specific rabbit IgG (Santa Cruz Biotechnology, 1:800) in block, washed, incubated with Cy3-donkey-ant-irabbit antibody (Jackson ImmunoResearch, 1:1000), washed, and mounted in VectaShield with DAPI (Vector Labs).

Fluorescence Quantification of Notch4-ICD Staining and TRE-H2B-GFP Expression

Quantification of immunofluorescence was conducted according to published protocol [18]. In brief, *Tie2-tTA; TRE-Notch4*; TRE-H2B-GFP* brain specimens were harvested at P10, P12, and P18 to correspond with various stages of AV development. Specimens were stained with Notch4-ICD antibody (see Immunostaining) and imaged using a 20x objective on a Zeiss Axiovert fluorescent microscope (Thornwood, NY, USA) with Intelligent Imaging software (Denver, CO, USA). Identical exposure time was used for all slides and individual fluorescent channel intensities were exported as 16-bit TIFF files. Using ImageJ, a blinded examiner circumscribed DAPI-labeled nuclei that were double-positive for perfusion-labeling by L. esculentum-lectin with Cy5-streptavidin**.** Intensities of Notch4-ICD or IgG staining, and TRE-H2B-GFP were quantified in the enclosed area for each nucleus. Notch4-ICD intensities in mutant mice was normalized to controls that were stained and imaged within the same experimental session. TRE-H2B-GFP intensities were normalized to background levels in neighboring, non-endothelial nuclei within the same slide.

RNA Probe Preparation

Mouse Rbp-J DNA (provided by C Cepko, Harvard Medical School) was amplified from plasmid using T3/T7 PCR (56°C annealing). DNA template was recovered using gel extraction (QIAGEN), and in vitro transcription produced digoxigenin-labeled, single-stranded RNA probe.

Whole mount In Situ hybridization

In situ hybridization was performed as described by Hunter et al., 2005, with modifications [49]. Following transcardial perfusion with saline and 4% paraformaldehyde, whole brains were harvested and immersion fixed in 4% paraformaldehyde overnight at 4°C. Cerebral cortex was removed and used in subsequent steps. Tissue was dehydrated through 5 min methanol series (25, 50, 75, 100%) and stored in 100% methanol at -20°C. Pre-hybridization, tissue was rehydrated through reverse methanol series, rinsed in PBS, treated with 6% hydrogen peroxide in PBS 1 hr, rinsed in PBS, incubated with 10ug/mL proteinase K 30 min, washed with 2mg/mL glycine 10 min, rinsed in PBT (PBS + 1% Tween-20), fixed in 0.2% gluteraldehyde/4% paraformaldehyde in PBT 20 min, rinsed in PBT, incubated in hybridization buffer (50% formamide, 5X SSC pH4.5, 50ug/mL yeast tRNA (Invitrogen), 1% SDS, 50ug/mL heparin). For hybridization, digoxigenin-labeled RNA probe was heated to 95°C 5min. Tissue was incubated in fresh hybridization buffer containing 1mg/mL riboprobe 70°C overnight. Post-hybridization, tissue was washed as follows: solution 1 (50% formamide, 5X SSC pH4.5, 1% SDS) 2X 30min 65°C; equal parts solution 1:solution 2 (0.5M NaCl, 10mM Tris pH7.5, 0.1% Tween-20) 10min room temperature (RT); solution 2 3X 5min RT; 25ug/mL RNase A (Sigma-Aldrich) in solution 2 1hr 37°C; solution 2 5min 65°C; solution 3 (50% formamide, 2X SSC pH4.5) 5min 65°C; solution 3 2X 30min 65°C; TBST (0.14M NaCl, 2.7mM KCl, 25mM Tris pH7.5, 1% Tween-20) 3X 5 min RT. Tissue was incubated in Roche Blocking Reagent (prepared per manufacturer's instructions) with 2mM levamisole (Sigma-Aldrich) 1hr RT. Anti-digoxigenin-alkaline phosphatase (Roche) was applied 1:1000 in blocking solution with 2mM levamisole 4°C overnight. Tissue was washed in TBST 3X 5min and 5X 1hr RT. Tissue was rinsed in staining buffer 100mM NaCl, 100mM Tris pH9.5, 50mM $MgCl_2$, 1% Tween-20) 3X 10min at RT. For transcript detection, tissue was incubated with 4.5uL NBT (Roche)/3.5uL BCIP (Roche) per 1mL of staining buffer in the dark at RT. Post-detection, tissue was rinsed 3X 5min in PBS containing 20mM EDTA and post-fixed in 4% paraformaldehyde.

REFERENCES

1. Morgan M, Winder M (2001) Haemodynamics of arteriovenous malformations of the brain and consequences of resection: a review. Journal of clinical neuroscience : official journal of the Neurosurgical Society of Australasia 8: 216-224.
2. Corti P, Young S, Chen CY, Patrick MJ, Rochon ER, et al. (2011) Interaction between alk1 and blood flow in the development of arteriovenous malformations. Development 138: 1573-1582.
3. Murray CD (1926) The Physiological Principle of Minimum Work Applied to the Angle of Branching of Arteries. The Journal of general physiology 9: 835-841.
4. Murray CD (1926) The Physiological Principle of Minimum Work: I. The Vascular System and the Cost of Blood Volume. Proceedings of the National Academy of Sciences of the United States of America 12: 207-214.
5. Girard H (1973) Arterial pressure in the chick embryo. The American journal of physiology 224: 454-460.
6. Gonzalez-Crussi F (1971) Vasculogenesis in the chick embryo. An ultrastructural study. The American journal of anatomy 130: 441-460.
7. Wang HU, Chen ZF, Anderson DJ (1998) Molecular distinction and angiogenic interaction between embryonic arteries and veins revealed by ephrin-B2 and its receptor Eph-B4. Cell 93: 741-753.
8. Gerety SS, Wang HU, Chen ZF, Anderson DJ (1999) Symmetrical mutant phenotypes of the receptor EphB4 and its specific transmembrane ligand ephrin-B2 in cardiovascular development. Molecular cell 4: 403-414.
9. Braverman IM, Keh A, Jacobson BS (1990) Ultrastructure and three-dimensional organization of the telangiectases of hereditary hemorrhagic telangiectasia. The Journal of investigative dermatology 95: 422-427.
10. Mullan S, Mojtahedi S, Johnson DL, Macdonald RL (1996) Embryological basis of some aspects of cerebral vascular fistulas and malformations. Journal of neurosurgery 85: 1-8.
11. Friedlander RM (2007) Clinical practice. Arteriovenous malformations of the brain. The New England journal of medicine 356: 2704-2712.
12. Krebs LT, Shutter JR, Tanigaki K, Honjo T, Stark KL, et al. (2004) Haploinsufficient lethality and formation of arteriovenous malformations in Notch pathway mutants. Genes & development 18: 2469-2473.
13. Lawson ND, Scheer N, Pham VN, Kim CH, Chitnis AB, et al. (2001) Notch signaling is required for arterial-venous differentiation during embryonic vascular development. Development 128: 3675-3683.
14. Krebs LT, Starling C, Chervonsky AV, Gridley T (2010) Notch1 activation in mice causes arteriovenous malformations phenocopied by ephrinB2 and EphB4 mutants. Genesis 48: 146-150.
15. Carlson TR, Yan Y, Wu X, Lam MT, Tang GL, et al. (2005) Endothelial expression of constitutively active Notch4 elicits reversible arteriovenous malformations in adult mice. Proc Natl Acad Sci U S A 102: 9884-9889.
16. Murphy PA, Lam MT, Wu X, Kim TN, Vartanian SM, et al. (2008) Endothelial Notch4 signaling induces hallmarks of brain arteriovenous malformations in mice. Proceedings of the National Academy of Sciences of the United States of America 105: 10901-10906.
17. ZhuGe Q, Zhong M, Zheng W, Yang GY, Mao X, et al. (2009) Notch-1 signalling is activated in brain arteriovenous malformations in humans. Brain : a journal of neurology 132: 3231-3241.
18. Murphy PA, Lu G, Shiah S, Bollen AW, Wang RA (2009) Endothelial Notch signaling is upregulated in human brain arteriovenous malformations and a mouse model of the

disease. Laboratory investigation; a journal of technical methods and pathology 89: 971-982.

19. Nichols SA, Dirks W, Pearse JS, King N (2006) Early evolution of animal cell signaling and adhesion genes. Proceedings of the National Academy of Sciences of the United States of America 103: 12451-12456.
20. King N, Westbrook MJ, Young SL, Kuo A, Abedin M, et al. (2008) The genome of the choanoflagellate Monosiga brevicollis and the origin of metazoans. Nature 451: 783-788.
21. Murphy PA, Kim TN, Lu G, Bollen AW, Schaffer CB, et al. (2012) Notch4 normalization reduces blood vessel size in arteriovenous malformations. Science translational medicine 4: 117ra118.
22. Murphy PA, Lam MT, Wu X, Kim TN, Vartanian SM, et al. (2008) Endothelial Notch4 signaling induces hallmarks of brain arteriovenous malformations in mice. Proc Natl Acad Sci U S A 105: 10901-10906.
23. Murphy PA, Lu G, Shiah S, Bollen AW, Wang RA (2009) Endothelial Notch signaling is upregulated in human brain arteriovenous malformations and a mouse model of the disease. Lab Invest 89: 971-982.
24. Tumbar T, Guasch G, Greco V, Blanpain C, Lowry WE, et al. (2004) Defining the epithelial stem cell niche in skin. Science 303: 359-363.
25. Kato H, Sakai T, Tamura K, Minoguchi S, Shirayoshi Y, et al. (1996) Functional conservation of mouse Notch receptor family members. FEBS letters 395: 221-224.
26. Tamura K, Taniguchi Y, Minoguchi S, Sakai T, Tun T, et al. (1995) Physical interaction between a novel domain of the receptor Notch and the transcription factor RBP-J kappa/Su(H). Current biology : CB 5: 1416-1423.
27. Tanigaki K, Han H, Yamamoto N, Tashiro K, Ikegawa M, et al. (2002) Notch-RBP-J signaling is involved in cell fate determination of marginal zone B cells. Nature immunology 3: 443-450.
28. Ekman N, Lymboussaki A, Vastrik I, Sarvas K, Kaipainen A, et al. (1997) Bmx tyrosine kinase is specifically expressed in the endocardium and the endothelium of large arteries. Circulation 96: 1729-1732.
29. Rajantie I, Ekman N, Iljin K, Arighi E, Gunji Y, et al. (2001) Bmx tyrosine kinase has a redundant function downstream of angiopoietin and vascular endothelial growth factor receptors in arterial endothelium. Molecular and cellular biology 21: 4647-4655.
30. Park SO, Wankhede M, Lee YJ, Choi EJ, Fliess N, et al. (2009) Real-time imaging of de novo arteriovenous malformation in a mouse model of hereditary hemorrhagic telangiectasia. The Journal of clinical investigation 119: 3487-3496.
31. Arima S, Nishiyama K, Ko T, Arima Y, Hakozaki Y, et al. (2011) Angiogenic morphogenesis driven by dynamic and heterogeneous collective endothelial cell movement. Development 138: 4763-4776.
32. Sho E, Nanjo H, Sho M, Kobayashi M, Komatsu M, et al. (2004) Arterial enlargement, tortuosity, and intimal thickening in response to sequential exposure to high and low wall shear stress. Journal of vascular surgery : official publication, the Society for Vascular Surgery [and] International Society for Cardiovascular Surgery, North American Chapter 39: 601-612.
33. Peppiatt CM, Howarth C, Mobbs P, Attwell D (2006) Bidirectional control of CNS capillary diameter by pericytes. Nature 443: 700-704.
34. Kleinfeld D, Denk W (2000) Two-photon imaging of neocortical micro-circulation. In: Yuste R, Lanni F, Konnerth A, editors Imaging neurons: A laboratory manual Cold Spring Harbor (New York) Cold Spring Harbor Laboratory Press 231-2315.
35. Schaffer CB, Friedman B, Nishimura N, Schroeder LF, Tsai PS, et al. (2006) Two-photon imaging of cortical surface microvessels reveals a robust redistribution in blood flow after vascular occlusion. PLoS biology 4: e22.

36. Holtmaat A, Bonhoeffer T, Chow DK, Chuckowree J, De Paola V, et al. (2009) Long-term, high-resolution imaging in the mouse neocortex through a chronic cranial window. Nature protocols 4: 1128-1144.
37. Shih AY, Driscoll JD, Drew PJ, Nishimura N, Schaffer CB, et al. (2012) Two-photon microscopy as a tool to study blood flow and neurovascular coupling in the rodent brain. Journal of cerebral blood flow and metabolism : official journal of the International Society of Cerebral Blood Flow and Metabolism.
38. Portera-Cailliau C, Weimer RM, De Paola V, Caroni P, Svoboda K (2005) Diverse modes of axon elaboration in the developing neocortex. PLoS biology 3: e272.
39. Hornig S, Christoph B, Gafe A, Wotschadlo J, Liebert T, et al. (2008) Biocompatible fluorescent nanoparticles for pH-sensoring. Soft Matter 4: 1169-1172.
40. Nguyen QT, Tsai PS, Kleinfeld D (2006) MPScope: a versatile software suite for multiphoton microscopy. Journal of neuroscience methods 156: 351-359.
41. Kim YH, Hu H, Guevara-Gallardo S, Lam MT, Fong SY, et al. (2008) Artery and vein size is balanced by Notch and ephrin B2/EphB4 during angiogenesis. Development 135: 3755-3764.
42. Davy A, Bush JO, Soriano P (2006) Inhibition of gap junction communication at ectopic Eph/ephrin boundaries underlies craniofrontonasal syndrome. PLoS Biol 4: e315.
43. Takamoto N, You LR, Moses K, Chiang C, Zimmer WE, et al. (2005) COUP-TFII is essential for radial and anteroposterior patterning of the stomach. Development 132: 2179-2189.
44. Pitulescu ME, Schmidt I, Benedito R, Adams RH (2010) Inducible gene targeting in the neonatal vasculature and analysis of retinal angiogenesis in mice. Nature protocols 5: 1518-1534.
45. Muzumdar MD, Tasic B, Miyamichi K, Li L, Luo L (2007) A global double-fluorescent Cre reporter mouse. Genesis 45: 593-605.
46. Wang L, Sharma K, Deng HX, Siddique T, Grisotti G, et al. (2008) Restricted expression of mutant SOD1 in spinal motor neurons and interneurons induces motor neuron pathology. Neurobiology of disease 29: 400-408.
47. Suchting S, Freitas C, le Noble F, Benedito R, Breant C, et al. (2007) The Notch ligand Delta-like 4 negatively regulates endothelial tip cell formation and vessel branching. Proceedings of the National Academy of Sciences of the United States of America 104: 3225-3230.
48. Carpenter B, Lin Y, Stoll S, Raffai RL, McCuskey R, et al. (2005) VEGF is crucial for the hepatic vascular development required for lipoprotein uptake. Development 132: 3293-3303.
49. Hunter NL, Awatramani RB, Farley FW, Dymecki SM (2005) Ligand-activated Flpe for temporally regulated gene modifications. Genesis 41: 99-109.

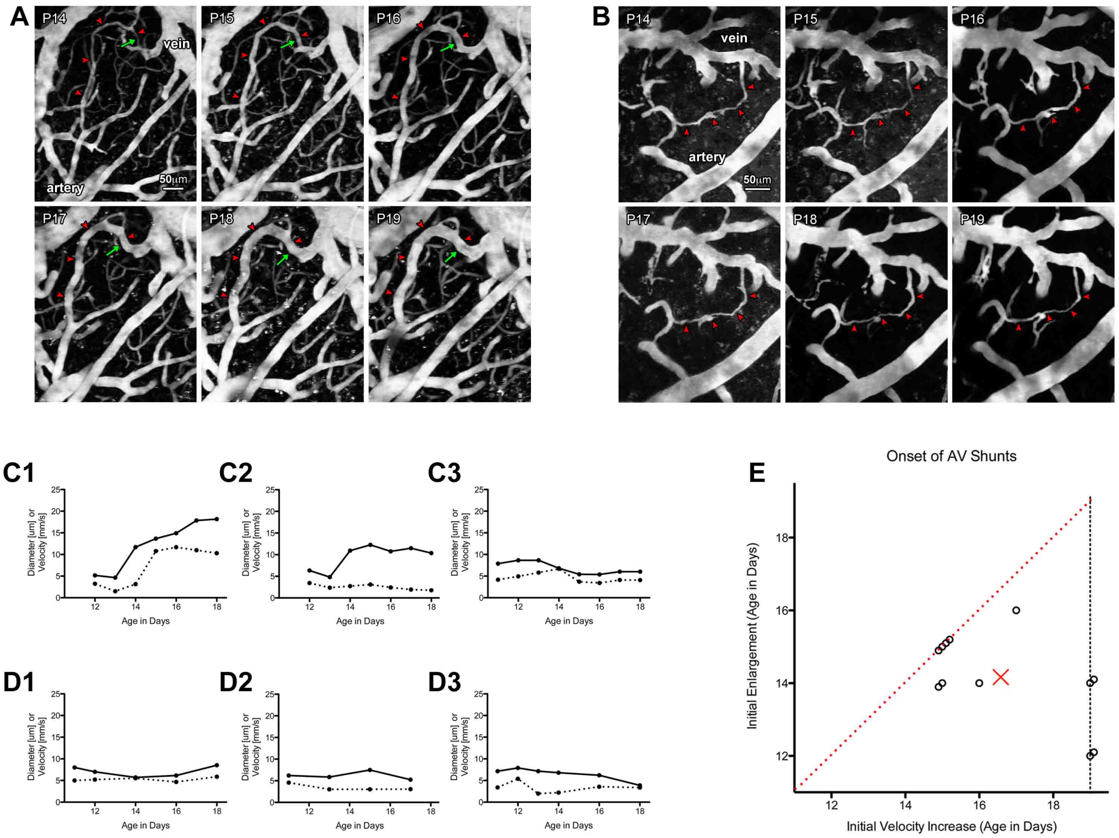

Figure 1. _Notch4*_-mediated AVMs arise from the primary enlargement of capillary-like vessels. A) Two-photon time-lapse imaging of a developing AV shunt in a _Notch4*_ mouse from post-natal day P14 to P19 where the plasma was labeled by intravenous injection of fluorescein-dextran. The complete artery-to-vein connection progressively enlarged over several days and is indicated by red arrowheads. Note the pronounced growth of the capillary-like vessel over time (green arrows). B) Two-photon time-lapse imaging of a capillary in a control mouse from P14 to P19. Red arrowheads indicate the complete artery-to-vein connection. C1-3) Representative plots of blood velocities (dotted line) and lumen diameters (solid line) of capillary-like vessels in Notch4* mice. C1) Example of coupled increase in lumen diameter and blood velocity. Note that the initial increase in lumen diameter precedes velocity by one day. C2) Example of initial increase in vessel diameter without increase in blood velocity over the recorded period. C3) Example of a capillary-like vessel that did not exhibit abnormal increase in lumen diameter or blood velocities over the recorded period. D1-3) Representative plots demonstrating normal variation of lumen diameter and blood velocity in control mice. E) Visual depiction of time of initial increase in velocity and lumen diameter per AV shunt. The dotted red line represents values with simultaneous increase in diameter and velocity. All capillary-like vessels were detected to enlarged either before or on the same day as increase in velocity. Data was acquired with per day temporal resolution. Adjacent data points represent overlapping values at the nearest whole number. Data points on the dotted black line represent capillary-like vessels that enlarged but did not exhibit a significant increase in velocity by the final day of imaging (P19).

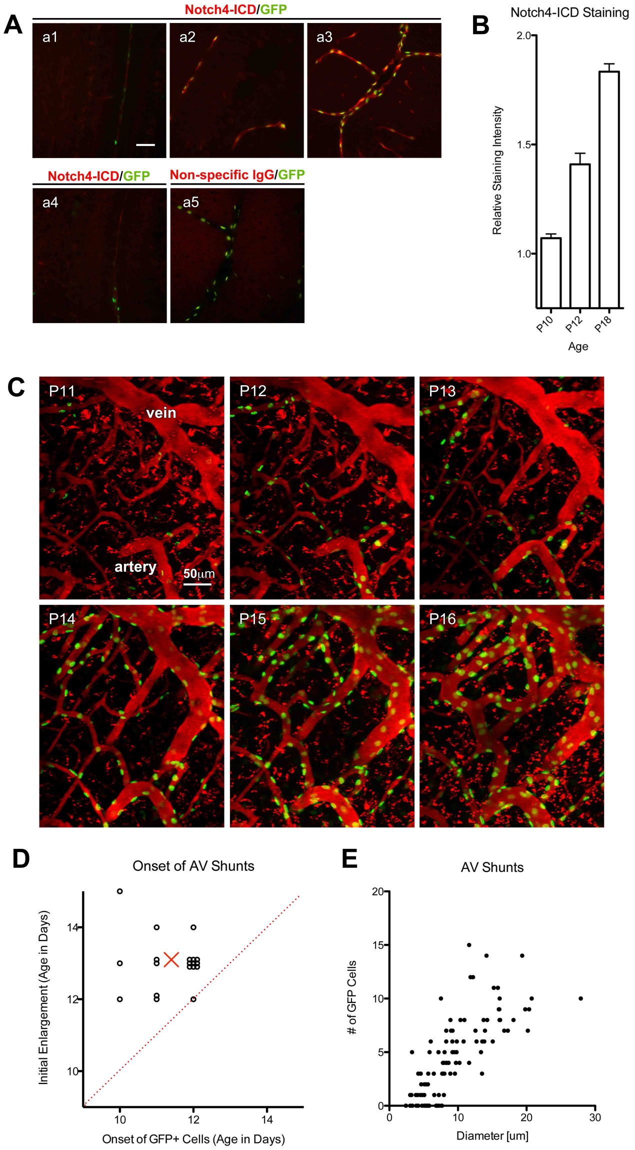

Figure 2. Notch4 expression increases in postnatal brain prior to enlargement of AV shunts. A) Notch4-ICD staining in sagittal brain sections of *Tie2-tTA/TRE-Notch4*/TRE-H2B-GFP* mice at P10 (a1), P12 (a2), and P18 (a3). (a3) Notch4-ICD staining in littermate control. (a4) Negative control of Notch4 staining using non-specific IgG on adjacent section in mutant specimen. B) Notch4-ICD staining intensities of mutant mice normalized to staining in age-matched controls. C) Two-photon time-lapse imaging of an artery-to-vein connection in a *Tie2-tTA/Notch4*/TRE-GFP* mutant mouse from post-natal day P11 to P16 where the plasma is labeled by intravenous injection of TexasRed-dextran. Note the initial detection of GFP+ cells in the artery-to-vein connection on P12 and P13, prior to enlargement of the AV shunt at P14. The AV shunt progressively enlarged from P14 to P16 with increase in GFP+ cells number. D) Correlation between the time of initial detection of GFP+ cells and initial increase of diameter per capillary-like vessel. The dotted red line represents simultaneous increase in diameter and detection of GFP+ cells. GFP was detected prior to enlargement in the majority of vessels (18/19 capillary-like connections in 5 mice) or on the same day (1/19 capillary-like connections). All data was acquired with per day temporal resolution. Grouped data points represent overlapping values at the nearest whole number. E) Correlation between the diameter and number of GFP+ cells in capillary-vessels that enlarged into AV shunts (Pearson r = 0.7713, P value < 0.0001).

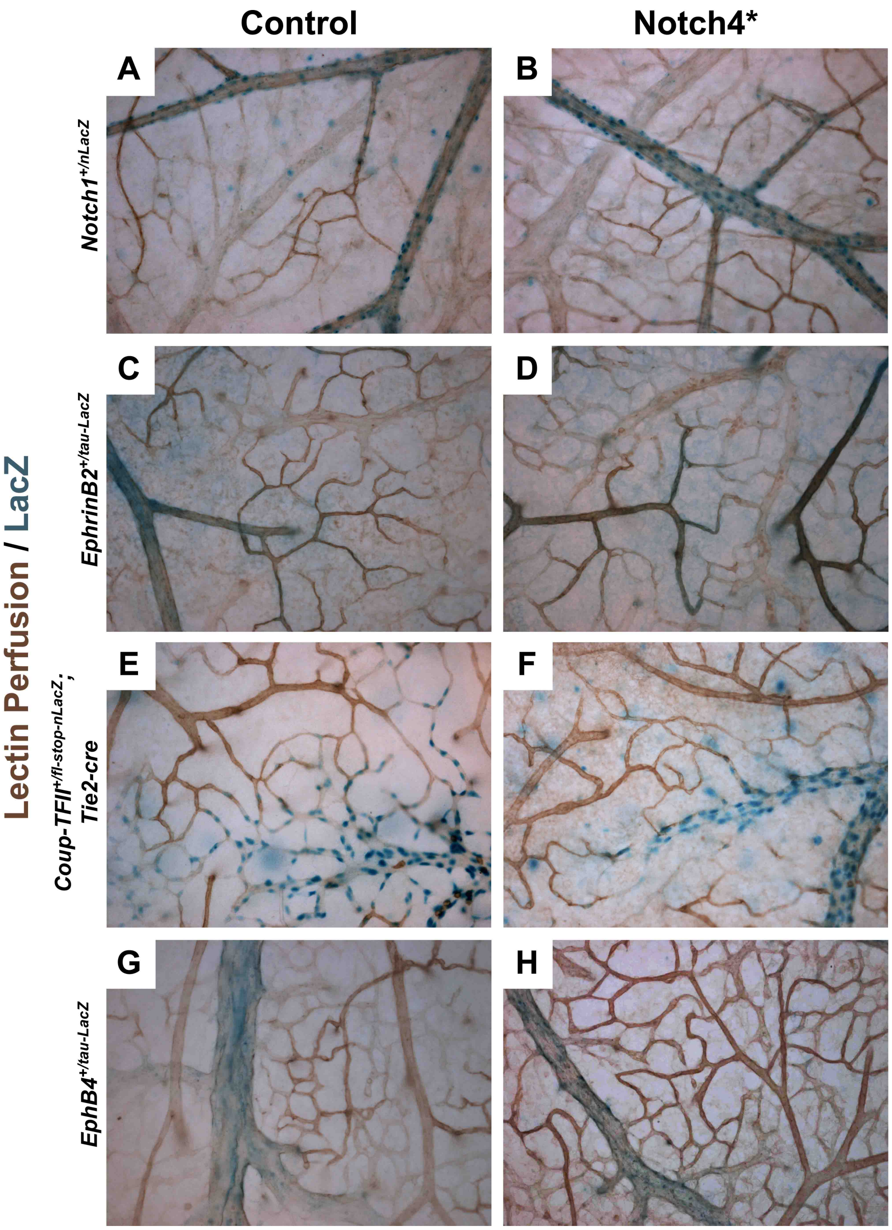

Figure 3. Arteriovenous specification appears normal in *Notch4 mice shortly before the onset of AV shunts.** Wholemount lacZ staining of the surface vasculature of the cerebral cortex demonstrating expression patterns of arterial and venous markers at postnatal day 10. Vessels were perfused with horseradish peroxidase-bound lycopersicon esculentum lectin, and counterstained by 3,3'-diaminobenzidine reaction. A and B) Notch1$^{+/nlacZ}$ reporter in control and Notch4* mice at P10. In both control (A) and mutant (B) animals, LacZ staining demonstrating nuclear labeling of arteries but not capillaries or veins. C and D) ephrin-B2$^{+/tau\text{-}lacZ}$ reporter in control and Notch4* mice at P10. LacZ staining labeled arteries and not veins in both control (C) and mutant (D) animals. E and F) Coup-TFII$^{+/fl\text{-}stop/nlacZ}$; Tie2-Cre labeling in control and Notch4* mice at P10. In both control (E) and mutant (F) animals, LacZ staining demonstrating nuclear labeling in veins and capillaries, but not arteries. G and H) EphB4$^{+/tau\text{-}lacZ}$ reporter in control and Notch4* mice at P10. In both control (G) and mutant (H) animals, LacZ staining demonstrating labeling in veins and not arteries without presence of AV shunts.

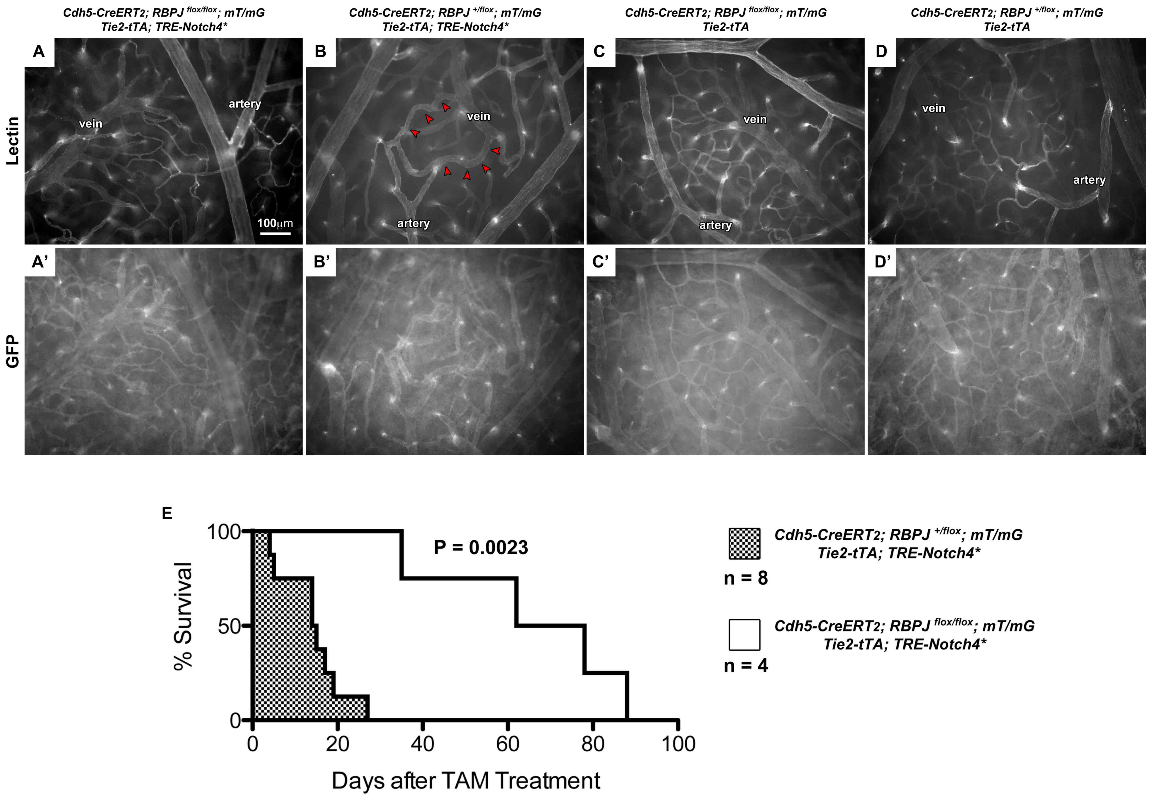

Figure 4. Endothelial deletion of *RBP-J* inhibits the formation of Notch4* mediated AVMs. Imaging of cortical vasculature in mice perfused at P18 with Cy5-conjugated Lycopersicon esculentum lectin. Animals were administered with Tamoxifen at P7 and P8 to allow post-natal excision of *RBP-J* in ECs by *Cdh5-CreERT*$_2$ prior to the onset of AV shunts. A) Notch4* mice homozygous for floxed-*RBP-J* alleles did not exhibit AVMs by P18 (43 fields in 4 mice). B) Notch4* mice heterozygous for the floxed-*RBP-J* allele developed AVMs by P18 (20 fields in 3 mice). Control mice homozygous for floxed-*RBP-J* alleles did not exhibit AVMs or gross cerebrovascular abnormalities (27 fields and 5 mice). D) Control mice heterozygous for the floxed-*RBP-J* allele did not exhibit AVMs or gross cerebrovascular abnormalities (23 fields in 4 mice). A'-D') *Cdh5-CreERT*$_2$ activity was visualized in ECs using the flox-STOP-mGFP construct from the *mT/mG* reporter. E) Kaplan-Meier survival curve showing that homozygous deletion of *RBP-J* in *Cdh5+* endothelium improved survival in Notch4* mice compared with heterozygous *RBP-J* deletion.

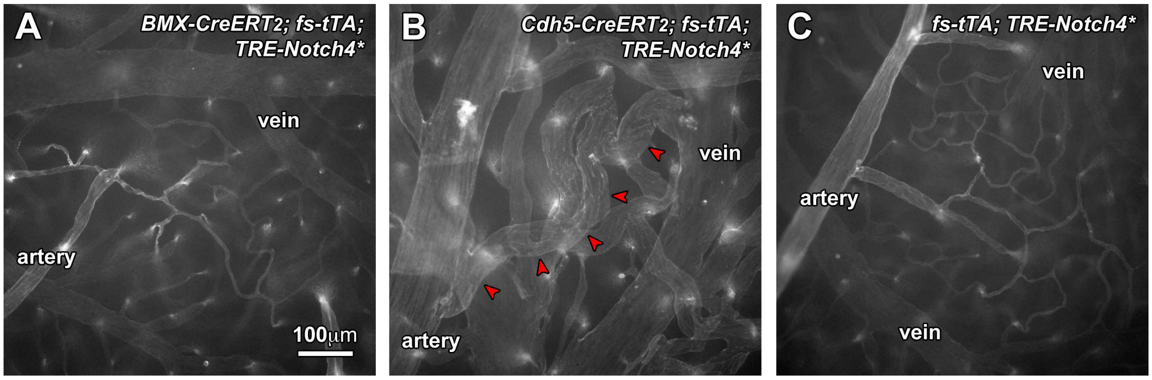

Figure 5. Notch4* expression in arterial endothelium does not lead to AV shunt formation. Imaging of cortical vasculature of *flox-stop-tTA;Notch4** mice perfused with Cy5-conjugated Lycopersicon esculentum lectin. Importantly, these animals contained the *flox-stop-tTA* instead of the *Tie2-tTA* element to regulate Notch4* expression. Animals were administered with Tamoxifen at P7 and P8 to allow expression of Notch4* under control Cre-mediated activation of *flox-stop-tTA.* A) *BMX-CreER;flox-stop-tTA;TRE-Notch4** did not demonstrate AVMs or gross abnormalities in the cerebral vasculature at P18 (34 fields in 4 mice). B) *Cdh5-CreER;flox-stop-tTA;TRE-Notch4** mice all developed robust AVMs indicated by the red arrowheads (33 fields in 3 mice). C) Control mice containing the *flox-stop-tTA;Notch4* construct, without Cre-recombinase, did not exhibit vascular abnormalities (41 fields in 5 mice).

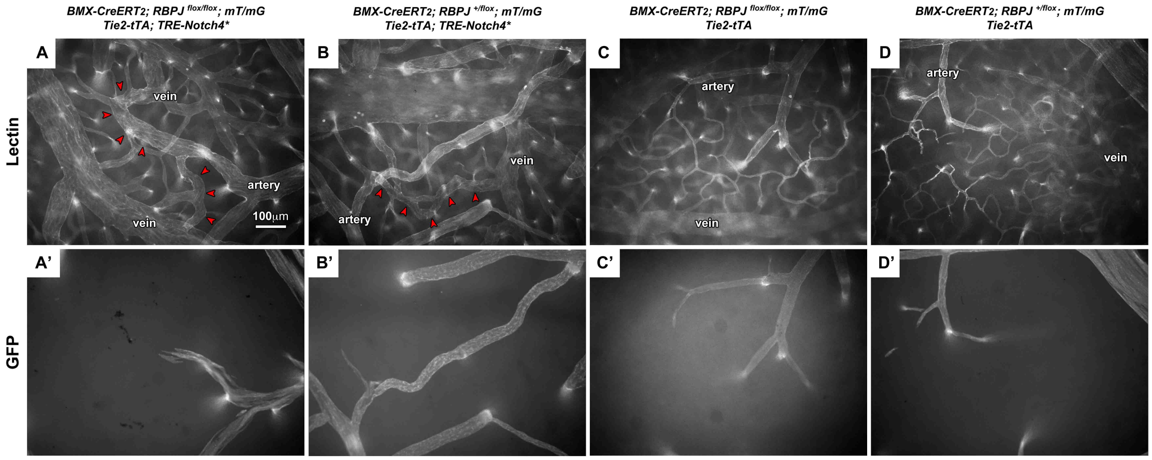

Figure 6. Deletion of *RBP-J* in arterial ECs does not inhibit formation of Notch4* mediated AVMs. Imaging of cortical vasculature in mice perfused at P18 with Cy5-conjugated Lycopersicon esculentum lectin. Animals were administered with tamoxifen at P7 and P8 to allow post-natal excision of *RBP-J* in arterial ECs by *BMX-CreERT$_2$* prior to the onset of AV shunts. A) Notch4* mice homozygous for floxed-*RBP-J* developed AVMs by P18 (34 fields in 4 mice). B) Notch4* mice heterozygous for the floxed-*RBP-J* allele developed AVMs by P18 (15 fields in 2 mice). Control mice homozygous for floxed-*RBP-J* alleles did not exhibit AVMs or gross cerebrovascular abnormalities (28 fields and 5 mice). D) Control mice heterozygous for the floxed-*RBP-J* allele did not exhibit AVMs or gross cerebrovascular abnormalities (11 fields in 2 mice). A'-D') *BMX-CreERT$_2$* activity was visualized in arterial ECs using the flox-STOP-mGFP construct from the *mT/mG* reporter.

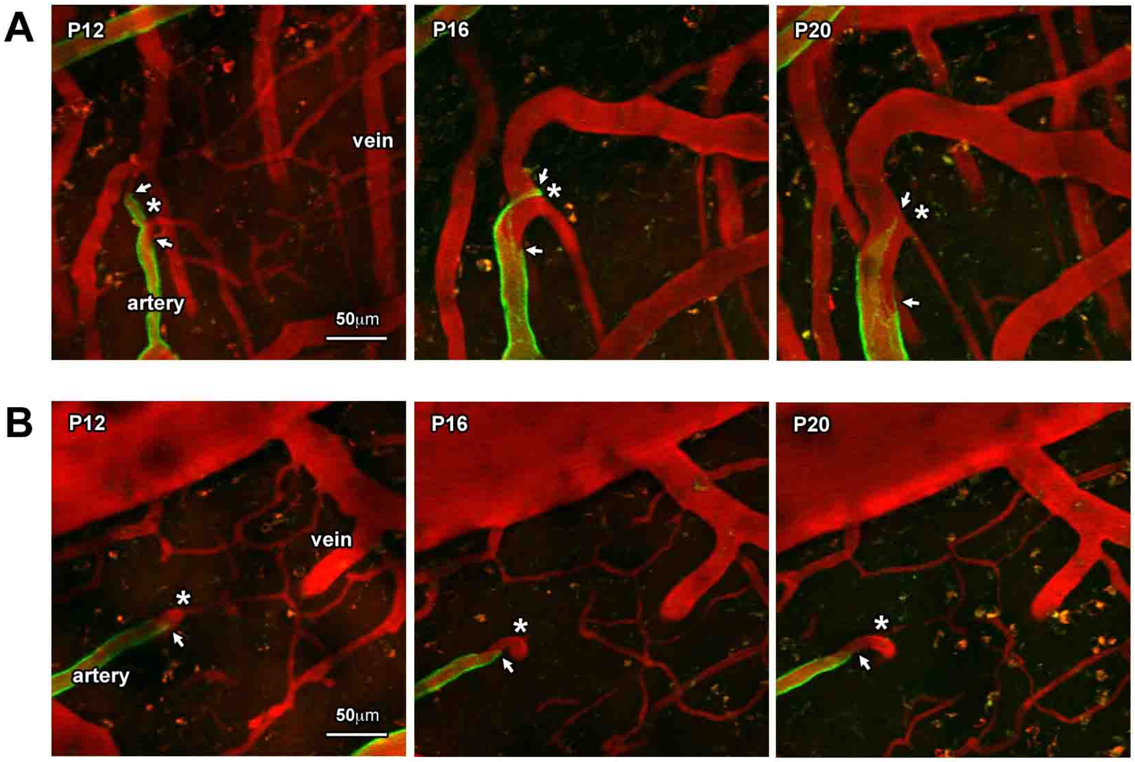

Figure 7. AVMs in Notch4* mice develop from capillaries without mixing or extension of ECs from the arteries. A) Two-photon time-lapse imaging of an enlarging AVM in *Notch4** mouse. Fluorescent contrast of perfused vessels was provided by intravenous injection of Texas Red-dextran. GFP expression was induced in arterial ECs prior to upregulation of Notch4* by administering Tamoxifen early at P1 and P2, allowing the cells at the arteriole-capillary boundary to be tracked over time. The (*) indicates the same vessel bifurcation over time and white arrows denote the edges of the GFP+ boundary. Imaging from P12 to P20 revealed that ECs from the artery did not migrate into the enlarging capillary and moved in the opposite direction past the proximal vessel bifurcation. B) Two-photon time-lapse imaging of a control mouse demonstrating little change in the boundary of GFP+ cells over time.

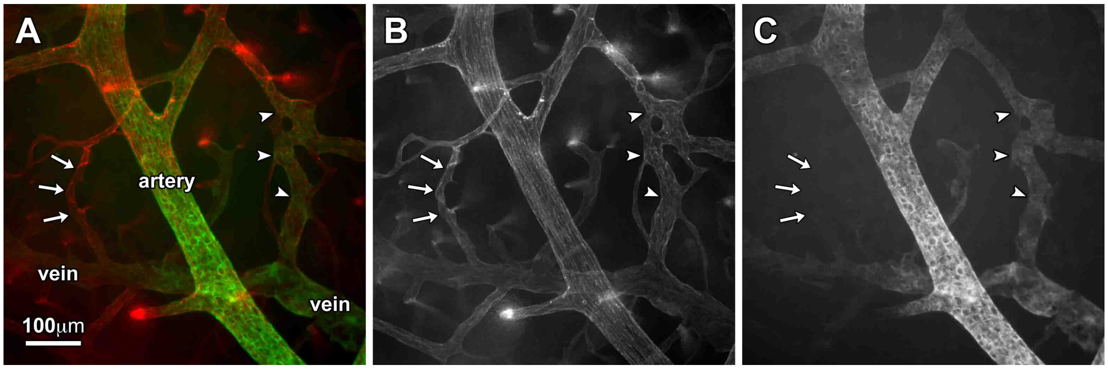

Figure 8. The onset of AV shunts can occur without smooth muscle coverage. Wholemount immunofluorescence imaging of cortical vasculature of Notch4* mutant mouse showing small and large AVMs. A) Merged image showing perfusion by Cy5-conjugated Lycopersicon esculentum lectin and staining with FITC-conjugated anti-alpha smooth muscle actin antibody. B) Image of Cy5 channel from panel (A) demonstrating a small and large AVM by perfusion labeling. C) Image of FITC channel from panel (A) demonstrating α smooth muscle staining throughout the large AVM (white arrowheads) but mostly negative in the small AV shunt (white arrows).

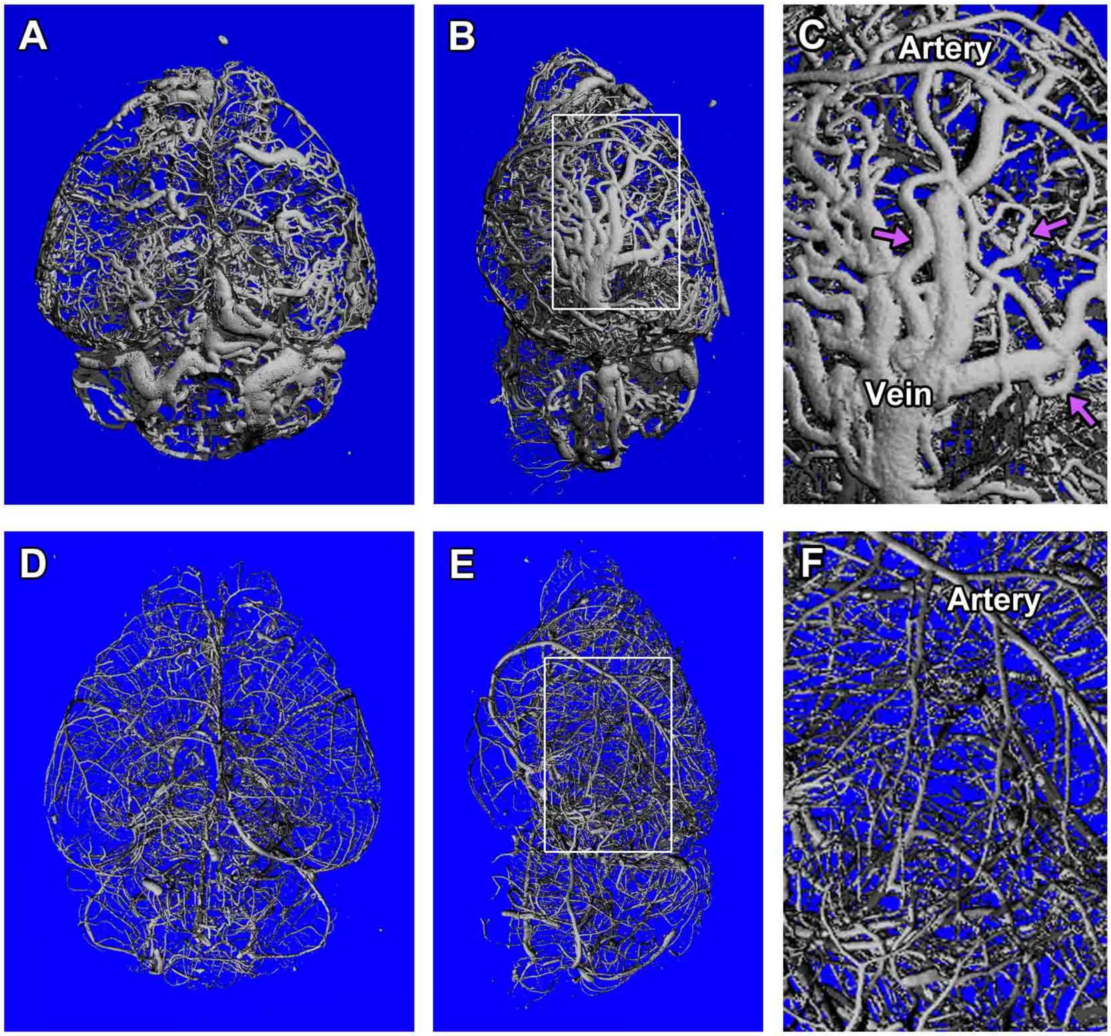

Supplemental Figure 1. Advanced-stage AVMs directly join major arteries and veins in Notch4* mice. MicroCT imaging of mutant and control mouse brains where contrast was provided by intra-cardiac perfusion of microfil. A-C) Imaging of a Notch4* mouse brain with advanced stage AVMs at P23. A) Superior and B) sagittal perspectives showing large and tortuous vessels throughout the brain. C) High magnification of boxed-region in panel (B) demonstrating extremely large caliber AV shunts directly joining the middle cerebral artery and a major draining vein (purple arrows). D-F) Imaging of littermate control brain at P23. D) Superior and E) sagittal perspectives showing no abnormally large vessels. F) High magnification of boxed-region in panel (E) demonstrating no AV shunts. The viscous microfil labeled arteries but not all veins, likely due to difficulty in passing through the capillary bed.

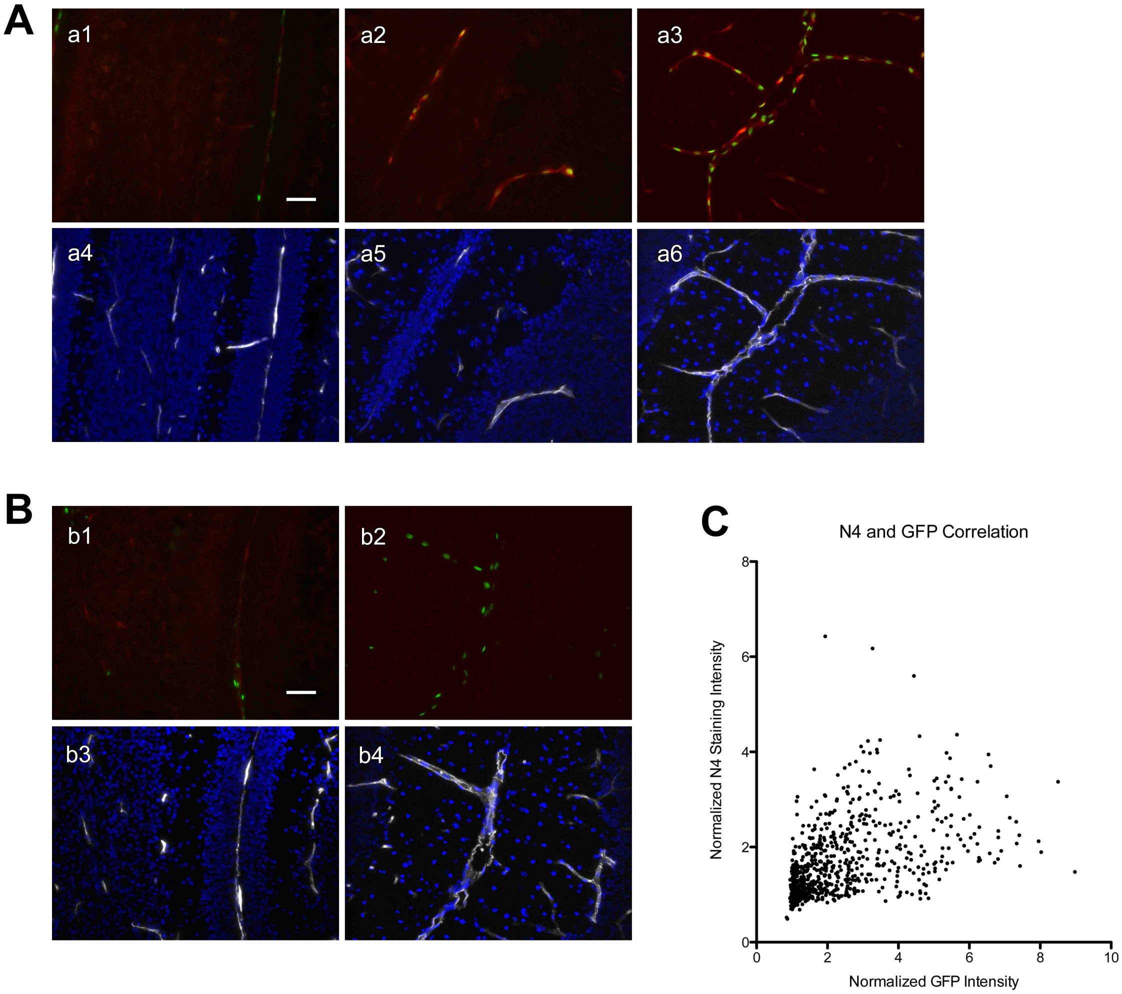

Supplemental Figure 2. Correlation of Notch4-ICD staining and TRE-GFP intensity. a1-a5) Notch4-ICD staining in sagittal brain sections of *Tie2-tTA/TRE-Notch4*/TRE-H2B-GFP* and control mice. b1-b5) Co-labeling by DAPI and perfusion of Cy5-conjugated Lycopersicon esculentum lectin. Endothelial nuclei were identified as DAPI+ nuclei enclosed by Cy5 labeling. ImageJ software was used to circumscribe these nuclei and quantify the enclosed intensities from the Notch4 and GFP channels. Notch4* staining in mutants was normalized to age-matched controls that were stained and imaged in the same experimental session. TRE-H2B-GFP expression in EC nuclei was normalized to background levels in neighboring, non-endothelial nuclei. C) Correlation between the normalized Notch4-ICD staining intensities and GFP expression in individual EC nuclei (Pearson r = 0.5286, P value < 0.0001).

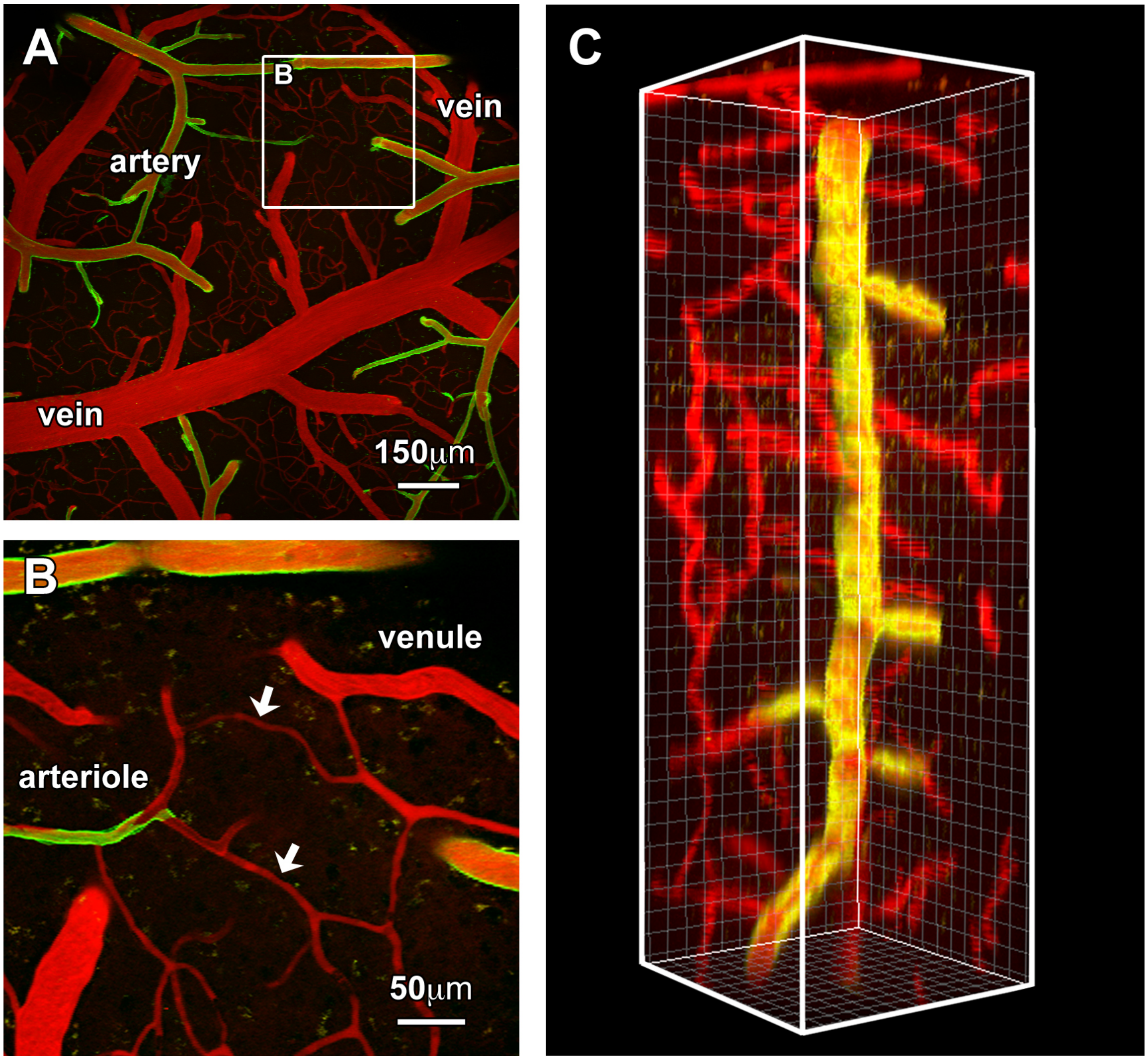

Supplemental Figure 3. *In vivo* labeling and Cre-mediated recombination in arterial endothelial cells. *In vivo* imaging of *BMX-CreER; mT/mG* construct where the plasma is labeled by intravenous injection of TexasRed-dextran. Mice are administered Tamoxifen at P1 and P2 to induce Cre-mediated recombination under regulation of the BMX promoter, resulting in irreversible GFP expression in arterial ECs from early post-natal life. Importantly, these cells remain GFP+ despite any subsequent changes in their arteriovenous specification. A) Low magnification view of the cortical vasculature demonstrating that arterial but not venous vessels are labeled with GFP. B) High magnification of the boxed-region from panel (A) demonstrating GFP expression in the arterioles but not capillaries or venules. The arteriole-capillary interface is visually distinguished by the boundary of GFP positive and negative expression along the vessels. C) Three-dimensional cortical stack demonstrating a penetrating arteriole that is also labeled by the *BMX-CreER; mT/mG* construct.

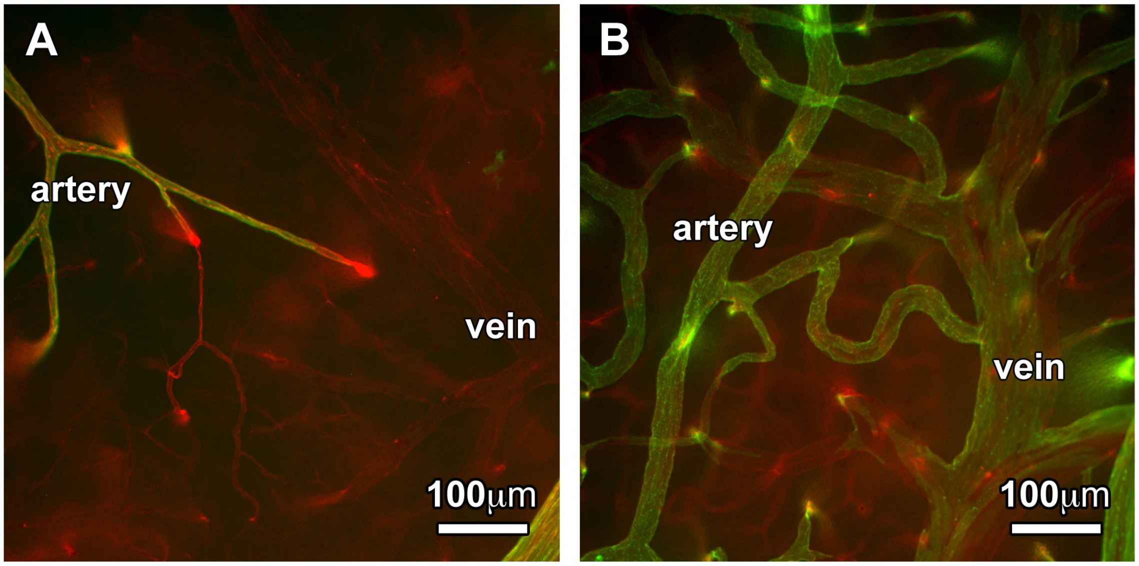

Supplemental Figure 4. BMX promoter activity is upregulated in Notch4*-mediated AVMs. Imaging of cortical vasculature of Notch4* mutant and control mice containing the *BMX-CreER; mT/mG* construct and perfused with Cy5-conjugated Lycopersicon esculentum lectin. Animals were administered Tamoxifen on post-natal days P16 and P17 and perfused at day P20. A) Littermate control demonstrating strong GFP labeling of arterial vessels but not capillaries or veins. B) Littermate mutant demonstrating robust expression of GFP in arteries, along the AV shunt, and patchy expression within the vein. Importantly, the timing of Cre-mediated recombination was chosen to correspond with a period after the onset of Notch4* expression.

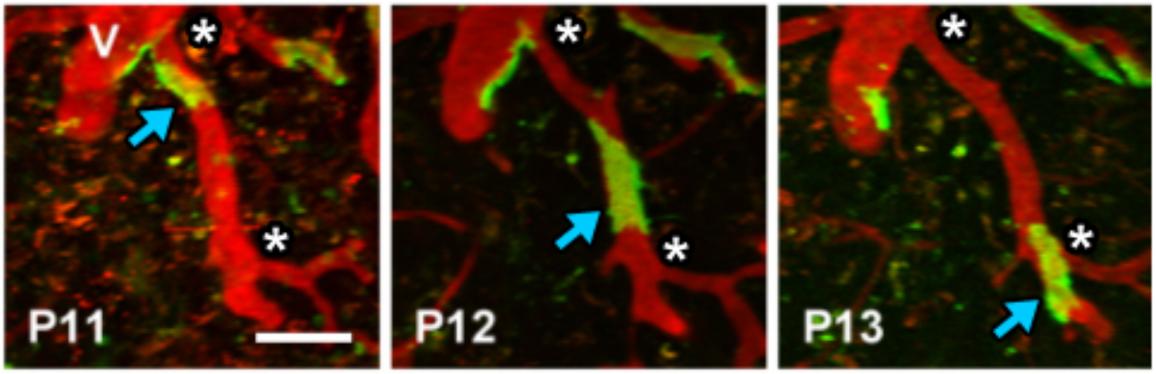

Supplemental Figure 5. Labeling and tracking of EC behavior in mouse brain*.* *In vivo* imaging of *Cdh-CreER; mT/mG* construct where the plasma is labeled by intravenous injection of TexasRed-dextran. Mice are administered low-dose Tamoxifen at P1 to induce Cre-mediated recombination in a few discrete endothelial cells, resulting in their expression of GFP from early post-natal life. Importantly, these cells continue to express GFP+ and their migration and proliferation can be tracked over time. Images correspond to post-natal day P11 through P13. (V) indicates a vein and the (*) denote the proximal and distal ends of a venule segment. The blue arrow shows an endothelial cell migrating within the venule. Note that this cell begins at one end and moves into the bifurcation point at the opposite end of the vessel segment. Scale bar is 20 microns.

DISCUSSIONS

The work in this dissertation creates a foundation for the dynamic study of vascular development in the neonatal brain and provides important insight into the pathology of brain arteriovenous malformation. Hemodynamic forces were once thought to be the primary determinants of artery and vein identity. More recently, studies have identified biochemical programs involved in specifying arteries and veins prior to circulation. The relationship between blood flow, AV specification, and vessel hierarchy may be better understood by investigating how these interdependent systems may be disrupted and restored.

Recently, we have reported that expression of activated Notch4 in endothelial cells results in AVMs in young and adult mice[1,2]. Additionally, we and others have linked increased Notch signaling in ECs with human brain AVMs[3,4], suggesting an important role for this signaling pathway in the pathogenesis of the disease. Notch's role in regulating markers of AV identity in ECs is compelling evidence for the physical segregation of arteries and veins. The sorting of endothelial cells between the early artery and vein in zebrafish and mouse embryo is an active field of study[5,6]. Importantly, Notch signaling has recently been established in regulating angiogenic sprouting by imparting a quiescent, non-sprouting phenotype on some ECs that may help to maintain the integrity of angiogenic blood vessels. However, these studies were conducted in specialized model systems where it was simpler to examine the extension of non-lumanized ECs into avascular regions. It currently remains unclear how perfused capillaries are maintained within the established AV network. Using our Notch-mediated mouse model of AVMs, we investigated how the appropriate balance of Notch signaling in vessels regulates the critical interface between arteries and veins through small, low-flow capillaries.

Using *in vivo* TPLSM through a cranial window, we observed that AV shunts enlarged from capillary-like vessels. The initial enlargement of these low-flow vessels often preceded their increase in blood velocity, indicating that expansion of the vessel lumen was the primary developmental defect. AV specification of the vasculature in mutant mice appeared normal at P10 prior to detection of Notch4* expression, suggesting that AV shunts arose from normal capillaries within the AV hierarchy. Conditional expression of Notch4* in arterial ECs did not lead to AVM formation. Similarly, blocking canonical Notch signaling in all ECs, but not arterial ECs, prevented the AVMs. Importantly, repression of Notch4* resulted in conversion of large-caliber AV shunts into capillary-like vessels and a normalization of blood flow. Taken together, these results indicate that ectopic Notch signaling outside of the arterial compartment was the specific genetic lesion leading to the enlargement of capillaries. Our work also compellingly suggests that the appropriate balance of Notch signaling actively maintains perfused capillaries between arteries and veins in postnatal life.

One of the most difficult aspects of studying biology is the intrinsic level of variability in living systems. Recent advancements in genetic and optical imaging technologies allow for interrogation of *in vivo* biology with incredible detail and specificity, helping to reduce the number of variables and determine mechanisms of interest. The work presented here utilizes TPLSM and regulatable genetic tools to study cerebral vascular development and concurrent blood flow dynamics at the cellular level. Importantly, this blend of genetics and optics is unbound from static, post-mortem analysis and allows for detailed study of dynamic processes over time. The possibilities are vast and herald a technical renaissance for developmental biology that will enable more rapid advancements in our understanding of normal and disease mechanisms. Additionally, our work provides an important analytical advancement in measuring blood flow dynamics with TPLSM, which will be helpful for the study of high-flow vascular biology in general.

REFERENCES

1 Carlson, T. R. *et al.* Endothelial expression of constitutively active Notch4 elicits reversible arteriovenous malformations in adult mice. *Proc Natl Acad Sci U S A* **102**, 9884-9889 (2005).

2 Murphy, P. A. *et al.* Endothelial Notch4 signaling induces hallmarks of brain arteriovenous malformations in mice. *Proceedings of the National Academy of Sciences of the United States of America* **105**, 10901-10906, doi:10.1073/pnas.0802743105 (2008).

3 ZhuGe, Q. *et al.* Notch-1 signalling is activated in brain arteriovenous malformations in humans. *Brain* **132**, 3231-3241, doi:10.1093/brain/awp246 (2009).

4 Murphy, P. A., Lu, G., Shiah, S., Bollen, A. W. & Wang, R. A. Endothelial Notch signaling is upregulated in human brain arteriovenous malformations and a mouse model of the disease. *Lab Invest* **89**, 971-982, doi:10.1038/labinvest.2009.62 (2009).

5 Herbert, S. P. *et al.* Arterial-venous segregation by selective cell sprouting: an alternative mode of blood vessel formation. *Science* **326**, 294-298, doi:10.1126/science.1178577 (2009).

6 Kim, Y. H. *et al.* Artery and vein size is balanced by Notch and ephrin B2/EphB4 during angiogenesis. *Development* **135**, 3755-3764, doi:10.1242/dev.022475 (2008).

Publishing Agreement

It is the policy of the University to encourage the distribution of all theses, dissertations, and manuscripts. Copies of all UCSF theses, dissertations, and manuscripts will be routed to the library via the Graduate Division. The library will make all theses, dissertations, and manuscripts accessible to the public and will preserve these to the best of their abilities, in perpetuity.

Please sign the following statement:

I hereby grant permission to the Graduate Division of the University of California, San Francisco to release copies of my thesis, dissertation, or manuscript to the Campus Library to provide access and preservation, in whole or in part, in perpetuity.

Author Signature

3/18/12

Date